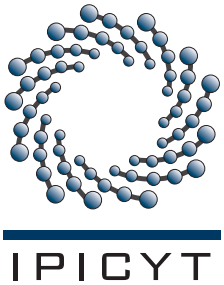

INSTITUTO POTOSINO DE INVESTIGACIÓN CIENTÍFICA Y TECNOLÓGICA, A.C.

POSGRADO EN CIENCIAS APLICADAS

Experimentos con microscopía óptica de partículas Brownianas atadas a biopolímeros asociados a la diatomea *Nitzschia* sp. y análisis de escala de las trayectorias de las diatomeas

Tesis que presenta

Andrés Jiménez Guerra

Para obtener el grado de

Maestro en Nanociencias y Materiales

Codirectores de la Tesis:

Dr. Braulio Gutiérrez Medina

Dr. Haret Codratian Rosu

San Luis Potosí, S.L.P., octubre de 2013

IPICYT

Constancia de aprobación de la tesis

La tesis "Experimentos con microscopía óptica de partículas Brownianas atadas a biopolímeros asociados a la diatomea Nitzschia sp. y análisis de escala de las trayectorias de las diatomeas" presentada para obtener el Grado de Maestro en Nanociencias y Materiales fue elaborada por **Andrés Jiménez Guerra** y aprobada el **veintidós de octubre de dos mil trece** por los suscritos, designados por el Colegio de Profesores de la División de Materiales Avanzados del Instituto Potosino de Investigación Científica y Tecnológica, A.C.

Dr. Braulio Gutiérrez Medina
Codirector de la tesis

Dr. Haret-Codratian Rosu Barbus
Codirector de la tesis

Dr. Gerardo Rafael Argüello Astorga
Miembro del Comité Tutoral

Dr. José Salomé Murguía Ibarra
Miembro del Comité Tutoral

Dra. Jessica Viridiana García Meza
Miembro del Comité Tutoral

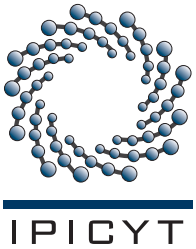

Créditos Institucionales

Esta tesis fue elaborada en el Laboratorio de Nanoestructuras I de la División de de Materiales Avanzados del Instituto Potosino de Investigación Científica y Tecnológica, A.C., y en el Laboratorio de Geomicrobiología del Instituto de Metalurgia de la Universidad Autónoma de San Luis Potosí bajo la dirección del Dr. Braulio Gutiérrez Medina, y la Dra. J. Viridiana García Meza, respectivamente.

Durante la realización del trabajo el autor recibió una beca académica del Consejo Nacional de Ciencia y Tecnología (No. de registro 201864) y del Instituto Potosino de Investigación Científica y Tecnológica, A. C.

IPICYT

Instituto Potosino de Investigación Científica y Tecnológica, A.C.

Acta de Examen de Grado

El Secretario Académico del Instituto Potosino de Investigación Científica y Tecnológica, A.C., certifica que en el Acta 006 del Libro Primero de Actas de Exámenes de Grado del Programa de Maestría en Nanociencias y Materiales está asentado lo siguiente:

En la ciudad de San Luis Potosí a los 22 días del mes de octubre del año 2013, se reunió a las 13:20 horas en las instalaciones del Instituto Potosino de Investigación Científica y Tecnológica, A.C., el Jurado integrado por:

Dr. José Salomé Murguía Ibarra	**Presidente**	**UASLP**
Dr. Gerardo Rafael Argüello Astorga	**Secretario**	**IPICYT**
Dr. Braulio Gutiérrez Medina	**Sinodal**	**IPICYT**
Dr. Haret-Codratian Rosu Barbus	**Sinodal**	**IPICYT**
Dra. Jessica Viridiana García Meza	**Sinodal externo**	**UASLP**

a fin de efectuar el examen, que para obtener el Grado de:

MAESTRO EN NANOCIENCIAS Y MATERIALES

sustentó el C.

Andrés Jiménez Guerra

sobre la Tesis intitulada:

Experimentos con microscopía óptica de partículas Brownianas atadas a biopolímeros asociados a la diatomea Nitzschia sp. y análisis de escala de las trayectorias de las diatomeas

que se desarrolló bajo la dirección de

Dr. Braulio Gutiérrez Medina
Dr. Haret-Codratian Rosu Barbus

El Jurado, después de deliberar, determinó

APROBARLO

Dándose por terminado el acto a las 14:35 horas, procediendo a la firma del Acta los integrantes del Jurado. Dando fe el Secretario Académico del Instituto.

A petición del interesado y para los fines que al mismo convengan, se extiende el presente documento en la ciudad de San Luis Potosí, S.L.P., México, a los 22 días del mes de octubre de 2013.

Dr. Marcial Bonilla Marín
Secretario Académico

Mtra. Ivonne Lizette Cuevas Vélez
Jefa del Departamento del Posgrado

INSTITUTO POTOSINO DE INVESTIGACIÓN CIENTÍFICA Y TECNOLÓGICA, A.C.
IPICYT
SECRETARIA ACADEMICA

RESUMEN

En este trabajo reportamos los resultados de dos tipos de experimentos realizados con la diatomea rafidea *Nitzschia* sp. a nivel de células individuales por medio de microscopía óptica. En el primer experimento se capturó en video el movimiento Browniano con atadura de microesferas de poliestireno (1.26 μm) donde la atadura consistió de nanofibras adhesivas asociadas a las biopelículas formadas en superficies por diatomeas de esta especie. En el segundo experimento, también por video microscopía, capturamos las trayectorias de diatomeas vivas *Nitzschia* sp. Para ambos experimentos se obtuvieron las series de tiempo correspondientes al movimiento Browniano con atadura y a la motilidad celular, respectivamente, y estas series fueron analizadas por el método estadístico de escala Anális de Fluctuaciones sin Tendencia (DFA, en inglés) optimizado por una transformada ondeleta. De esta manera se determinó el exponente de Hurst que caracteriza la naturaleza del movimiento Browniano de atadura y del movimiento de diatomeas vivas. Del punto de vista de fluctuaciones $1/f$, encontramos que el movimiento de atadura de las microesferas es persistente, sugiriendo un movimiento Browniano de carácter fractal. Por otro lado, el movimiento celular de las diatomeas *Nitzschia* sp., también persistente, sugiere una motilidad celular activa con un tipo de memoria.

Descriptores: análisis de fluctuaciones sin tendencia; diatomeas; microscopía óptica convencional; monofractal; movimiento de partícula con atadura; trayectorias celulares; ondeletas.

ABSTRACT

In this thesis, we report the results of two types of experiments we performed with the raphid type *Nitzschia* sp. diatom of the single cell level using optical microscopy. In the first experiment, the tethered Brownian motion of polystyrene microspheres (1.26 μm) was captured in video in which the tether consisted of adhesive nanofibers associated to the biofilms formed on surfaces by diatoms of this species. In the second experiment, also done with video microscopy, we captured the trajectories of live *Nitzschia* sp. diatoms. For both experiments, the time series corresponding to the tethered Brownian motion and the cell motility, respectively, were obtained and analyzed with the scaling statistical method Detrended Fluctuation Analysis (DFA) optimized via a wavelet transfrom. In this way, we determined the Hurst parameter that characterizes the nature of the tethered Brownian motion and that of live diatoms. From the standpoint of $1/f$ fluctuations, we have found that the tethered motion of microspheres is persistent, suggesting a Brownian motion with a fractal feature. On the other hand, the cell motion of *Nitzschia* sp. diatoms, also persistent, suggests an active cell motility with a kind of memory.

Keywords: conventional optical microscopy; diatoms; detrended fluctuation analysis; cell trajectories; monofractal; tethered particle motion; wavelets.

All mov'd together, and kept the same position
in respect to one another, however, agitated by the Water;
these considerations, I say, persuade me,
that they may be rather Plants than Salts.

— Mr. C, 1702.
First reported microscope
observation of diatoms [100].

ACKNOWLEDGEMENTS

I thank my advisors, *Braulio Gutiérrez* and *Haret Rosu*, for giving me the chance to work together in this project, and all in all for the sense of orderliness and craftsmanship that I learned from them. Special thanks to *Salomé Murguía* for the genuine interest in the project and the great help in the final stage of elaborating this thesis. *Gerardo Argüello* for his feedback on my previous research topic.

I also thank *Viridiana García* for her friendship, gently allowing me the use of her laboratory equipment and introducing me to her lab members; *Yadiralia Covarrubias*, and *Nubia Arteaga*, who shared their ideas about this project; but mostly *Sayuri Sánchez*, who taught me everyday, and *Georgina González*, for carrying on with my training in the lab.

My thanks to *José Antonio Robledo* for solving the `crossings` algorithm presented in this work. *Noemí Hernández* for instructing me, and along with *Alma Oaxaca*, in helping me polish my oral presentations.

Horacio Flores, *Miguel Ávalos*, and *Vicente Rodríguez* for their sincere attention to my academic progress. *José Luis S. Llamazares* and *Pablo Ibarra* for valuable advise with the manuscript, as well as *Cal Newport* for his continuous academic guidance.

Ivonne Cuevas, *Edith Rodríguez*, *Minerva Jiménez*, and *Rafael Rico* for their kind help in administrative efforts.

The group members of both IPICYT Pinzas Ópticas and IM-UASLP Geomicrobiología labs for assisting me.

André Miede and the TEX-community for support, and valuable software.

I thank those who lend a hand to me in different stages during my academic formation: *Bruce Lundberg*, *Marta and Steve Wallin*, *Dave Spenny*, *James Derr*, *Janet Barnett*, *Bill Brown*, *Pedro Villaseñor*, *Ricardo Guirado*, *Máximo Lopez*, *Ciro Falcony*, *Agustín Conde*, *Kurihara Susumu*, and *Matsuda Iwao*.

I'm grateful to Consejo Nacional de Ciencia y Tecnología (CONACyT), México, for the financial support through a scholarship.

CONTENTS

LIST OF FIGURES

LIST OF TABLES

LISTINGS

ACRONYMS

AC Adhesion complex.

ANF Adhesive nanofiber.

AFM Atomic force microscopy.

DFA Detrended fluctuation analysis.

DIC Differential interference contrast microscopy.

EPS Extracellular polymeric substance.

FWT Fast wavelet transform.

fBm Fractional Brownian motion.

fGn Fractional Gaussian noise.

GUI Graphical user interface.

LRC Long-range correlation.

MF-DFA Multi fractal detrended fluctuation analysis.

ROI Region of interest.

R/S Rescaled range analysis.

RMS Root mean squared.

SEM Scanning electron microscopy.

TBM Tethered Brownian motion.

TPM Tethered particle motion.

WT-DFA Wavelet transform detrended fluctuation analysis.

WHM Woods Hole culture medium.

1 INTRODUCTION

Diatoms are microscopic unicellular algae ubiquitous to marine and freshwater habitats capable of performing photosynthesis. Despite their microscopic size, diatoms contribute to 20% of the global carbon fixation [6, 21], and are the leading group in the biogenic silica production [47]. They exhibit *cell adhesion* and an adaptive migration known as *diatom cell motility* [115, 133]. Both of these processes are interrelated and of interest in bionanotechnology and for industrial applications [3, 7, 50, 62, 86, 87, 95, 130].

Moreover, *biofouling*, which is the colonization via adhesion of organisms such as diatoms in natural and artificial substrates, especially from the standpoint of preventing it, has been a strong motivation of studying bioadhesives and related surface technologies [11, 21, 66, 74, 76, 77, 88, 94]. On the other hand, the nature of the motility of diatoms has been thoroughly investigated [20, 44, 45, 46, 74, 76, 101, 115, 129, 135] and even some biodevices using live diatoms have been proposed [87, 130].

Previously, diatoms have been studied in different disciplines such as genetics [6, 15], molecular biology [21, 45], chemistry [22, 47], materials science [5, 7], and also for biomimetics [81] and technological applications [87] (for reviews see Kröger & Poulsen 2008 [86]). Currently, there is a standard model for the motility of diatoms, detailed in Chapter 2, but the precise biochemistry and physical properties of the adhesive strands that mediate adhesion and motility is still a work in progress.

GOALS: In this work, we made subcultures of the raphid type *Nitzschia* sp. diatom, and we focus on two general problems. Executing a single molecule study of diatom bioadhesives that are complementary to AFM techniques previously reported [22, 27, 39, 40, 58, 73, 74, 75] and an automated analysis of diatom cell motility. Within these two general problems we paid special attention to the following issues:

- Characterizing the tethered Brownian motion of microspheres that were attached to adhesive nanofibers during Tethered Particle Motion (TPM) measurements captured with video microscopy.
- Studying the diatom trajectories using novel parameters that can be helpful for future studies of diatom motility in response to photostimulation.

- Performing the mathematical analysis of the trajectories of live diatoms incubated in a flow cell.

OUR CONTRIBUTION: A detailed statistical analysis of single diatom trajectories using in-house automated software is presented. Besides, the kinematic features of *Nitzschia* sp. diatom motion to nanometric scale are determined and a physical model for the motility characteristics of this diatom species is also discussed. To our knowledge, such inclusive approach has not been done before using live diatoms.

This is the first time TPM techniques have been applied to polymeric biofilms produced *in situ* by live diatoms and an application of the analyses of time series originated from TPM measurements by scaling methods.

RESULTS: Two types of results are reported; the first type refers to the time series of the TBM experiments which has been analyzed by statistical methods of the scaling type, mainly the Detrended Fluctuation Analysis. The type of fractional Brownian motion corresponding to this experiment has been stablished by determining the Hurst parameters of this kind of tethered motion.

The second class of results refers to the *Nitzschia* sp. diatoms. In this case, we have been provided with axenic subcultures of *Nitzschia* sp. diatoms made in the IM-UASLP Geomicrobiología laboratory. The motion of live diatoms has been recorded by us and the Hurst scaling parameters of their motion in a lab-designed experiment at IPICYT have been determined through the same Detrended Fluctuation Analysis as in the case of TBM.

From the Brownian motion standpoint, the recorded motion of *Nitzschia* sp. diatoms is characteristic of persistent time series which indicates a memory effect specific to particles capable of active motion in a given environment.

Part I

THEORETICAL BACKGROUND

This part includes three introductory chapters. A first chapter about diatoms, their cell adhesion and cell motility, and the current state of diatom research. A second chapter describing the tethered Brownian motion of particles in solution. Finally, a third chapter covering the scaling analyses used in this work.

2 DIATOMS: BIOADHESION AND CELL MOTILITY

This chapter covers the general biology and cell motility of diatoms, as well as the properties of the biofilms they produce. The bibliography is curated from topics related to our three goals: (a) probe the diatom adhesive biofilms using a single molecule approach, (b) study diatom trajectories, and (c) investigate the diatom motion using fractal scaling analyses.

The final section of this chapter discusses the current state of diatom research, its trends, and the areas with potential development.

2.1 CELL BIOLOGY

Diatoms are microscopic photosynthetic algae, with the protoplast enclosed in a cell wall made of silica that is highly ornated with patterns unique to each species. They are ubiquitous in marine and freshwater habitats and exhibit both planktic and benthic lifestyles [98] (see Figure 1 and Figure 2).

They are eukaryotic organisms, unicellular protists, of class Bacillariophyceae and group division Ochrophyta [27, 73, 74]. Despite their microscopic size, diatoms contribute to 20% of the global carbon fixation [6, 21], and are the leading group in the biogenic silica production [47].

There is active research in determining the biochemistry and the physical properties of the biofilms associated with diatoms to prevent biofouling [3, 77, 95]. As major biofoulers, diatoms are of the first organisms to colonize clear natural and artificial surfaces by adhering to substrata and developing what is known as the primary biofilm or slime [37, 77, 94, 131, 133]. Antifouling coatings have been successful at preventing permanent adherence of diatom slimes from certain species [3, 7] but are not environmental friendly and have been regulated. Currently, there is no coating that eases the removal of build up from diatom slimes [22].

Cell morphology

A diatom's cell wall consists of two silica structures, known as the epitheca and hypotheca (plus a range of organic coatings), each having a valve that allows nutrients and gas exchange with the surroundings [40, 90]. Girdle bands along the cell wall stretch and contract to ease cell division and growth [98]. The microstructure of girdle bands

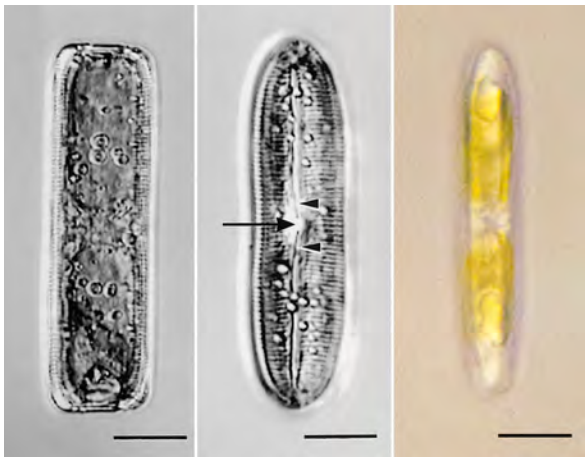

Figure 1: Light micrographs of live diatom cells. Images of *Pinnularia viridis* shown in, (left) girdle view and in (middle) valve view [27]. (right) *Nitzschia* sp. shown in valve view taken by the author at IPICYT (2013). Scale bars, (left, middle) 20 µm and, (right) 6 µm.

and valves is porous and highly organized. It may include slits from where diatoms secrete extracellular polymeric substances (EPS) that have a function of fixing adhesion, forming colonies, and sustaining cell motility. Motility is a behavior of photosynthetic organisms in depositional environments of low illumination, and their adaptive response is to migrate into illuminated zones near the surface [20, 131].

Most pennate diatoms have bilateral symmetry including an elongated slit along each of the two valves, known as the *raphe*, from which an adhesive substance is secreted (Figure 3). The raphe bridges intracellular structures to external surfaces via adhesive secretions resulting in cell-substratum adhesion and cell motility. This kind of motility is non-flagellar and because the cell wall does not suffer deformations as in crawling motility, the substrate dependent motility of diatoms is known as *gliding* [36, 133].

While diatoms glide, they leave behind trails of adhesive strands that can buildup and develop a biofilm matrix (see Figure 4a) [44, 46, 73, 133].

Motility observations help to understand the ecological and physiological relevance of diatom migrations. For example, in tidal flat sediments diatoms exhibit a rhythmic migratory behavior that actively controls their solar irradiance exposure. The primary response to prevent photoinhibition is the vertical migration of the diatoms in the sediment-biofilm matrix and is complementary of the xanthophyll cycle, a physiological process responsible of dissipating and reducing the energy that reaches the photosynthetic reaction centers, thus protecting the cell [20, 109, 110].

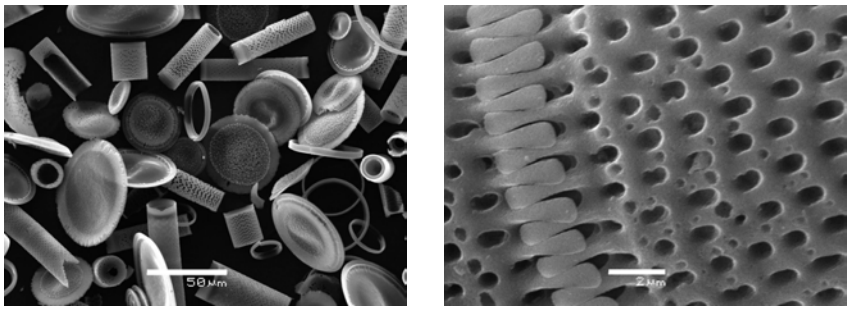

(a) (b)

Figure 2: SEM images of preserved diatom cells collected from 800 m underwater sediments and dated 8 – 10 thousand years old [47]. (a) Noncrystalline SiO_2 cell walls of various species. (b) Magnification of the porous microstructure and girdle band that is coated by organic macromolecules (proteins, polysaccharides, LCPA) and allows exchange of nutrients and gas with the external surroundings [86]. Scale bars, (a) 50 µm and, (b) 2 µm.

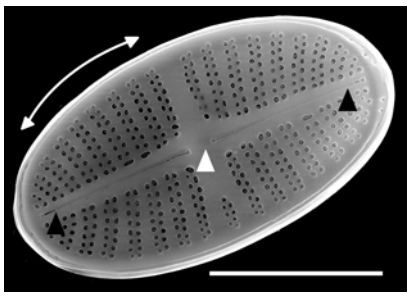

Figure 3: SEM image of a monoraphid *Platessa stewartii* diatom cell of elliptical valves shown in valve view. (Based on Potapova 2010 [113]). Girdle band (arrows) wraps around the cell, and the raphe (dark arrowheads) is discontinuous at the central zone of the valve (bright arrowhead). Scale bar, 5 µm.

2.2 MOTILITY IN RAPHID DIATOMS

Edgar & Pickett-Heaps proposed in 1984 the first basic model of cell motility in raphid diatoms [45, 46]. In their model the extracellular adhesive strands are connected to an internal bundle of actin filaments through the plasma membrane which sets in diatom locomotion. Wetherbee et al. (1998) developed upon this model suggesting that the actin filament assembly was not capable of generating enough force for motility, but instead proposed that it provided a scaffold for an actin-myosin molecular motor [133]. This argument is reasonable because other protoists, for example the *Toxoplasma gondii* and *Plasmodium falciparum* parasites, have been found at that time to glide using a similar actin-myosin system [36, 112].

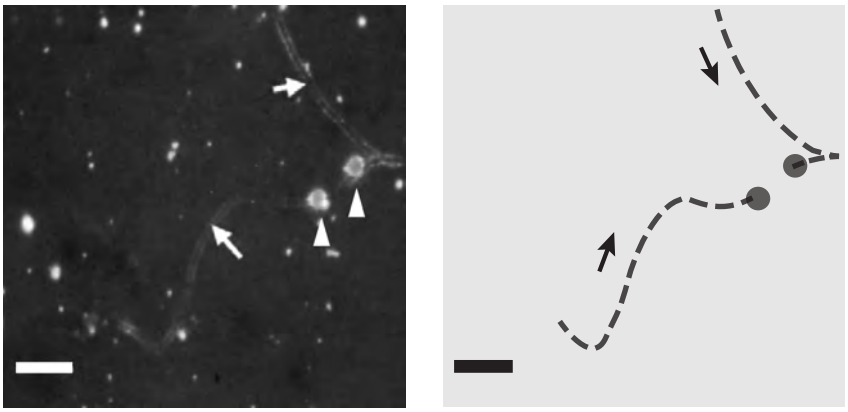

(a) (b)

Figure 4: (a) Fluorescence image of 'train-track' like adhesive trails (arrows) left by *Amphora coffeaeformis* diatoms (arrowheads). (Based on Wigglesworth-Cooksey & Cooksey 2005 [135]). (b) Representation of the diatom trajectories in (a) where arrows indicate the direction of cell motility. Scale bars, 50 μm.

Adhesion Complex model (AC)

The paper of Wetherbee et al. (1998), introduced the Adhesion Complex model (see Figure 5) that explains the mechanism for both adhesion and motility and which became the standard model, especially after Poulsen et al. (1999) validated it in the following year [115].

AC incorporates a seamless polarized group of molecules and associated intracellular proteins. The proteins extend from actin filaments through connectors linking to extracellular adhesive strands that come outside the cell from the raphe and become attached to the substratum. The role of myosin is to move along the acting filaments generating the mechanical force that results in cell motility. The actin bundle and associated proteins act as a scaffold for the molecular motor myosin that is capable of translocating actin filaments by the hydrolysis of ATP [36, 115].

The mechanical force in the AC acts as a tractional force running parallel to the actin filaments, like a treadmill moving belt, resulting in the thrust of the diatom in the opposite direction of the tractional force [46, 115, 133]. As the diatom moves forward an adhesive substance is continuously being secreted from the raphe while a supply of adhesive is made ready for immediate use. As the new supply is available, a trail of adhesive strands deposit in the substratum cut smoothly at the membrane as these slide to the edge of the raphe.

In the paper of Poulsen et al. (1999) the role of actin and myosin in diatom adhesion and motility is investigated in detail [115]. In their two independent experiments, cell motility is hindered by treating diatoms with an actin inhibitor or a myosin inhibitor, respectively.

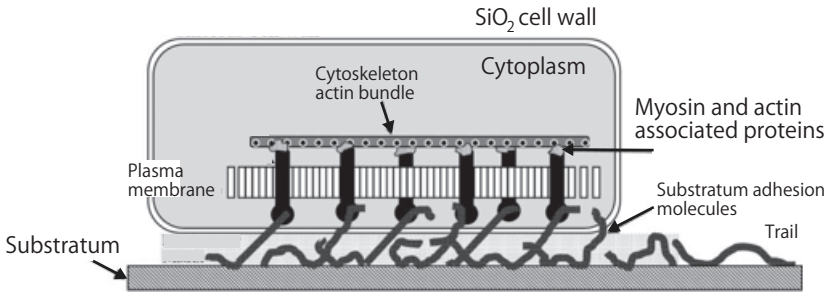

Figure 5: Adhesion complex motility model (AC). (Based on Poulsen et al. 1999 [115]). See text for complete description.

When the actin inhibitor was introduced it resulted in the absence of adhesive strands halting the cells. Inhibiting myosin affected the capability of myosin to generate a mechanical force to propel the diatom and cell locomotion was not observed.
A decade later, Molino et al. (2008) used a Quartz Crystal Microbalance with Dissipation monitoring (QCM-D) to test the myosin capabilities in the AC model [97]. This technique is surface sensitive via a piezoelectric quartz crystal that oscillates in response to an alternating applied voltage. Cell adhesion and migration on the QCM-D sensor surface slightly change the sensor's oscillating frequency translating into mass being deposited (removed) on (from) the surface. To examine directly the role of the actin-myosin system, diatoms were treated with the same myosin inhibitor as Poulsen et al. [115], and were injected onto hydrophobic and hydrophilic functionalized surfaces. Diatoms adhered strongly to the hydrophobic surface and became incapable of moving. However, the frequency and dissipation responses recorded were theorized a consequence of a pulling force via the AC actin-myosin system. When the cells were treated with the myosin inhibitor the pulling force was not reproduced, thus validating the essential function of myosin in the AC model [97, 115].

2.3 MECHANISMS OF CELL ADHESION

It is well established that diatoms go through two stages of primary and secondary adhesion [25, 74, 133].

PRIMARY DIATOM ADHESION: Diatoms typically sediment and land on their girdle bands, and initially, their raphes are not in contact with the surface. During primary adhesion, a diatom expends

energy as it relocates itself by guiding its raphe until it contacts and adheres to a surface [133] (see Figure 6a). But the cause of cells to reorientate is merely a stochastic process rather than the effect of a surface proximity transducer [25]. Higgins et al. observed diatoms that secreted adhesive networks from their raphes that had accumulated within reach of the closest surface as to pull themselves onto one raphe (see Figure 6b & Figure 7) [74]. When the raphe was in contact with the surface the diatoms could begin gliding. Its primary adhesion is reversible, and diatoms may detach from non optimal surfaces.

SECONDARY DIATOM ADHESION: Following primary adhesion, the secondary adhesion is a more permanent adhesion structure in a biofilm construction that does not require a continuos expenditure of energy. Fouling slimes fabricated by diatom EPS develop thick films of varying extension and architectural complexity that in a natural setting, for example a tidal fluctuation, help diatoms to settle and protects them from drying. The biofilm matrix is EPS, mainly pads and stalks as well as any adhesive trails left mostly by raphid motile diatoms [96]. Secondary diatom adhesion is also a reversible mechanism controlled by the AC.

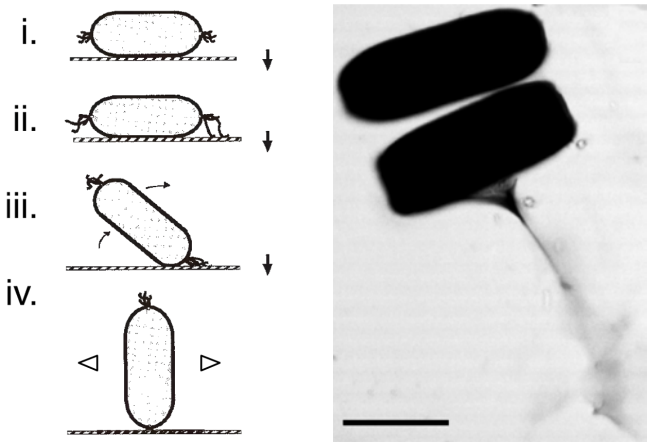

(a) (b)

Figure 6: (a) Stages of primary adhesion. (i–iii) Diatom reorientates guiding its raphe to contact the surface. (iv) The in-contact raphe allows the cell to have multiple directional motility. (Based on Wetherbee et al. 1998 [133]). (b) Superimposed light micrographs of stained tethers from a chemically fixed *Pinnularia viridis* cell that attached to the coverslip. (Based on Higgins et al. 2003 [74]). Scale bar, 20 µm.

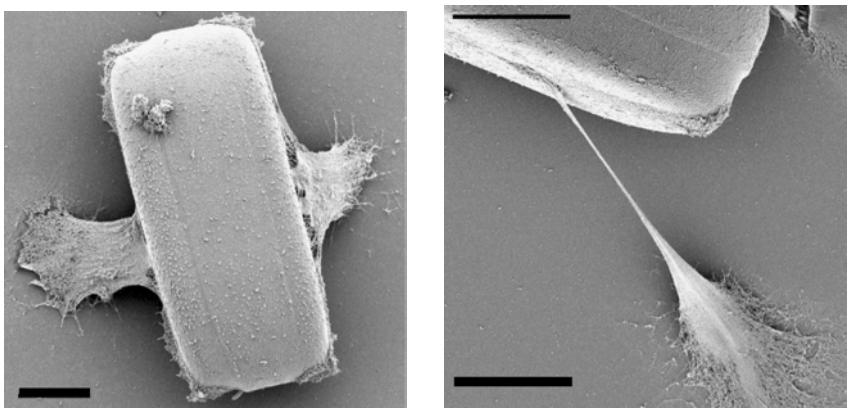

(a) (b)

Figure 7: SEM images of *Pinnularia viridis* cells during primary adhesion [74]. Scale bars, (a) 10 µm and, (b) 15 µm.

2.4 DIATOM ADHESIVES

Biochemistry

The extracellular adhesive is a composite of proteoglycans, proteins, and yet undefined carbohydrates [21]. Thirty years of research have identified a few components of the carbohydrate complex as the anionic polysaccharides and heterogeneous monosaccharides, sulfate ester, uronic acid, and O-methylated sugars [21, 125]. Biochemical analysis [23] and AFM investigations [39, 40, 41], have identified that the primary adhesive components in the extracellular secretions are certain type of protein groups (see below).

Physical Properties

Any submicrometre object bonds to a solid surface with an adhesive force ranging from 10 – 1000 nN [62]. At this scale, van der Waals interactions of approximately 100 nN are significant and compete with capillary forces, with van der Waals being dominant in hydrophobic surfaces. Within this force range, many researchers used AFM to probe the diatom EPS *in situ* in its native hydrated state and designed studies to characterize the mechanical and elastic properties of the EPS.

For a list of research highlights in this area, see Table 1.

In the following we comment on the main works that used AFM. Crawford et al. (2001) used contact mode AFM imaging and revealed that the organic layer encapsulating the cell wall, and associated with secretions from pores in the valves and girdle bands, is an amorphous

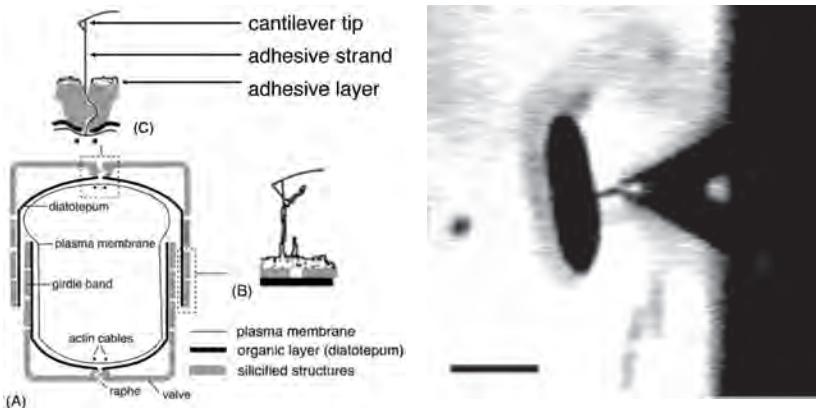

(a) (b)

Figure 8: (a) Experimental design for studying the adhesive found in the cell wall secreted from the girdle band (inset:B), or from the raphe (inset:C). An image of (b) an adhesive tether from a *Pinnularia viridis* diatom attached to a cantilever at an instant where the tether appears fully stretched. (Based on Higgins et al. 2002, 2003 [73, 74]). Scale bar, 100 µm.

and non-adhesive compressible material that does not obstruct the raphe fissure [27].

Furthermore, Higgins et al. (2002, 2003) characterized two distinct EPS found in diatom secretions. The material derived from the raphe (minimum adhesive force, 60 nN) exhibited a strong adhesive polymer behavior; the material derived from the girdle (adhesive force, 3.6 nN) behaved as a soft compressible polymer [73]. (See Figure 8). Subsequent studies probed the raphe-derived pads with a popular AFM technique called 'fly-fishing.' This technique scans the surface of the sample without burying the cantilever tip, and any protruding macromolecule with the size of a few nanometers interacts and strongly adsorbs to the tip [74]. Retracting the tip from the anchored adhesive strands resulted in a series of regularly spaced peaks in the extension-force curves in the form of sawtooth patterns [74, 75]. (See Figure 9).

This finding indicated that the diatom adhesive went through a sequenced unfolding of modular domains in resemblance with previous reports about other modular macromolecules [83, 119].

Elaborating on this work, Dugdale et al. (2005) reliably matched AFM sawtooth patterns from diatom adhesive EPS with those reported as fingerprints of modular proteins [39, 83, 119], and such curves could be superimposed for hundreds of stretch-relax cycles.

The repeatability of the cycles is evidence of a single adhesive being stretched rather than a variable unaligned number of molecules [39, 40]. The single cohesive unit is now known as an *adhesive nanofiber*.

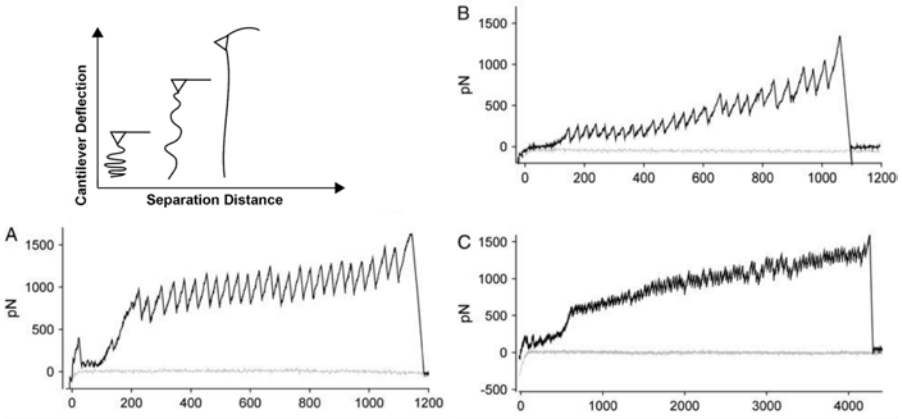

Figure 9: Types of adhesive nanofibers and their sawtooth force curves from 'fly-fishing' AFM studies: Type I (A), type II (B), and type III (C) (advancing = flat, retracting = sawtooth) Inset: AFM experimental design. (Based on Dugdale et al. 2006 [40]). See text for description.

The adhesive nanofibers have been identified and classified as type I, II, III, plus oligomers. Researchers have also proposed their architectural role in the development of the biofilm matrix, and shown that modular proteins are an essential component of the bioadhesives of both motile and non-motile diatoms [22, 40, 41].

Combining AFM with other techniques, Chiovitti et al. (2003, 2008) found that nanofibers in pads are made up of high-molecular-mass glycoproteins cross linked by mineral ions [21]. The ions are thought responsible for the modular proteins being capable to sustain numerous unfolding-refolding cycles while keeping their adhesive strength [22].

ADHESIVE NANOFIBERS: An adhesive nanofiber is a cohesive unit of modular proteins aligned in parallel [40], with adhesives forces of $\approx$ 0.200 nN that vary for different diatom species [39, 74].

The raphe-derived EPS is a stronger adhesive polymer than EPS secreted from pores (rupture forces of $\approx$ 60 nN and $\approx$ 13 nN, respectively) [73].

The length of an adhesive nanofiber could be up to 1.2 µm before rupture. [39]. It extends in at least two sections; the first is a 200 nm long section with a 'free' conformation that twists with out deflecting an AFM cantilever; the remainder is structured as a rigid backbone, composed of up to 27 folded domains where each domain unfolds in 34 nm bundles [39]. (See Figure 9).

The energy required to fully stretch an adhesive nanofiber (hundreds of 10^{-18} J, collagen is tens of 10^{-18} J) does not decrease with subsequent cycles, indicating the cohesion of a definite number of bridged modular proteins [39].

Adhesive nanofibers have been modeled as polymers [39]. The WLC model [18] describes the mechanical behavior of a polymer under a full range of stretching forces on torsionally unconstrained polymer chains. Under the WLC fit, an adhesive nanofiber persistence length is 0.036 nm with an unfolding force of 0.800 nN per domain, and rupture forces are of ≈ 0.790 nN [40].

Adhesive nanofibers are a biocomposite of groups of modular proteins classified by types I, II, and III, plus oligomers:

- Type I. Group of ≈ 29 modular protein molecules present in all adhesive pads. Adhesive nanofibers are mainly made of type I molecules. (Rupture force F_{max} = 0.872 nN. Persistence length, L_p = 0.030 nm).
- Type II. Group of ≈ 10 modular proteins spread along the entire length of the fiber. (F_{max} = 0.516 nN, L_p = 0.090 nm).
- Type III. Group of ≈ 20 modular protein molecules of > 5 μm long when unfolded. (F_{max} = 0.850 nN, L_p = 0.040 nm).
- Oligomers. A small bundle of ≈ 5 single molecules not found in all pads. (F_{max} = 0.270 nN, L_p = 0.190 nm).

These groups give structure to adhesive nanofibers, each of them distinguishable from one another and characterized by a distinct rupture force, persistence length, and interpeak force based on force curves.

2.5 BIOFILM DEVELOPMENT

In this document, we investigate experimentally the physical properties of the biofilms associated with the diatom species *Nitzschia*. This species is a common genus that exhibits cell adhesion and gliding motility, as well as secretion of an adhesive EPS that form biofilms on natural and artificial substrates to which they have attached [29].

The EPS composition is 95% polysaccharides and it is balanced by proteins (Sutherland 1999 cited in Stal & Brouwer 2003). Of the total, two distinct EPS fractions are found in diatoms; soluble EPS and bound EPS [29, 37, 125]. Soluble EPS is found dissolved in the culture medium, whereas bound EPS is localized on diatoms and diatom aggregates. This is in agreement with Higgins et al. who have visualized and confirmed the distinct adhesive EPS using AFM [73, 74]. (See Figure 10).

ADHESIVE NANOFIBERS RESEARCH HIGHLIGHTS
Crawford et al. (2001) (Diatom features: motile, freshwater) (Adhesive derived from: organic cell coating) The organic cell coating is soft and non adhesive, and does not obstruct the raphe [27].
Higgins et al. (2002) (Diatom: motile, marine) (Adhesive: girdle band pores and raphe) The raphe-derived adhesive is a strong adhesive polymer, while the pore-derived is soft and compressible [73].
Higgins et al. (2003) (Diatom: motile, freshwater and marine) (Adhesive: raphe) Observed sawtooth patterns in AFM measurements suggested an unfolding of modular domains [74].
Dugdale et al. (2005) (Diatom: non-motile, marine) (Adhesive: pad) Discovered the adhesive is made of cohesive units of modular proteins aligned in parallel, and the individual strands adopted the name of *adhesive nanofibers* [39].
Dugdale et al. (2006) (Diatom: motile, marine) (Adhesive: pad) Identified and classified the adhesive nanofibers as type I, II, III, plus oligomers, and proposed their architectural role in the development of the biofilm matrix [40].
Dugdale et al. (2006) (Diatom: motile, marine) (Adhesive: raphe) Shown that modular proteins are an essential component of the bioadhesives of both motile and non-motile diatoms [41].
Chiovitti et al. (2003, 2008) (Diatom: non-motile, marine) (Adhesive: pad) Identified specific protein groups cross-linked by cations as structural components of the nanofibers.The cross-linking of the backbones of adjacent modular domains explains the mechanism for the nanofibers to fold and re-fold in register [23, 21, 22].

Table 1: Adhesive nanofibers research highlights.

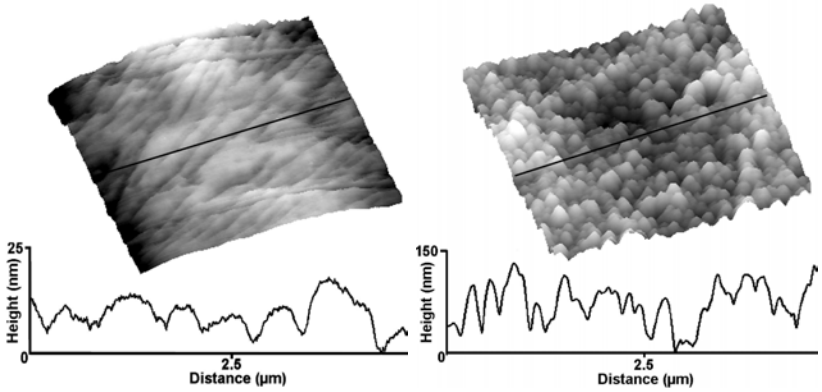

(a) (b)

Figure 10: AFM (tapping mode) height images of adhesive EPS layers on live diatoms. A region of long striated-like topography in *Craspedostauros australis* (a), and a granular texture in *Pinnularia viridis* (b) are shown. Height profiles taken across the black line for each corresponding image are shown below. (Based on Higgins et al. 2003 [75]).

SOLUBLE EPS: It is recovered from culture post-centrifugation supernatant and it represents polysaccharides that do not associate strongly with the cells. Its composition is mostly galactose and glucuronic acid. For *Nitzschia* sp. diatoms, it takes 18 – 22% of the internal carbohydrate supply and bound EPS to be produced. Its production continues during the stationary growth phase, which remains after a cultivation period of 2 weeks for this species, and in the dark at expense of internal sugars [29, 125]. Additionally, in this work, we have observed that in the presence of soluble EPS, the motility rates of *Nitzschia* sp. diatoms decrease by at least 30% (details on p. 94).

BOUND EPS: Bound EPS is localized in the organic layers encapsulating the diatom cell wall and is closely associated with diatom aggregates. It is 80% glucose and has minor quantities of uronic acids [21, 125]. This EPS is produced only in the light and in large concentrations during the 8-day exponential phase of *Nitzschia* sp.. Thus, in comparison to soluble EPS, bound EPS is light dependent [29].

The differences of the two EPS fractions in localization, composition, and production suggest they are under distinct metabolic controls and have different cellular functions. [29, 125].

2.6 CURRENT STATE OF DIATOM RESEARCH

In the last decade, diatom research has grown steadily. A major effort was the sequencing of the entire genomes of the diatoms *Thalassiosira pseudonana* [6] and *Phaeodactylum tricornutum* [15] for which genomic

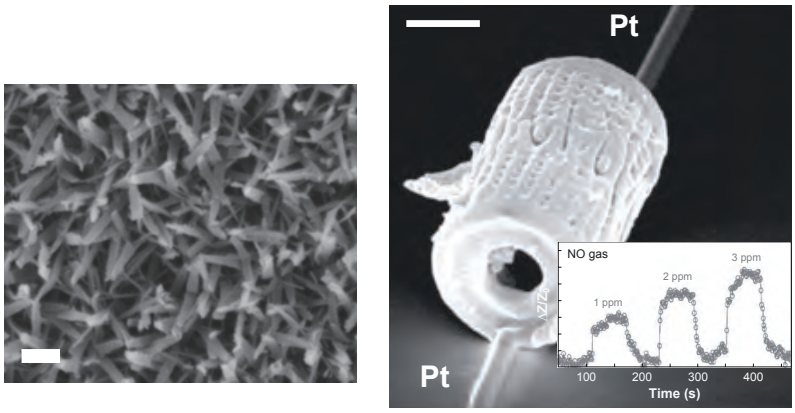

(a) (b)

Figure 11: (a) SEM image showing the morphology of a biomimetic polyethyleneimine (PEI) directed silica material [81]. (b) SEM image of a silicon replica of an *Aulacoseira* sp. cell wall with a microscale gas sensing capability. (Based on Bao et al. 2007 [8]). Scale bars, (a) 500 nm and, (b) 5 µm.

information regarding the process of biogenic silica production was identified [54].

In this process, a single cell is capable of metabolizing silica for the formation of its species-specific nanopatterned cell wall. Inside the cell, silicon transport is done by an encoding protein known as *silaffin*, for its silica affinity, and polymerized by a long chain polyamine catalyst (LCPA) [116, 54]. Proposed models for the mechanism of nanopatterned silica morphogenesis in diatoms suggest a silica deposition vesicle that participates actively in templating self-assembled organic matrices (for reviews see Kröger & Poulsen 2008 [86]).

In a recent publication, from the point of view of biomimetics, Jin & Yuan investigated silica morphogenesis by programmable self- assembly of linear polyethyleneimine, a polymer produced on industrial scale (for examples see Figure 11) [81]. However, in regards to the mechanism of biogenic silica in diatoms, there is limited insight into other proteins that constitute the silica deposition vesicle [54, 86]. Thus, in the next years, the identification of the remaining proteins involved in that mechanism will be possibly investigated using a combination of biochemistry and functional genomics.

Regarding the process of photosynthesis of diatoms, in a variety of microalgae and fungi light perception takes place in a specialized domain known as LOV that is sensitive to light, oxygen and voltage. In the two diatom genomes fully sequenced to date orthologues of LOV histidine kinases are present [15]. The LovK-LovR domains found in diatoms make a two-component signal transduction system [34, 53] which has a function of a blue-light photoreceptor [6] (for reviews on

Orthologues are genes in different species that originated from a single gene of a common ancestor.

two-component signal transduction systems see Capra & Laub 2012 [19]).

Studies of cell bioadhesion have advanced towards investigating the relationship between the cells capacity to maintain surface contact (wettability) in surfaces of distinct energies and their adhesive behavior [11, 51, 50, 66]. The usage of flow cells on self-assembled monolayers (SAMS), which are chemically well-defined surfaces, produce shear stress that is useful for quantifying the cells attachment and adhesion [88]. SAMS have also been prepared with functional groups that adsorb proteins on cell adhesion and have been considered as another approach to characterize diatom adhesion [5].

The cell biology of diatoms have influenced the creation of biodevices using live diatoms. A photobioreactor that uses living diatoms has been developed for the production of an intracellular pigmentous material [87]. In the same year, another device was made to regulate the growth of diatoms in a functionalized SAMS [130].

Biotribology at the diatom scale considers hydrodynamics; viscoelasticity and adhesion; friction, lubrication and wear.

Studying the cell motility of diatoms has been done by the analysis of diatom trajectories in controlled environments [101, 129]. A paper in 2013 probed the motility of diatoms in confined grooves by chemically stimulating the cells [129]. In that paper, according to their proposed physical model diatoms seemed to effectively minimize friction within the walls of the grooves. However, the model did not include the biotribological scale effects of diatoms [59, 60, 57, 71]. For example, the EPS that encapsulates the cell wall lubricates and reduces the interaction of a diatom with a surface in contact, as well as the adhesive trails deposited that alter the topography where diatoms glide are not mentioned. (For texts on tribology refer to "*Fundamentals of Tribology*" by Gohar & Rahnejat 2008 [64], and "*Tribology - Fundamentals and Advancements*" by Gegner 2013 [61]).

As techniques from biophysics and molecular biology continue developing the knowledge about diatoms will grow significantly in the future. However, as shown in this document, there are studies we perform on diatoms and their biofilms at the single cell level using modern experimental techniques paired with statistical analyses.

3

TETHERED BROWNIAN MOTION (TBM)

The work of this chapter follows the experimental and, to some extent, the same analysis of a technique known as tethered particle motion (TPM). However, for our study of Brownian motion we have decided upon referring to our experimental and analytical procedure as *tethered Brownian motion* (TBM).[1] During the last 20 years, single molecule studies for understanding biological processes such as protein dynamics and its interactions with DNA, have been done by analyzing individual molecules rather than their average behavior as an ensemble.

Schafer et al. introduced tethered particle motion in 1991 [121]. This approach gives information of the dynamics of individual biomolecules participating in the mechanisms of biological processes. It consists in monitoring with light microscopy the Brownian motion of a microscopic particle in solution that is anchored to a glass surface by a biomolecule such as DNA. Rather than averaging the overall particle motion, this method measures each particular trajectory and allows analysis at the single molecule level. (See Figure 12).

In molecular biology, TPM has been used to observe molecular motors like kinesin [63], RNA polymerase [121], DNA dynamics [105, 114], protein mediated loop formation in DNA [52, 138] and bending of DNA [35]. All of the mentioned publications have analyzed the particle's motion for revealing underlying macromolecular dynamics of their respective system of interest.

In our experiments, we observed the tethered Brownian motion of a microscopic particle by tracking its trajectory in time and analyzing its corresponding time series. This chapter explores the theory and limitations of tethered Brownian motion experiments, Chapter 6 is dedicated to analyzing the series.

3.1 DESCRIPTION OF TETHERED BROWNIAN MOTION

In tethered Brownian motion, the idea is that a macromolecule (for example, DNA or an adhesive nanofiber) is anchored at one end to a surface, while the other end attaches to a free microsphere that experiences no external applied forces and therefore undergoes (tethered) Brownian motion.

1 The term, tethered Brownian motion, has also been used by Beausang et al. (2007) [10] to describe the motion of a tethered particle in solution.

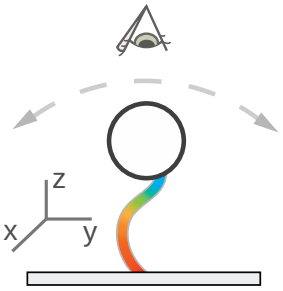

Figure 12: Tethered particle motion technique. A tether molecule is attached at one end to a point on a particle and to a glass surface on the opposite end. Because the particle does not experience external forces it is allowed to diffuse in a characteristic Brownian motion we refer to as tethered Brownian motion (TBM).

Due to the absence of external applied forces on the microsphere, the observed motion of the particle reports directly the underlying macromolecular conformation. Specifically, changes in the macromolecular tether length accompanies changes in the amplitude of the microsphere's diffusive motion.

3.2 MECHANICS OF TETHERED BROWNIAN MOTION

Tethered Brownian motion could be simulated as the Brownian motion of a particle in a Hooke's law potential well where the particle's motion is confined according to the features of the attractive potential [10].

In this model, the diffusion phenomenon and its relationship to random walk describes well the statistical dynamics of the particle. Each displacement of the particle is considered part of a series of time steps, and a step in Brownian motion is independent of previous steps. This is a stochastic process with the probability distribution of the diffusion equation;

$$u_t = \alpha^2 u_{xx} \,, \tag{1}$$

where $u(x,t)$ is the particle's position, the proportionality constant α is a property of the medium, and partial derivatives are indicated by subscripts, following the notation used by Farlow [49].

The normal distribution is of the form $P(x,t) \propto e^{-x^2/2\sigma^2(t)}$, and its first moment $< x(t) >= \int_{-\infty}^{\infty} xP(x,t)dx = 0$ gives the mean. The standard deviation is $\sigma(t) = \bar{x^2}(t)$, and is related to the variance (second moment) of the distribution $< \bar{x^2}(t) >= 2Dt$ in one dimension, where D is the diffusion coefficient and the bar indicates an average. A generalization is given by the autocorrelation function

$C := < x(t+\tau)\, x(t) >$, where the brackets denote averaging over time t. Notice that the mean square displacement, or second moment, is recovered by setting up the time $\tau = 0$.

In Figure 13a, a particle walks randomly in Brownian motion, it does not explore evenly because each step lasts longer than the correlation time τ that the particle uses to change its velocity. In Figure 13b, a particle in TBM is physically restricted to explore a range of positions in space determined by the tether elastic properties. (Panels c and d show closeups). In the simulations, most of the time particles in Brownian motion (c) will rapidly diffuse, while those in tethered Brownian motion (d) revisit places as its motion is constrained to a tighter region. (Time series of these simulated walks are in Figure 15).

In TBM, the particle is kept close to its attachment point due to an attractive potential well produced by a tension force. At a low relative extension, the tension is approximately of the form $f = -kx$ with an effective spring constant $k = 3k_BT/2L_pl$, where $k_BT = 4$ pN·nm is the thermal energy associated to a particle in solution at room temperature [122]. L_p is known as the persistence length, and l is the contour length of the polymer which serves as the tether. (Both concepts are written in detail soon in this section).

The interactions particle-substratum are modeled by Segall et al. as a hard-wall interaction that limit the conformations a tether molecule can adopt resulting in an effective stretching force on the tether.

The external forces acting on the sphere from effects due to the surface are;

- A repulsive double layer potential.
- An attractive van der Waals interaction.

  (Both of these interactions are in a scale much smaller than the typical TBM experiments and are weak in long scales, thus not involved in the particle-substratum interactions).
- A hard-wall repulsion which prevents the end point of the tether from making contact with the surface by stretching it.

The extension force due to the hard-wall force acts only in the z-direction, and at height z this force is k_BT/z [122]. For example, at 34 nm height, that is, the length of a known short tether, this force is of 0.118 pN. Compared to the force required to unfold one module of an adhesive nanofiber of a diatom, 800 pN [39], TBM experiments preserve an adhesive fiber in its native conformation and could be used as tethers.

Determining the mechanical tension on the tether is possible by analyzing the thermal motion of the particle. The tension of the molecular

1 The algorithm I wrote for the random walk simulation is in Appendix B, page 102.

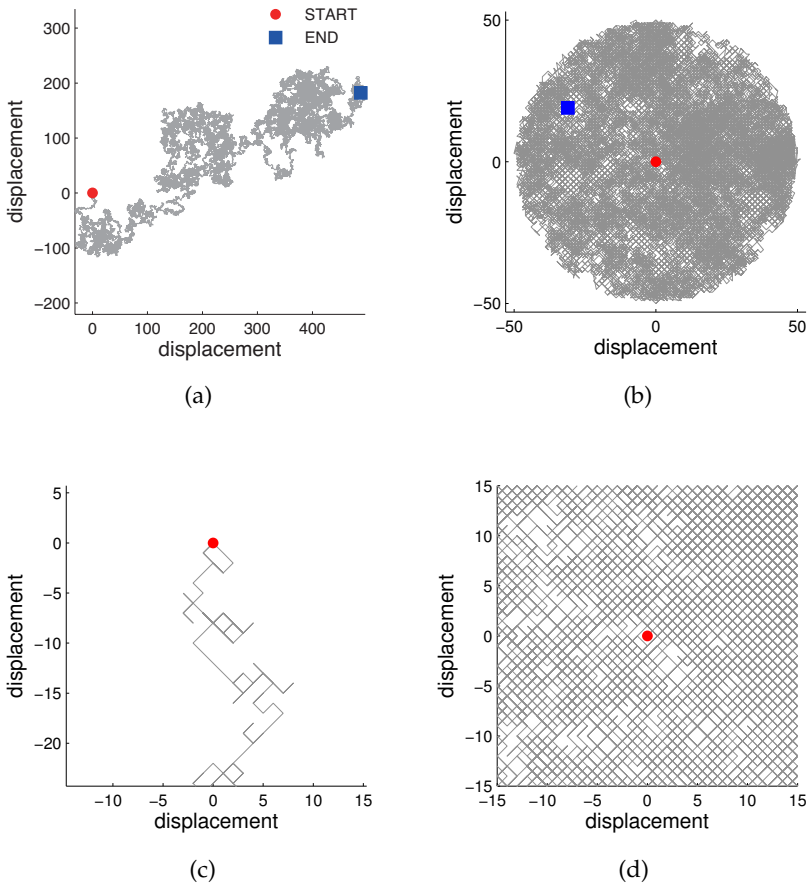

Figure 13: A simulation of (a) a particle's random walk illustrating ordinary Brownian motion, and (b) a particle's *restricted* random walk illustrating tethered Brownian motion[2]. We can see that in both types of motion the particle does not explores all space in the grid. (c) and (d) are closeups of the initial random walk steps. There are 12,000 steps for each walker, each with a probability of $^1/_2$ to move forward or backward along an axis. In (b) and (d) the tether is 50 units long.

tether is given by the particle-substratum interaction potential from the Brownian motion of the particle ϕ/k_BT, and the derivative at a certain position gives the average tension [35].

A tethered particle near to a surface originates a volume-exclusion effect that influences in the statistical properties of the tether macromolecule. The volume occupied by both the particle and the tether is the excluded volume and it is inaccessible. Volume-exclusion forces depend upon particle size and tether length. In practice, tether lengths typically range from hundred to several thousand base pairs which, is approximately 34 – 850 nm [52, 69, 105].

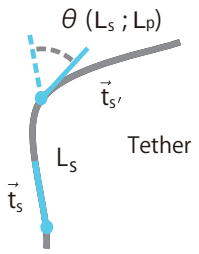

Figure 14: Model of a semiflexible biopolymer tether. The persistence length, L_p, is the length of a filament over thermal bending is appreciable. When the length L of the polymer is significantly greater than the persistence length the tangent angles at the two ends become uncorrelated. Its dynamics are governed by an entropic tension force that minimizes the end-to-end distance of the polymer to maximize the number of possible conformations.

The tether is considered a biopolymer; a number of repetitive units chemically bound[3]. If the tether is flexible, each subunit is free and independent for rotations relative to each other in a random walk fashion. In tethered Brownian motion, the particle's motion is influenced by the mechanical properties of the tethering molecule, specifically the persistence length.

PERSISTENCE LENGTH: In a filamentous polymer, the characteristic bending length scale is called the persistence length, L_p, and is mathematically defined by

$$< \mathbf{t}(s) \cdot \mathbf{t}(s\prime) >= e^{-|s-s\prime|/L_p} \ , \tag{2}$$

where the vectors $\mathbf{t}(s)$ and $\mathbf{t}(s\prime)$ are tangential at two points on a polymer separated by a distance $|s - s\prime|$. (See Figure 14).

CONTOUR LENGTH: A polymer is said to be semiflexible if the persistence length is of the order of the contour length; the length of maximum end-to-end extension.

The energy required to bend a polymer over an angle θ and length L is

$$E = k_B T \frac{L_p}{2L} \theta^2 \ , \tag{3}$$

and depends on the persistence length L_p,[4] and temperature T.

3 Molecules longer than 200 bp have been modeled as the worm-like chain (Wiggins & Nelson (2006) cited in Nelson et al. (2006)).

4 DNA is known to have a persistence length L_p = 50 nm [128], or approximately 145 bp.

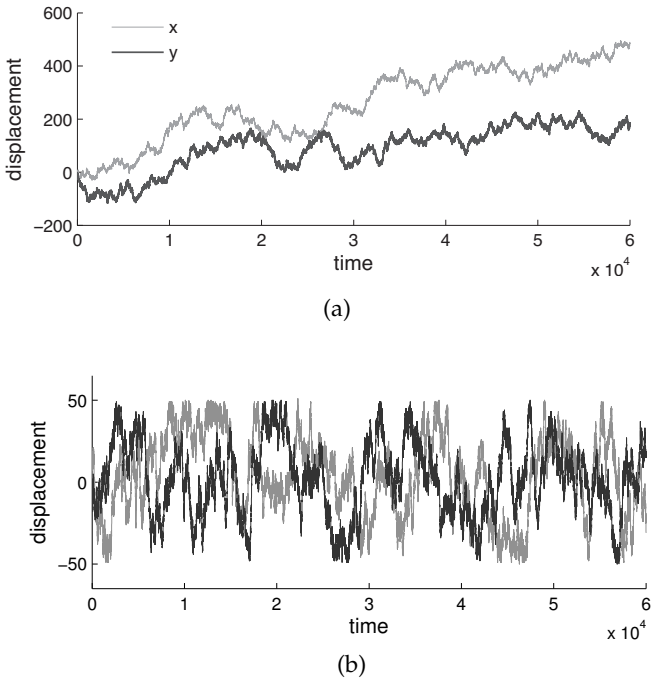

Figure 15: Simulated time series for (a) Brownian motion, and (b) tethered Brownian motion. The tether in (b) is 50 units long.

3.3 STRATEGY FOR TETHERED BROWNIAN MOTION EXPERIMENTS

TBM experiments require only a high magnification microscope equipped with digital video analysis [16, 35, 42, 69], and a choice of commercial microsphere size that is large enough to be seen with conventional optical microscopy or DIC microscopy.

The time scales involved in TPM data analysis are:

- Total observation time. The length of the time series due to changes in the amplitude of motion, or the excursions, of the microsphere.
- Exposure time. The time the video camera shutter remains open. For long exposure times more light is captured and motion is seen as a blur. Shorter times are best practice to capture rapid motion.
- Intrinsic diffusive time of the tethered particle. Is given by the variance of the normal distribution for a diffusive process,

  $t =< x^2 > /2D$.

Some of the inherent limitations in TBM are the spatial and temporal resolution which depend mostly on the tether length and particle size. The calibration curves are made using DNA molecules of different lengths, because controlling different tether lengths allows the

measurement of the corresponding microsphere motion amplitudes available for comparison with a reference value [69, 105].

These experiments have technical challenges like multiple tethering and transient sticking events. In our experiments with diatoms, the adhesive trails used as tethers slowly degrade with time (as observed by Dugdale et al. in a period of 48 – 89 hours [39]), and therefore suffer a possible loss of tethering capabilities with time. However, we did not encounter this limitation as our experimental procedures took only a couple of hours.

The experimental motion of one of the microspheres that we obtained is similar to the simulated time series of Figure 15b, a sequence of observed values in time which we further analyze using the concepts we introduce in Chapter 4.

4

DFA BY MEANS OF THE WAVELET TRANSFORM

The Detrended Fluctuation Analysis (DFA) is a method for analyzing a time series signal. A time series is a sequence of values at regularly spaced intervals in time and the goal of DFA is to reveal and characterize any possible correlation properties of the series. An interesting property of these signals is that a current observation seems to keep in memory a large set of previous observations.

Processes of this type are known as $1/f$ fluctuations or long-range correlations (LRC). They appear in the spectral density of many stochastic processes occurring in nature. They have been observed in science, economics, culturomics and music [55, 132]. Some physiological systems that have been labeled as healthy, sustainable, or adaptable are characterized by long-range correlations in their time series [30, 32, 65, 117]. This kind of correlations have been found in heartbeat dynamics [118], opening the promise of a correlation analysis which could become a macroscopic biomarker of health, providing early information for detecting patterns of disease.

In this chapter, we present the DFA method by means of the discrete orthogonal wavelet transform as a theoretical background for its application to the analysis of the time series from a system of *Nitzschia* sp. diatoms.

4.1 CORRELATION PROPERTIES OF TIME SERIES

When a time series has a mutual relationship, or correlation, within the series itself the series is said to be autocorrelated. For a time series $x(i)$, the autocorrelation function is expressed mathematically by

$$C(n) =< [x(i+n) - \mu]\,[x(i) - \mu] > , \tag{4}$$

where $< ... >$ indicates the mean value, and μ is the mean value of the series $x(i)$ [108].

In Figure 16, a *short-range correlation* occurs when the correlations of $C(n)$ decay exponentially as $C(n) \propto exp(-n/n_s)$.

A *long-range correlation* (LRC) occurs for large n values when the correlations decay asymptotically as in the power law, $C(n) \propto n^{-\gamma}$, with $0 < \gamma < 1$.

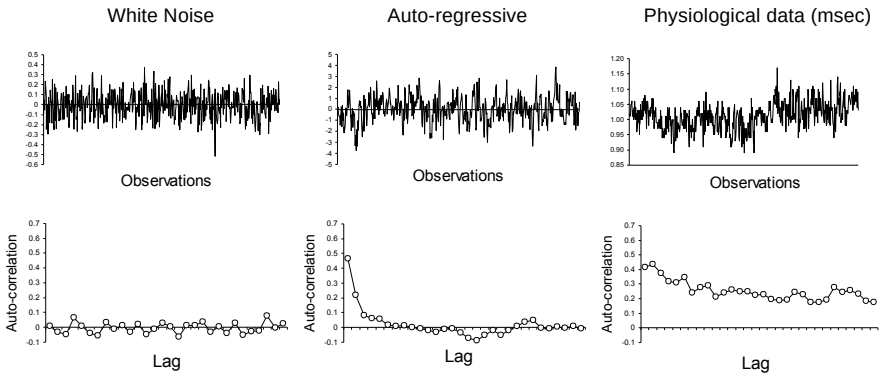

Figure 16: Time series (top row) and autocorrelation functions (bottom row). The white noise (left column) time series and autocorrelation function have a short dependence. A similar case occurs for the auto-regressive processes (middle column) which shows a serial dependence. A contrasting case is the physiological time series and autocorrelation function (right column) which shows LRC. (Based on Delignières & Marmelat 2013 [31]).

The slow decay over time means that the influence of the signal on i extends over all values $j > i$ and the sum of the correlations tend to diverge:

$$\sum_{n=i}^{\infty} C(n) \propto \sum_{n=i}^{\infty} n^{-\gamma} \propto \int_{1}^{\infty} n^{-\gamma} dn \text{ , diverges.} \tag{5}$$

In this chapter, the interest is in the detection of this last type of correlations.

Long-range correlations (LRC)

Often, one wants to know if there are correlations within the series. In Figure 17, simple operations in the original time series (top row) could evidence the presence of correlations. If the original series consists of a sample of *independent* points, when one arranges them randomly, as in the second row of the figure, then both series will look similar. This is not the case for the original series given as the example. In the middle row, a white noise signal is obtained by randomly ordering the original data which evidences that any temporal correlation between data points was lost.

The original signal could consist of the sum of independent increments $x(i+1) - x(i)$. To verify that possibility, if the original series is ordered randomly and a new series is made of the cumulative sum, it should look similar to the original. Again, this is not the case in the example as the new series (bottom row) describes a random walk that reveals that correlations in $x(i)$ are not the result of of independent increments.

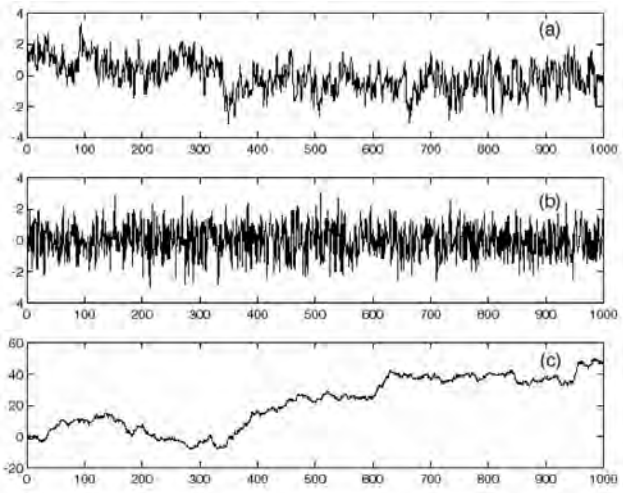

Figure 17: Evidence of correlations in time series. The original series (top). White noise (middle) obtained by randomly ordering the original data, and a random walk (bottom) obtained from the original data. See text for details. (Based on Perazzo et al. 2004 [108]).

Conceptually, LRC means that an increasing trend is likely to be followed by an increasing trend, while a decreasing trend is likely to be followed by a decreasing trend.

In analogy to random walk theory, the stochastic nature of long-range dependence in a time series has been modeled after two interrelated processes; *fractional Brownian motion* (fBm) and *fractional Gaussian noise* (fGn). fGn and fBm are invertible over differentiation and integration, respectively.

fBm is a well-developed mathematical model of strongly correlated stochastic processes that follows a scaling law, $< \Delta x^2 > \propto \Delta t^{2H}$, that gives fBm a diffusive property.

In ordinary Brownian motion, successive positions are uncorrelated, that is, each displacement in a random walk is independent of the previous.

Fractional Gaussian noise (fGn), is defined in terms of the successive increments from fBm. By differentiating fBm, one can obtain the corresponding fGn and a unique exponent H appears as the relationship between the series.

On the other hand, fBm series are non-stationary meaning their variance and moments of higher order are not invariant over time. In contrast, fGn are stationary and their statistical properties remain constant over time.

POSITIVE CORRELATION (PERSISTENT): A positive correlation means that an increasing trend in the past is likely to be followed by an increasing trend in the future. The series is said to be *persistent*.

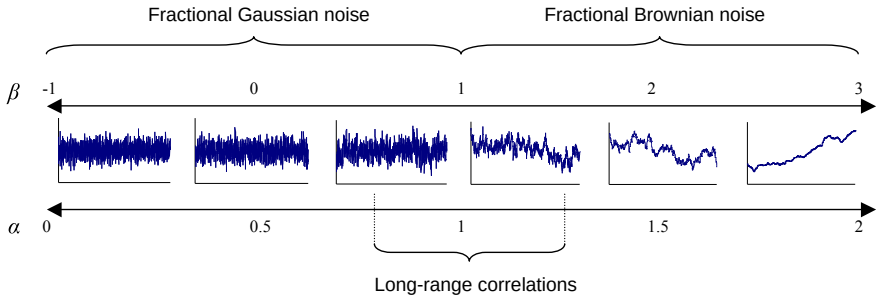

Figure 18: Representation of the fGn/fBn continuum. The fGn and fBm are characterized by a set of α and β exponents ranging from the most antipersistent to the most persistent values, and in the frontier between them is the domain of long-range correlations [31].

NEGATIVE CORRELATION (ANTIPERSISTENT): When a negative correlation occurs, an increasing trend in the past is likely to be followed by a decreasing trend in the future and viceversa. The series is said to be *antipersistent*.

The continuum represented in Figure 18 shows the range within the fGn and fBm series, which is defined by their correlations.
To know the quantities delimiting the continuum, two methods exist that exploit the frequency and temporal domains of a time series. In the frequency domain, using the power spectrum defined as the Fourier transform of the autocorrelation function of the stochastic process, one can compute the fractal exponent β if the series scale to,

$$S(f) \propto 1/f^{\beta}\,, \tag{6}$$

where the power $S(f)$ is a function of the frequency f.

In Figure 19, the exponent β is the negative of the slope of the double logarithmic plot of the power spectrum. The value of β is between -1 and 3.

In the time domain, the DFA method is used to calculate the fractal exponent α. The exponent α is the slope of the double logarithmic plot of the diffusion equation (in Figure 19). The range of α is between 0 and 2. The scaling law that arises in the time domain is,

$$\begin{cases} y(i) = \sum_{k=0}^{i} x(k) \\ \\ SD(y) \propto n^{\alpha} \end{cases} \tag{7}$$

where $y(i)$ is the integrated series of $x(i)$ and SD its standard deviation.

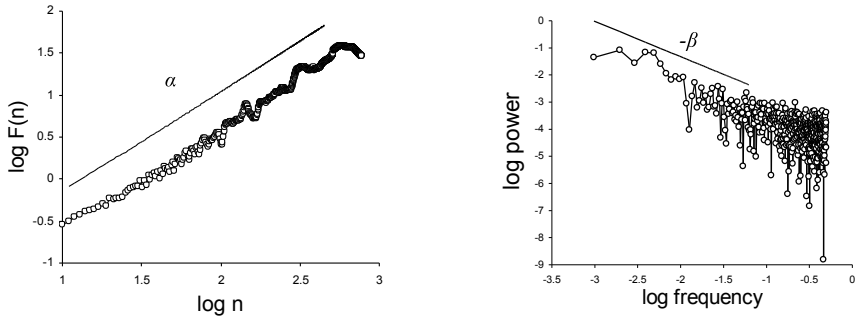

Figure 19: The fractal exponents. The exponent α (left) is the slope of the fluctuation function $F(n)$ as n varies. On the other hand, the exponent β (right) is the negative of the slope obtained from the power spectrum density [31].

*Note on self-similarity**

* This brief may be skipped without loss of continuity.

In general, LRCs and self-similarity are not the same. In the framework of stationary stochastic processes, following the discussion in Dieker (2004) [33], these are the differences:

LONG-RANGE CORRELATION: A discrete-time process X has long-range dependence or long memory, when its autocovariance function $\gamma(\cdot)$ decays slowly as $\sum_{k=0}^{\infty}\gamma(\cdot) = \infty$. Long-range dependence holds true if we assume the covariance $\gamma(\cdot)$ decays hyperbolically and the decay of the correlation follows the relation

$$\gamma(k) \propto c_\gamma |k|^{-\alpha} \,. \tag{8}$$

SELF-SIMILARITY: A continuous-time stochastic process $Y = \{Y(t) : 0 \le t < \infty\}$ is called self-similar with sub-unitary exponent H, where $0 < H < 1$, if $\{Y(at) : 0 \le t < \infty\}$ and $\{a^H Y(t) : 0 \le t < a\}$ have identical finite-dimensional distributions for all $a > 0$.

Ordinary Brownian motion has increments that are self-similar and its exponent $H = 1/2$, but are not long-range dependent. The increments in this type of motion are random walks of an independent sequence of steps. In the frontier $1/2 < H < 1$, LRC is equivalent to a weaker notion of self-similarity called 'asymptotic second-order self-similarity for stationary processes.'

On the other hand, the features of fBm are; a sequence of stationary increments; a scaling law $EB_H^2(t) = t^{2H}$; a Gaussian distribution. This features and its covariance structure function (not shown) conclude that fBm with H exponent is self-similar.

fGn is defined as the incremental process $X = \{X_k : k = 0, 1, \dots\}$ of fBm [33, 118], and it is expressed as $X_k = B_H(k+1) - B_H(k)$.

Although fGn has a different autocovariant function $\gamma(\cdot)$ than that of fBm, and follows a power law $\gamma(k) \sim H(2H-1)k^{2H-2}$ as $k \to \infty$ fGn is self-similar as well.

4.2 SCALING LAWS AND THE HURST EXPONENT

The following statistics present a technique for estimating the H parameter.

Rescaled Range Analysis (R/S)

In 1951, Harold E. Hurst developed the Rescaled Range analysis (R/S) [78]. In (R/S), a *profile* of the time series is constructed by averaging over the values of a newer series made of accumulated deviations from the arithmetic mean. With the profile, the method forms a rescaled range by standardizing each range by their corresponding standard deviation. For many subperiods ν, the rescaled range is given by

$$(R/S)_\nu \propto \nu^H \,. \tag{9}$$

To uncover the scaling law, a least squares regression on logarithms of each side is applied, so that

$$\log(R/S)_\nu \propto H \log\nu \tag{10}$$

where H is the *Hurst exponent*.

For small periods ν, the exponent is biased [26] and a larger value of ν is recommended.

The general relationships between the fractal exponents, α and β, and the Hurst exponent is given by the following set of equations [17]:

$$\text{For fGn series,} \qquad \beta = 2H - 1, \text{ and } \alpha = H \,. \tag{11}$$

$$\text{For fBm series,} \qquad \beta = 2H + 1, \text{ and } \alpha = H + 1 \,. \tag{12}$$

$$\text{For fGn and fBm series,} \quad \beta = 2\alpha + 1, \text{ and } \alpha = \tfrac{1}{2}(\beta - 1) \,. \tag{13}$$

In Figure 20, three examples of fBm series for three contrasting H exponents represent the frontier between persistent and antipersistent series.

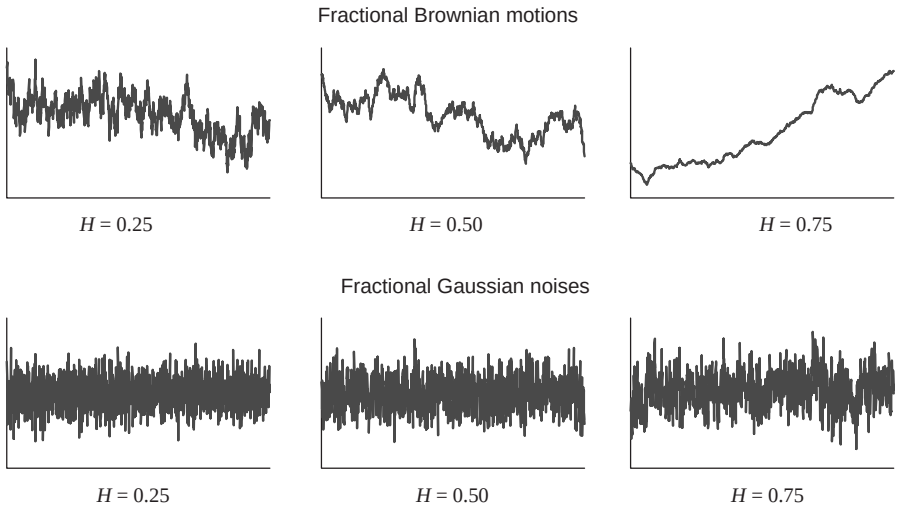

Figure 20: Three example fBm series for three constrasted H exponents and their corresponding fGn series. [31].

4.3 DETRENDED FLUCTUATION ANALYSIS METHOD (DFA)

Originally proposed by Peng et al. (1994) [107], Detrended Fluctuation Analysis (DFA) is a method that can be applied to both fGn and fBm.

1. Integrate the analyzed series $x(i)$ for each i by computing the departure from the mean of the whole series: This function is the profile.

$$Y(k) = \sum_{i=1}^{k} [x(i) - \bar{x}] \tag{14}$$

   where the bar indicates an average.

2. This series is then divided by non-overlapping intervals[1] of equal length n as exemplified in Figure 21. In each of the intervals, a monotonous trend appear and is fitted via a least-squares approach.

   A piecewise polynomial estimates each local trend within an interval. The use of linear and quadratic orders, $l = 1$ and $l = 2$, respectively, or higher order fittings of the profile correspond to a conventional DFA1, DFA2.

3. The series $X(t)$ is locally detrended by substracting from the profile $Y(k)$ of Equation 14 the values $X_n(t)$ given by the re-

1 The interval lengths are for the shortest length $n \approx 10$ and the largest $n \approx N/2$ [31].

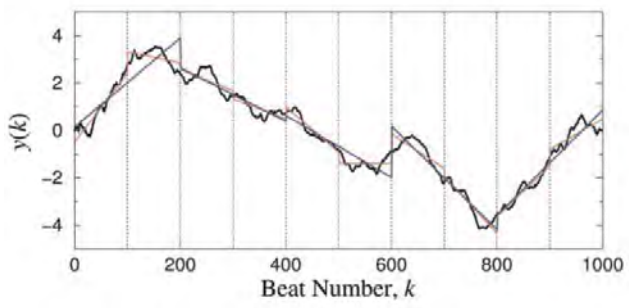

Figure 21: Illustration of the DFA algorithm applied to a human heartbeat. The solid black curve is the integrated time series, $y(k)$. The vertical lines indicate the periods of size $n = 100$ beats. The red straight line segments represent the trend estimated within each period [65].

gression; $[Y(k) - X_n(k)]^2$. The fluctuation function of the series for a given interval n is defined by:

$$F_q(M_s) := \left(\frac{1}{2M_s} \sum_{\nu=1}^{2M_s} |F^2(\nu)|^{q/2} \right)^{1/q}, \quad q = 2\,, \tag{15}$$

where M_s is the number of windows of length s.

4. Repeating the previous computation over all time scales reveals that if the fluctuation F_n increases with interval length n, and a linear relationship on a double logarithmic plot shows a scaling behavior, then such fluctuations in small intervals relate to those in larger intervals according to a power law.

$$F(n) \propto n^{\alpha} \tag{16}$$

The slope of the line in a $\log F(n)$ versus $\log n$ plot (Figure 22) determines the fractal scaling exponent α [32]).

If the series $x(i)$ is a fGn, $y(i)$ is its corresponding fBm and $\alpha = H$. However, if the series $x(i)$ is a fBm, $y(i)$ belongs to a different family of diffusive processes, then $\alpha = H + 1$ and $1 < \alpha < 3$.

To apply DFA to a time series, the appropriate length of the time series is usually made of 2^{11} points, and the minimum recommended is around 206 points [12, 32].

TWO RECENT SCALING METHODS WIDELY USED

Method 1: Multifractal Detrended Fluctuation Analysis (MF-DFA)

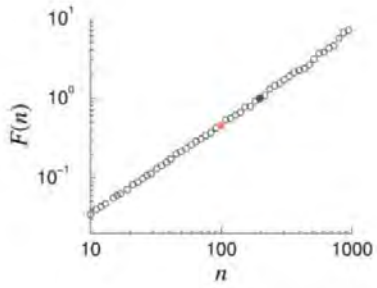

Figure 22: Illustration of the DFA algorithm applied to a human heartbeat signal. The RMS deviations $F(n)$ of Step 3 in the DFA algorithm, they are plotted against the period n in a log-log plot. The red circle is the data point for $F(100)$ (the blue circle is the data point for $F(200)$). A straight-line graph indicates scaling [65].

Multifractal Detrended Fluctuation Analysis (MF-DFA) is a generalization of the DFA method that applies to non-stationary multifractal data.

MF-DFA is based on calculating the qth order fluctuation function [82, 120],

$$F_{\mathrm{DFA},\,q}(M_s, s; m) := \left(\frac{1}{2M_s} \sum_{\nu=1}^{2M_s} |F^2(\nu, s; m)|^{q/2} \right)^{1/q}, \quad q \in \mathbb{Z}, q \neq 0 \,. \tag{17}$$

$F^2(\nu, s; m)$ is the standard deviation of the cumulative signal in a window ν of length s at level m (the importance of such level will come relevant in the next section).

Similarly to DFA, in MF-DFA the time series is divided into subperiods ν, and for each subperiod a profile is generated.

If this fluctuation scales as $F_{\mathrm{DFA},\,q}(s; m) \propto c s^{H(q)}$, where c is a constant independent of s then the $H(q)$ is known as the generalized Hurst exponent.

Method 2: Detrending moving average (DMA)

In the Detrending Moving Average (DMA), the deviations from a moving average $\bar{X}_\lambda(t)$ take in a straight forward manner the whole series.

Defining a fluctuation $F^2_{\mathrm{DMA},\,\lambda}$ as in reference [1]

$$F^2_{\mathrm{DMA},\,\lambda} = \sum_{t=\lambda}^{T} (X(t) - \bar{X}_\lambda(t))^2 \tag{18}$$

where the moving average with a time window of lag λ is

$$\bar{X}_\lambda(t) = \sum_{k=0}^{\lambda-1} X(t-\lambda) \tag{19}$$

The fluctuation then scales as

$$F^2_{DMA,\,\lambda} \approx c\lambda^{2H} \,. \tag{20}$$

The moving average can be applied backward and forward, or it could start from the center.

The Detrending Moving Average analysis does not divide the time series into subperiods, in contrast to the (R/S), DFA and MF-DFA.

4.4 WAVELETS AND WAVELET TRANSFORM

In 1982, Jean Morlet and collaborators introduced wavelets as families of functions constructed by using translations and dilations of a single function that is known as the *mother wavelet* for the analysis of non-stationary signals.

The Fourier transform analysis does not provide the local information of the signals and cannot be used for analyzing signals in a joint time and frequency domain. In contrast, a wavelet approach includes the temporal as well as the spatial information [91, 123, 126].

The dynamics of non-stationary signals in a time series are revealed with techniques such as the DFA by separating carefully fluctuations off the trend in a time interval. In this case, a fast wavelet transform decomposes the original signal in levels of approximation and detail, which leads to the optimization of DFA computations.

The simplest mathematical wavelets are *Haar's wavelets*, which as any wavelet employ dilations described by a parameter a, and shifts or translations described by a parameter b of mathematical functions. The scaled-translated wavelet, or daughter wavelet is defined by

$$\psi_{a,b}(t) := \frac{1}{\sqrt{a}}\psi\left(\frac{t-b}{a}\right) \,, \tag{21}$$

where a is a scale parameter that contracts ($0 < a < 1$) or expands ($a > 1$), and b is the translation [79, 72, 102]. $\frac{1}{\sqrt{a}}$ is a normalization coefficient, and in Equation 21, the parameter a dictates the dilation of the temporal variable $(t-b)$.

In Figure 23, the Haar wavelet function for three different scales and translation combinations is shown. When $a < 1$ the wavelet contracts and when $a > 1$ it expands.

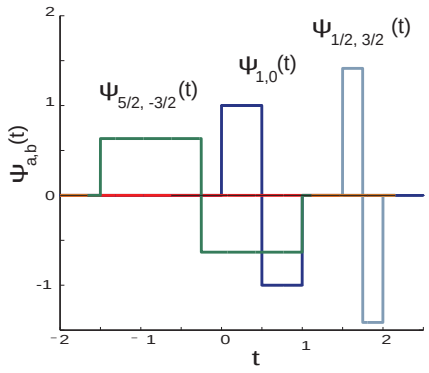

Figure 23: Haar wavelets $\psi_{a,b}(t)$ illustrating scaling parameters for $a = 5/2, 1, 1/2$, $b = -5/2, 0, 3/2$. When $a > 1$ ($a < 1$) the wavelet function expands (contracts). When $b > 1$ ($b < 1$) the wavelet function shifts along the positive (negative) axis. (Based on Murguía & Rosu 2011 [102]).

The function $\psi(t)$ is said to be a wavelet if and only if its Fourier transform, $\hat{\psi}(\omega) = \int \exp(i\omega t)\psi(t)dt$ satisfies the admissibility condition proposed by Daubechies [28],

$$C_\psi = \int_0^\infty \frac{|\hat{\psi}(\omega)|^2}{|\omega|} d\omega < \infty \, , \tag{22}$$

The condition implies that the wavelet $\psi(t)$ is oscillatory or of finite energy. Mathematically, it satisfies

$$\int_{-\infty}^{\infty} \psi(t)dt = \hat{\psi}(0) = 0 \, . \tag{23}$$

where $\hat{\psi}(t)$ is the complex conjugate of $\psi(t)$.

A signal $x(t)$ of finite energy is usually detected in discrete form and can be approximated in series using an orthonormal wavelet basis [67, 102, 104],

$$x(t) = \sum_m \sum_n d_{m,n}\psi_{m,n}(t) \tag{24}$$

with coefficients,

$$d_{m,n} = \int_{-\infty}^{\infty} x(t)\psi_{m,n}(t)dt \, . \tag{25}$$

These orthonormal basis are referred as the *analyzing wavelet* $\psi(t)$, $\psi_{m,n} = 2^{m/2}\psi(2^m t - n)$ with m and n, the scaling parameter and the translation parameter, respectively.

In 1998, Mallat [92] proposed an efficient method to calculate Equation 24 and Equation 25 via multiresolution analysis. This analysis

consists in constructing an orthogonal wavelet basis by a successive decomposition of the original series in a low and high frequency level known as the approximation and the detail, respectively. The repeated multilevel decomposition of the series results into a fast wavelet transform (FWT) (see Figure 24).

To a wavelet function $\psi(t)$, there is an associated scaling function $\varphi(t)$, and scaling coefficients $a_{m,n}$.

The scaling functions are expressed as $\{\varphi_{m,n}(t)\}$, where,

$$\varphi_{m,n}(t) = 2^{m/2}\varphi(2^m t - n) \ . \tag{26}$$

Then,

$$\varphi(t) = \sum_k h_\varphi \sqrt{2}\varphi(2t - k) \ . \tag{27}$$

In Equation 26 and Equation 27 the shifts have integer values.

Orthogonal wavelet basis

The orthogonal basis is constructed by the scaling coefficients computed at the next finer level $m + 1$ by the following fast wavelet transform (FWT),

$$a_{m,n} = \sum_k h[k - 2n] a_{m+1,k} \tag{28}$$

$$d_{m,n} = \sum_k g[k - 2n] a_{m+1,k} \tag{29}$$

where $h[n]$ and $g[n]$ are the lowpass and highpass filters, respectively.

The construction of the original scaling coefficients $a_{m,n}$ by combining scaling and wavelet coefficients,

$$a_{m+1,n} = \sum_k (h[2k - n] a_{m,k} + g[2k - n] d_{m,k}) \tag{30}$$

represents the inverse fast wavelet transform for computing Equation 24.

According to the multiresolution analysis, an arbitrary signal is approximated by the scaling and wavelet series as follows,

$$x(t) = \sum_n a_{m_0,n} \varphi_{m_0,n}(t) + \sum_n \sum_{m=r_0}^{M-1} d_{m,n} \psi_{m,n}(t) \tag{31}$$

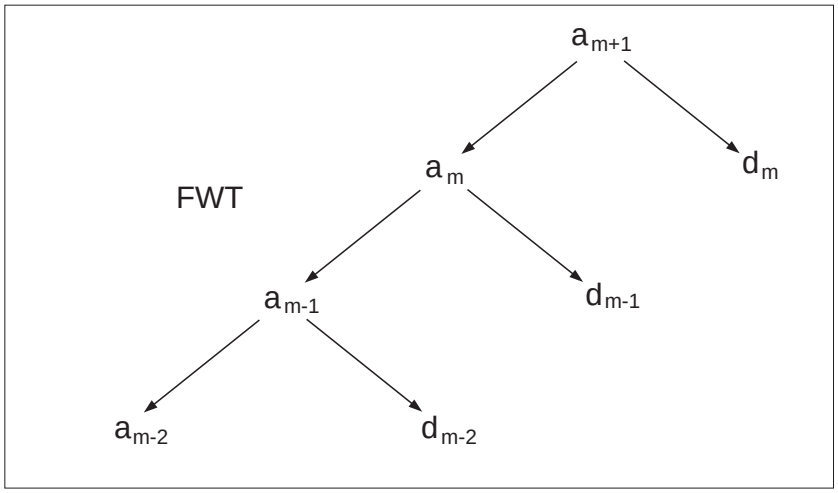

Figure 24: The structure of a three-level decomposition process of the wavelet transform (FWT) in multiresolution analysis (MRA). Beginning from level $a_{n,m+1}$, the next finer level $m+1$ of a 2^k value signal in MRA is $a_{n,m}$. For each iteration of the FWT a scaling coefficient $a_{n,m}$ has a corresponding wavelet coefficient $b_{n,m-1}$. (Based on Murguía & Rosu 2011 [102]).

where the first term is the set V_0 with the shifted version of the scaling function $\varphi_{r_0,s}(x)$ weighted by $a_{m_0,n}$ [103, 67]. The second term contains the possible shifted versions of the wavelet $\psi_{m,n}(x)$.

In Equation 31 the scaling coefficients are given by,

$$a_{m,n} = \int x(t)\varphi_{m,n}(t)dt \tag{32}$$

whereas the wavelet coefficients are defined by:

$$d_{m,n} = \int x(t)\psi_{m,n}(t)dt\ . \tag{33}$$

Part II

EXPERIMENTAL PROTOCOLS, ANALYSES AND RESULTS

This part contains a chapter about the experimental protocols for the two main experiments done in this work, tethered Brownian motion and diatom cell motility. In addition, the analyses and the results of these experiments are presented in separate chapters.

5

EXPERIMENTAL PROTOCOLS

This chapter contains the experimental procedure for two experiments done with *Nitzschia* sp. diatoms. Each section covers one experiment and details its corresponding protocol to reproduce it. Please see Appendix A p. 91 for details regarding how I grew the subcultures and prepared its culture medium.

5.1 TBM ASSAY PROTOCOLS

The motivation of this experiment comes from the observation made by Lind et al. (1997) of diatoms and their adhesive EPS interacting with silica microspheres. As diatoms glided, these deposited adhesive biofilms in the form of trails over a glass substrate and microspheres were observed to attach and align along the trails [89]. A couple of years later, Poulsen et al. (1999) discovered that the gliding of diatoms is due to an acting-myosin motility system in which actin cables are connected to the extracellular adhesive strands of diatoms [115].

Through single molecule studies with AFM, Dugdale et al. (2005) discovered modular proteins as the main constituent of the extracellular strands known now as adhesive nanofibers [39]. Using the AFM tip to test the tethering capability of diatom adhesives allowed them to distinguish between single and multiple nanofibers. A year later, Chiovitti et al. (2006) observed the adhesion and interaction of silica microspheres along the raphe of diatoms [21]. The diatom cell adhesion and motility is mediated by an adhesive EPS secreted from a slit in the diatom's cell wall structure, known as the raphe.

In our experiment, we tested the tethered particle motion (TPM) technique with light microscopy and motion capture of silica microspheres interacting with the biofilms formed by the gliding of *Nitzschia* sp. diatoms. The TPM data was analyzed and the motion of the tethered microspheres was characterized by a Detrended Fluctuation Analysis (DFA) in p. 55.

Figure 25 shows a schematic situation where diatoms glide leaving an adhesive trail behind to which a microsphere in solution attaches to and forms a tether with an adhesive nanofiber.

We captured the motion of a tethered microsphere in video as observed along the optical axis. Tethered particle samples self-form inside a 8 – 10 µL flow cell where we had no external control. All experiments were done at room temperature of 22 °C as in other publications [48]. Our equipment permits data acquisition in two dimen-

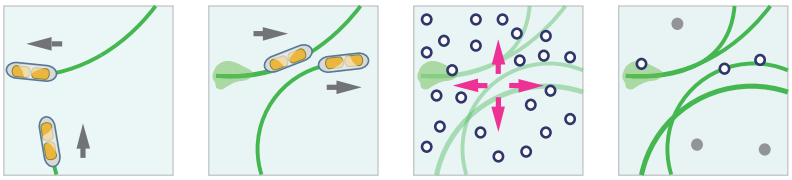

(a) (b) (c) (d)

Figure 25: The TBM experimental design. (a) Initially, diatoms glide, (b) and after several minutes adhesive trails and biofilms form. (c) Presence of freely diffusive microspheres (exaggerated in size) are added to the sample. Washing the sample with a stream of culture medium leaves (d) tethered microspheres (bright color) and unbound microspheres (dark color). As shown, tethered microspheres are anchored to a point around trails or biofilms and exhibit TBM. (Microspheres adhered to or near a diatom cell wall are not discussed in this work).

sions, which according to the features of TBM detailed in Ch. 3, for our goals is not considered a limitation [122, 69]. Extending to three dimensions has been done with evanescent fields or diffraction rings by Blumberg et al. [13].

5.1.1 *Materials*

- Diatoms: A culture of freshwater *Nitzschia* sp. diatoms grown in a 500 µL flask containing culture medium with constant air bubbling. The cultures were 7 days old and were stored at the IM-UASLP Geomicrobiología laboratory,[1] in a light and temperature controlled room (14 : 10 h light/dark cycle at 25 °C).
- Culture medium: Fresh Woods Hole culture medium at pH 7.0 (see Appendix A, p. 91 for the preparation method).
- Microspheres: Streptavidin-coated polystyrene spheres (Spherotech) of 1.26 µm in diameter. These are stored in a refrigerator.

5.1.2 *Experimental setup*

- Centrifuge (MIKKRO 120, Hettich).
- Light microscope: The microscope is an upright optical microscope equipped with an oil-immersion objective (AmScope, 100×, NA = 1.25) and a 10 MP digital camera (AmScope).

1 Contact: Dr. J. Viridiana García Meza
550 Sierra Leona, Lomas 2a, 78210, San Luis Potosí, SLP, México
Phone: 52 (444) 825 – 3426, jvgm@uaslp.mx

- Computer: Windows7 OS (Microsoft) computer with an Nvidia video card and wired to the microscope. VirtualDUB 1.9.11 (SourceForge.net) for video capture and processing.

5.1.3 *Experimental procedure*

Take a 400 – 500 µL sample of resuspended diatoms from the culture in a centrifuge tube and 200 – 300 mL of fresh Woods Hole culture medium, then transfer them to IPICYT (5-minute commute time) and immediately vortex the sample for 30 seconds. The sample is left in a rotor to prevent sedimentation and formation of diatom aggregates while the following solutions are prepared.

Microsphere solution

- Spheres & Milli-Q water (1 : 100) dilution.

  1 µL microspheres.

  99 µL filtrated Milli-Q water (available from the DBM-IPICYT laboratory).[2]

  Sonicate the solution for 30 minutes.

- Spheres & Milli-Q & culture medium dilution.

  Transfer 20 µL of the 1 : 100 sphere-Milli-Q dilution into a new centrifuge tube.

  Add 80 µL Woods Hole culture medium.

Diatom samples

We recommend the washing of diatoms by removing and replacing their culture medium; We have seen higher motility rates in *Nitzschia* sp. diatoms when we removed the soluble EPS that is found dissolved in the medium and replaced with fresh medium. The details and importance on removing the soluble EPS matrix from diatom samples can be read in p. 94.

- Add 300 µL diatoms to a centrifuge tube.
- Centrifuge at 5000 rpm for 2 minutes.
- Carefully remove an approximate of 285 µL of supernatant. This volume depends on the visible diatom pellet size and can be adjusted easily.

2 Contact: Dr. Gerardo Rafael Argüello Astorga
2055 Camino a la Presa San José, Lomas 4a, 78216, San Luis Potosí, SLP, México
Phone: 52 (444) 834 – 2000, grarguel@ipicyt.edu.mx

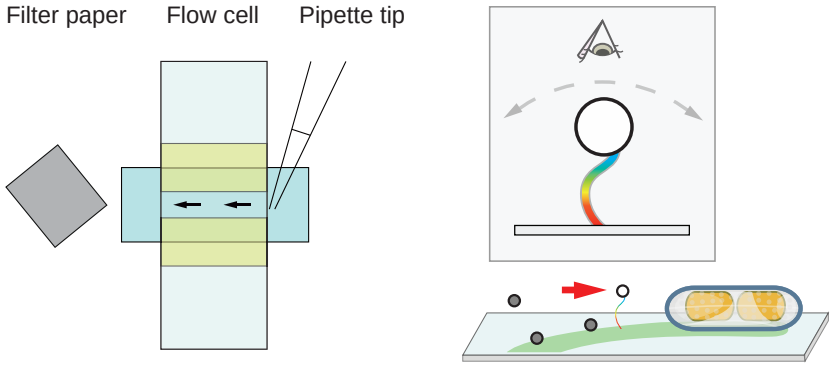

(a) (b)

Figure 26: Formation of adhesive tethers inside a flow cell. (a) Block scheme of a flow cell. When adding another solution inside the flow cell, a filter paper on one end is placed to absorb and allow remove the volume of the current solution while flowing a newer solution on the opposite end of the flow cell. (b) The resulting TBM local system. Inset: a particle tethered to an adhesive nanofiber.

- Add 285 µL of fresh culture medium.
- Vortex until the mixture looks homogenous.

  (Centrifuge and replace the culture medium if needed).
- Transfer the contents to a new centrifuge tube to avoid adhesive pads deposited in the tube walls possibly influence the diatom motility in the assay.

Usage of flow cell

- *Assembly of a flow cell for tethered Brownian motion assays* [4]: Clean a microscope glass slide and coverslip with ethanol, then stick two pieces of double-sided tape to a glass slide leaving a 3 – 4 mm wide channel in between, and remove excess tape from the glass border with a razor edge. Place a coverslip on top of the tape and gently push as to adhere it uniformly while removing air bubbles trapped between the tape and the cover. Figure 26a shows an illustration of an assembled flow cell.
- *Flowing a solution into the flow cell*: At one end of the flow cell as in Figure 26a, place the pipette tip and flow 9 µL of diatom solution which will run into the flow cell by capillary action.
- Incubate for 90-minutes inside a closed Petri dish. Add a few drops of culture medium on both ends of the flow cell to prevent the sample from drying.

Formation of adhesive tethers

During the time of incubation, diatoms left adhesive trails as they glided across the glass slide and coverslip. We have placed immediately the flow cell in an optical microscope and observed diatoms gliding. However, in order to have higher motility rates and larger quantities of biofilms (details in Appendix A, p. 95), we let the sample sit for an incubation time after flowing diatoms into the flow cell.

- After 90-minute incubation time, slowly add 10 µL of the Spheres & Milli-Q & culture medium solution into the flow cell using a filter paper as in Figure 26a to displace the current liquid.
- Add drops of culture medium on both ends of the cell and incubate for 45 minutes inside the Petri dish. This is an additional time we give to spheres to adhere to adhesive nanofiber tethers.
- After a 45-minute period, use the filter paper to slowly wash with 1 mL of culture medium any unbound sphere.
- Finally, seal both ends of the flow cell with a wax syringe.

Sealed flow cells enable us to observe samples over several hours with out internal currents that could perturb the assays.

Experimental control

Our control sample contained microspheres in culture medium and Milli-Q water with 1 : 1000 concentration but absent of diatoms. Microspheres diffused freely in ordinary Brownian motion and did not stick to the chamber walls other than occasionally. Only when diatoms where present we could observe microspheres in a limited motion as in TBM.

Light microscopy

We used conventional optical microscopy in video mode to observe polystyrene microspheres exhibiting TBM near gliding *Nitzschia* sp. diatoms. The size of the microspheres, 1.26 µm, is within the diffraction limit and is suitable for this kind of microscopy. Smaller spheres, 400 nm, were too small to be distinguished with the eye and video camera.

It is known that blurring of the image reduces the apparent amplitude of the microsphere observed in digital video recordings (Allemand (1997) in Nelson et al. (2006)). For our 1.26 µm spheres we choose an exposure time slightly shorter than the time required for the sphere to travel its range of motion σ, by $t \approx \sigma^2/D$, where the diffusion coefficient $D \approx 1000\ \mathrm{nm}^2/\mathrm{ms}$. The exposure time calculated is 400 ms, but instead we use 40 ms; the lowest exposure time the spheres remained

Figure 27: Light micrograph of a *Nitzschia* sp. diatom and a short microsphere trail. In our selection criteria, 1.26 µm sized spheres presenting TBM (dark arrows) have been captured in video whereas stuck or freely diffusing spheres (bright arrows) have been discarded. The bar scale is 10 µm.

visible on screen and the time that allowed us to have average frame rates of 25 fps. This is a valid exposure time and frame rate used in previous publications [93, 105, 137].

The flow cell was placed on the specimen holder of an upright microscope. Many tethered microspheres can be recorded simultaneously in a single run as reported in Beausang & Nelson [9]. We observed 10 – 20 mobile microspheres within each field of view of the microscope, and after observing for several minutes, spheres presenting TBM were captured in video whereas stuck or freely diffusing spheres were discarded (see Figure 27). When spheres of interest were at the borders of the field of view the stage was repositioned because chromatic aberration is not appreciable at the central region.

Videos were digitized with VirtualDUB 1.9.11 as uncompressed `avi` files, and each frame was exported as text images in ImageJ 1.46 (National Institutes of Health). Object tracking was done with an in-house LabVIEW routine (National Instruments, Austin, TX). (For details about the digital video processing and tracking algorithm see Appendix B p. 97). The analysis of TBM assays starts by a tracking algorithm that determines the in-plane position of a tethered sphere and stores it for each video frame [13]. Raw positional data is subject of drift due to vibrations of the microscope and tracking error. In the analysis chapter (p. 55), we applied a high-pass filter and a moving average [69] to correct for drift, then we perform scaling analyses to the drift corrected time series.

5.2 CELL MOTILITY ASSAY PROTOCOLS

In the second experiment, we captured on video live *Nitzschia* sp. diatoms gliding. The goal in this assay is to visualize diatom motility in a non-invasive set up and collect data for quantifying the kinematics and the underlying features of the time series of diatom migrations.

To motivate this study, diatom gliding motility has been studied systematically since the 1960's in search for evidence that explain their type of motility and also for ecological purposes (Harper & Harper 1967 [70], and Drum & Hopkins 1966 [38] cited in Edgar & Pickett-Heaps 1983 [45]). Even thirty years ago, computers and motion capture have been used to aid the measurements of these types of experiments as in Edgar 1979 [43] cited in Edgar & Pickett-Heaps 1983 [45].

In the last decade, diatom trajectories have been visualized by altering the adhesive trails with attached silica microspheres [74], stain-

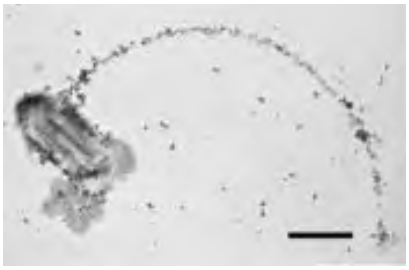

(a)

(b)

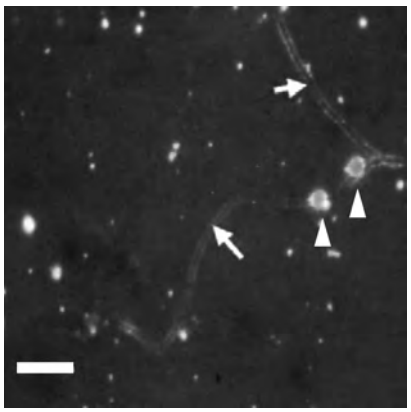

(c)

Figure 28: Previously reported diatom trajectories. Light micrographs of (a) silica microspheres adhered to a diatom trail [74] and, (b) stained trails deposited on a glass surface after 30 min [96]. (c) Fluorescent image of trails (arrows) and of diatoms in motion (arrowheads) [135]. Con-A was used in (c) as a fluorescence-based glucose sensor, it degrades by diffusion or photobleaching [111]. *Amphora coffeaeformis* diatoms appear in these panels. Scale bars, (a) 25 μm, (b) NA and, (c) 50 μm.

ing techniques [96], and fluorescent microscopy [135] (see Figure 28a, Figure 28b, and Figure 28c, respectively). These type of experiments can be considered invasive because the addition of particles or chemicals can influence the motion of diatoms. In addition, the staining degrades with light and halts the cells, and the fluorophores degrade by diffusion or photobleaching.

During the same decade, diatom trajectories have been observed with optical microscopy, captured in video and visualized in a computer screen. This approach allowed them to quantify kinematic parameters for certain natural situations such as diatom dispersing from a cellular aggregate [136], and for in-lab situations as diatom motion in confined regions [101] and motion along custom made tracks [129]. (See Figure 29a, Figure 29b, and Figure 29c, respectively).

In our experiment, a diatom sample from an axenic culture of *Nitzschia* sp. during their exponential phase of growth was placed inside a flow cell where cells could adhere and glide freely.

If individual diatoms could be observed moving freely for several minutes then information about their motility could be obtained by studying their trajectories. When diatoms are in their exponential phase of growth, the rate of motile diatoms is optimal [68] and if these are able to migrate in a natural fashion their motility could be investigated non-invasively. A proper characterization and understanding of this particular case of motion is a requirement for the study of motility in other controllable conditions.

The conditions that can be controllable in this assay are the following: The quality and growth phase of the diatom culture; Soluble EPS can be removed post-centrifugation; The concentration of the diatom inoculate; The width of the flow cell; The type of illumination in optical microscopy used for visualizing cells.

Once the flow cell is sealed in the assay, the motion of diatoms is not controlled externally in any way.

5.2.1 *Materials*

- Diatoms: A culture of freshwater *Nitzschia* sp. diatoms grown in a 500 µL flask containing culture medium with constant air bubbling. The cultures were 8 days old and were stored at the IM-UASLP Geomicrobiología laboratory,[3] in a light and temperature controlled room (14 : 10 h light/dark cycle at 25 °C).
- Culture medium: Fresh Woods Hole culture medium at pH 7.0 (see Appendix A, p. 91 for the preparation method).

3 Contact: Dr. J. Viridiana García Meza
550 Sierra Leona, Lomas 2a, 78210, San Luis Potosí, SLP, México
Phone: 52 (444) 825 – 3426, jvgm@uaslp.mx

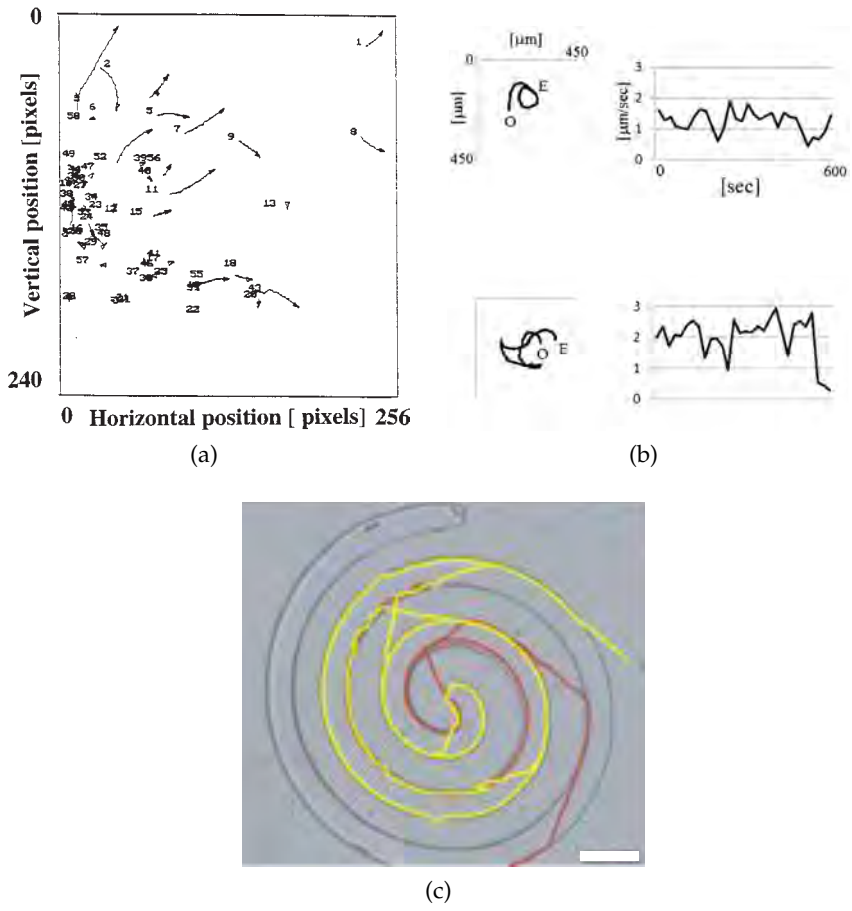

(a) (b)

(c)

Figure 29: Previously reported diatom trajectories. Computer-generated tracks of (a) diatoms dispersing from a cellular aggregate, where arrows indicate their direction of gliding during 100 s [136] and, (b) trajectories of two diatoms inside a micro-chamber shown next to their corresponding time series [101]. (c) Light micrograph of a diatom gliding on a groove [129]. Scale bar is 100 µm.

5.2.2 *Experimental setup*

- Centrifuge (MIKKRO 120, Hettich).
- Light microscope: The microscope is an upright optical microscope equipped with an oil-immersion objective (AmScope, 10×, NA = 1.25) and a 10 MP digital camera (AmScope).
- Computer: Windows7 OS (Microsoft) computer with an Nvidia video card and wired to the microscope. VirtualDUB 1.9.11 (SourceForge.net) for video capture and processing.

5.2.3 *Experimental procedure*

Take a 400 – 500 µL sample of resuspended diatoms from the culture in a centrifuge tube and 200 – 300 mL of fresh Woods Hole culture

medium, then transfer them to IPICYT (5-minute commute time) and immediately vortex the sample for 30 seconds. The sample is left in a rotor to prevent sedimentation and formation of diatom aggregates while a flow cell is assembled (see Figure 26a).

Diatom samples

We recommend the washing of diatoms by removing and replacing their culture medium; We have seen higher motility rates in *Nitzschia* sp. diatoms when we removed the soluble EPS that is found dissolved in the medium and replaced with fresh medium. The details and importance on removing the soluble EPS matrix from diatoms can be read in p. 94.

- Add 300 µL diatoms to a centrifuge tube.
- Centrifuge at 5000 rpm for 2 minutes.
- Carefully remove an approximate of 285 µL of supernatant. This volume depends on the visible diatom pellet size and can be adjusted easily.
- Add 285 µL of fresh culture medium.
- Vortex until the mixture looks homogenous.

  (Centrifuge and replace the culture medium if needed).
- Transfer the contents to a new centrifuge tube to avoid adhesive pads deposited in the tube walls possibly influence the diatom motility in the assay.

We inoculate the diatom sample inside a flow cell as described in p. 46. We have placed immediately the flow cell in an optical microscope and observed diatoms gliding. However, in order to have higher motility rates (details in Appendix A, p. 95), we let the sample sit for an incubation time of 90 min. after flowing diatoms into the flow cell.

Sealed flow cells enable us to observe samples over several hours with out internal currents that could perturb the assays.

Light microscopy

The flow cell was placed on the specimen holder of an upright microscope to observe gliding *Nitzschia* sp. diatoms. The size of these cells is about 30 µm. Several diatoms can be recorded simultaneously in a single run, 2 – 17 diatoms were observed within each field of view of the microscope. After observing the sample for several seconds, diatoms gliding at approximately 5 µm/s were captured in video (see Figure 30).

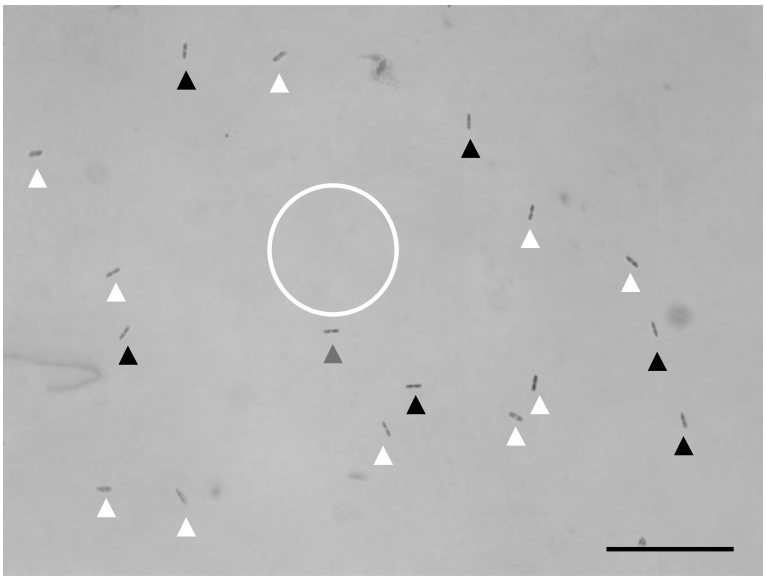

Figure 30: Video frame from the diatom motility assay. Light microscopy field of view of gliding *Nitzschia* sp. diatoms (dark arrowheads) and immobile diatoms (bright arrowheads). The cell near the center of the field (mid-tone arrowhead) moved in multiple directions along a circular trajectory indicated by the bright circle. (The radius of the circular trajectory illustrated is a close approximation of its true size). The bar scale is 200 µm.

Videos were digitized with VirtualDUB 1.9.11 as uncompressed `avi` files, and each frame was exported as text images in ImageJ 1.46 (National Institutes of Health). Object tracking was done with an in-house LabVIEW routine (National Instruments, Austin, TX). (For details about the digital video processing and tracking algorithm see Appendix B p. 97). The analysis of the two dimensional diatom trajectories starts by a tracking algorithm that determines the in-plane position of a single diatom and stores it for each video frame [13]. Raw positional data is subject of drift due to vibrations of the microscope and tracking error. In the analysis chapter (p. 65), we applied a high pass filter and a moving average [69] to correct for drift, then we perform scaling analyses to the drift corrected time series.

6

TBM: ANALYSIS AND RESULTS

This chapter is dedicated to the analyses of the experimental time series originating from the tethered Brownian motion (TBM) of polystyrene microspheres. From the observations made in an in-lab control type of experiment, the microspheres attached to tethers were determined to be adhesive nanofibers (ANFs) complexes from biofilms associated to the *Nitzschia* sp. diatom. The Detrended Fluctuation Analysis by means of a fast wavelet transform method (WT-DFA) is applied to the time series described.

6.1 SCALING ANALYSES OF TBM

The motion of microspheres in TBM was obtained by a post process of video microscopy and an in-house computer tracking routine. One hundred microspheres were captured in video and only 13 of them were confirmed to present TBM for the full length of observation. The WT-DFA analyses were performed on 10 of them.

Videos captured digitally (26 fps) from the TBM assay went under a basic digital image processing of cropping, color inversion and file format conversion. The video frame format conversion and the tracking routine are fully detailed in Appendix B, p. 97.

Precision of the microsphere position measurement

To determine the precision of the measured positions by the tracking routine, we use videos of microspheres at rest and assigned one sphere as the reference position to which we compared the position of other immobile spheres relative to the reference.

In Figure 31, the computed tracking positions of the reference microsphere No. 1, microsphere No. 2 and their corresponding time series (left and right columns, respectively) are shown. Lastly, their position difference is also shown. The standard deviation of the position difference is 56.0 nm and 58.4 nm for the x and y coordinates, respectively, suggesting a precision of the measurements of microsphere positions of 56 – 59 nm or better can be obtained with the experimental equipment and computer tracking routine.

Tethered particle motion approach

Our initial approach for the study of tethered Brownian motion was to test a well-developed technique known as Tethered particle motion

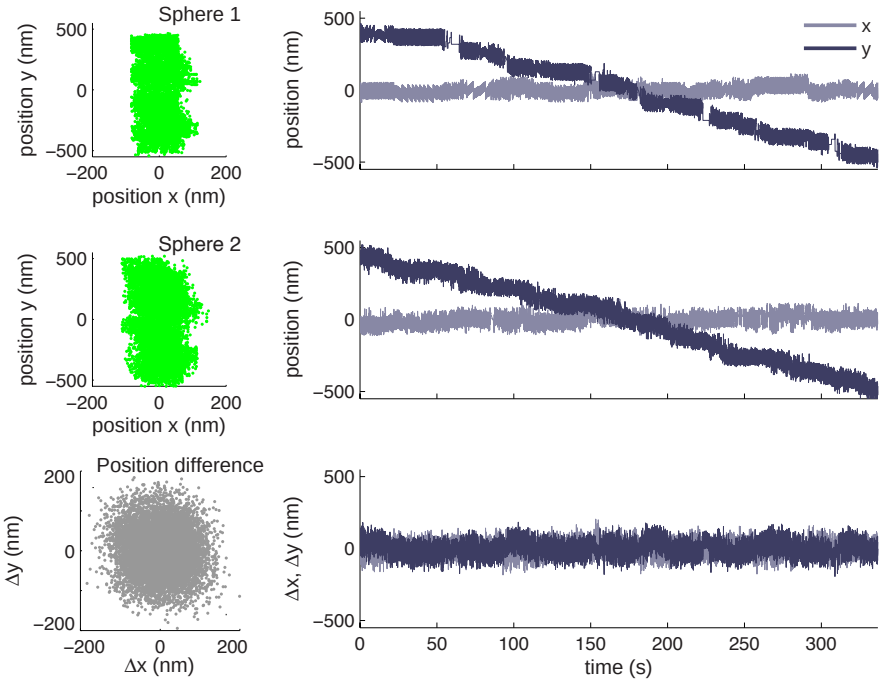

Figure 31: Precision of the position measurements by analyzing two immobile microspheres.

(TPM) that is used to study conformational properties of biological macromolecules, such as DNA, and apply it to a system of biofilms formed by diatoms.

Following the complete established TPM protocols [52, 69, 114] with our current equipment was not possible for two reasons; first, the length of an ANF tether was unknown due to the nature of the experiment; secondly, the experimental design did not satisfied the spatial and temporal resolutions of TPM [69].

The spatial resolution in TPM is interrelated to the temporal resolution, meaning that the combined motion of tethered particles and their respective tethers(the coupled TPM system) dictates the sensibility of the TPM measurements and qualifies them as resolvable. If the measurements are outside the boundary imposed by the coupled TPM system then the measurements are not reliable.

In the case of a coupled TPM system of 1.2 μm spheres tethered to ANFs and detected by optical microscopy with bright field illumination, the corresponding time series were not resolvable by TPM. According to the literature [69, 85, 114], a time series whose $< RMS_t >$ function fits an exponential function and is outside of the asymptotic region is considered resolvable. In our experiments shown in Figure 32, the coupled TPM system was in the asymptotic region even at the shortest times.

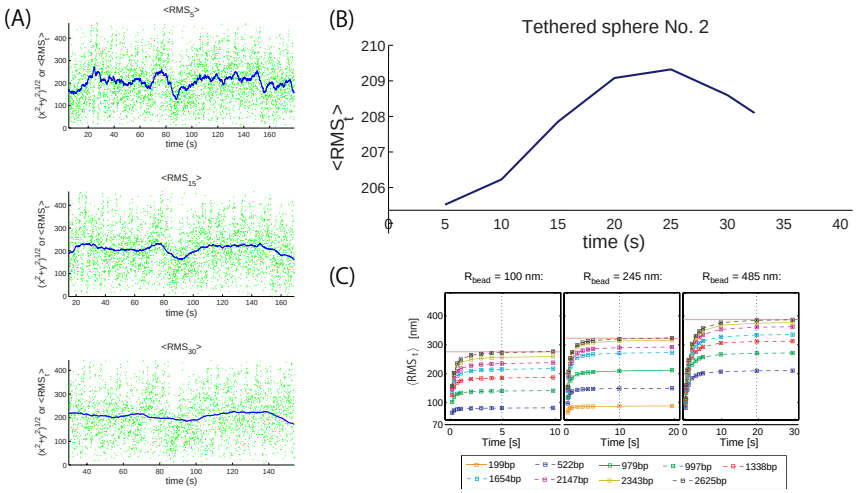

Figure 32: Experimental TPM approach in a system of ANF-tethers. (A) For the tethered particle No. 2, the function $(x^2+y^2)^{1/2}$ in light colored dots and the $< RMS_t >$ in dark line for $t = 5, 15, 30$ s are shown (top, middle and bottom, respectively). (B) $< RMS_t >$ function in the ANF system evaluated at different times is shown in comparison to the temporal behavior of the (C) $< RMS_t >$ function, but in a TPM experiment using DNA tethers. (Complete details of (C) in Han et al. 2008 [69]).

Application of the WT-DFA to the time series of TBM experiments

We applied the WT-DFA to the time series of 10 tethered spheres from a sample size of 100 tether events. Of the spheres selected, all presented a uniform spatial distribution symmetry as we inspected two-dimensional histograms of the positions of the particles (histograms not shown) and discarded those without an isotropic distribution. Multiple tethered particles can be identified by a position distribution asymmetry where an anisotropy of 10% is still safe to identify visually [16].

Moreover, to confirm a single or multiple tether, we computed the time-averaged sphere position in 4-second windows with the following expression,

$$RMS_t = \sqrt{< (x - \bar{x})^2 + (y - \bar{y})^2 >}\,, \tag{34}$$

where t is the time interval of the measured RMS motion. $\bar{x}$ and $\bar{y}$ are the averages of x and y, respectively, over time t.

This equation and a high-pass filter were used as a moving filter at every point of the microsphere trajectory producing a drift corrected time series.

Of the resulting drift corrected time series, the sphere excursion in the focal plane of the microscope and the time series of x and y displacements are shown in page 59. In each time series displayed, an

RMS_t with t = 4 s is presented as a visual indicator of the trend of the signal. For example, in Figure 33, the time series of tethered sphere No. 1 present a transient and non-specific binding event that was not appreciable in the sphere excursion plot or at the time during the experiment. We discarded spheres that presented such behavior.

Multiple tethering is common in DNA assays and occurred most of the times in our experiments. In contrast to the broad control in DNA assays, the TBM assays in this work had no control of the surface density of the diatom ANFs and the microspheres had no specific directed attachments to the diatom biofilms, thus, causing multiple tethering.

In page 59, next to the sphere excursions in the focal plane of the microscope and their corresponding time series, the double logarithmic plots for the determination of the scaling parameter H are shown. The algorithm of the WT-DFA in page 102 was applied to each of the drift corrected time series to analyze their correlation properties. Table 2 in page 63 displays the Hurst exponents and the particular correlations of each tethered sphere analyzed.

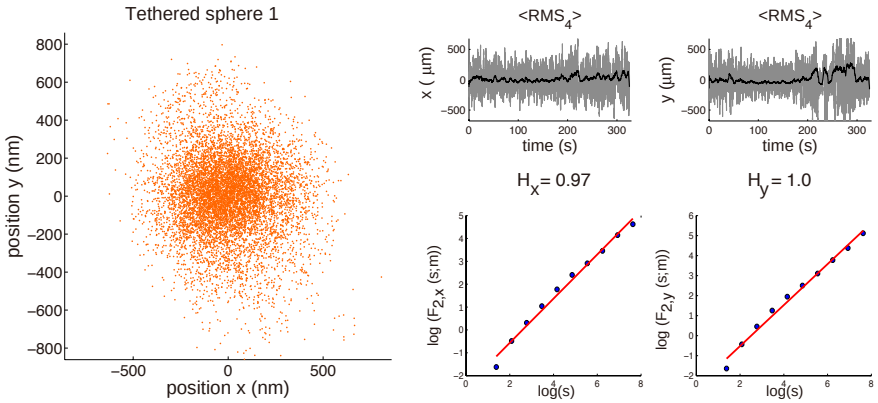

Figure 33: Sphere excursion in the focal plane of the microscope, time series of x and y displacements, and log-log plots of the fluctuation function F_2 of the two time series. The corresponding Hurst parameters are: $H_x = 0.97$, $H_y = 1.0$.

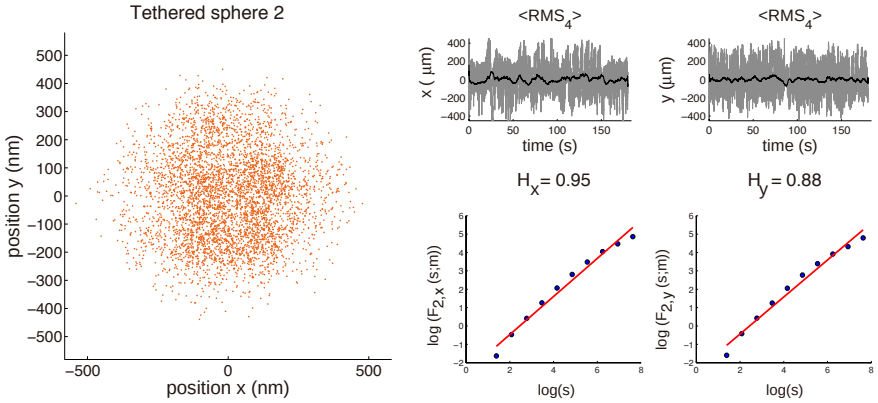

Figure 34: Same caption as in the previous figure, but different Hurst parameters: $H_x = 0.95$, $H_y = 0.88$.

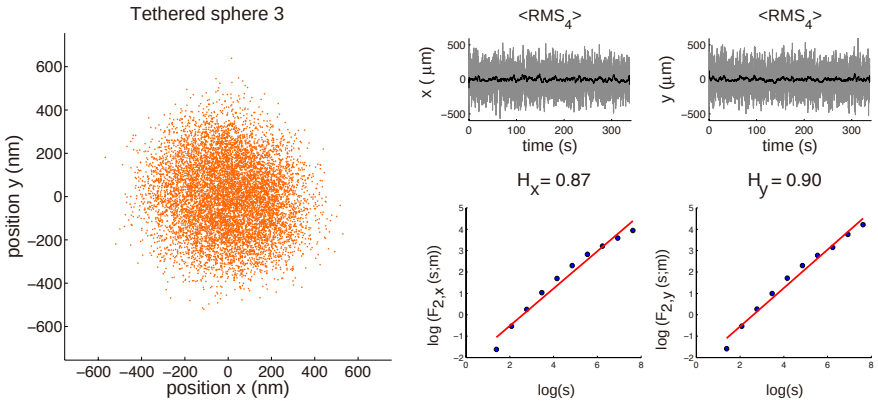

Figure 35: Same caption as in the previous figure, but different Hurst parameters: $H_x = 0.87$, $H_y = 0.90$.

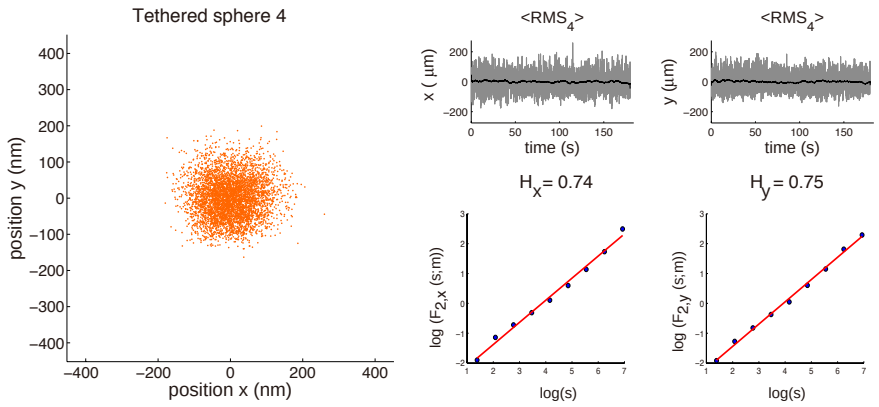

Figure 36: Sphere excursion in the focal plane of the microscope, time series of x and y displacements, and log-log plots of the fluctuation function F_2 of the two time series. The corresponding Hurst parameters are: $H_x = 0.74$, $H_y = 0.75$.

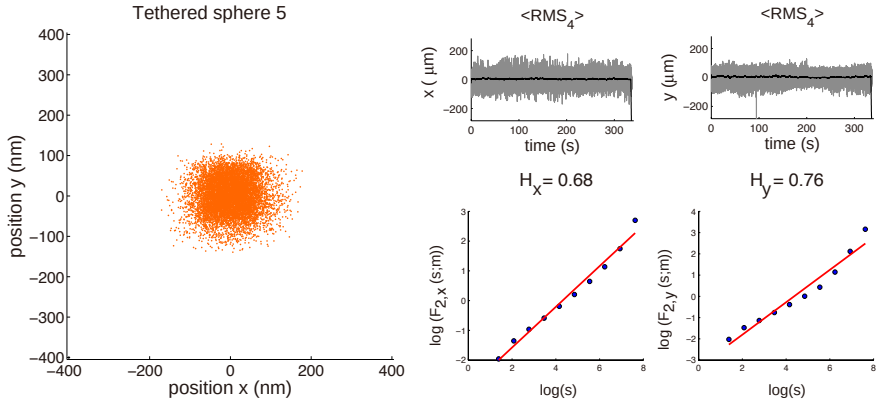

Figure 37: Same caption as in the previous figure, but different Hurst parameters: $H_x = 0.68$, $H_y = 0.76$.

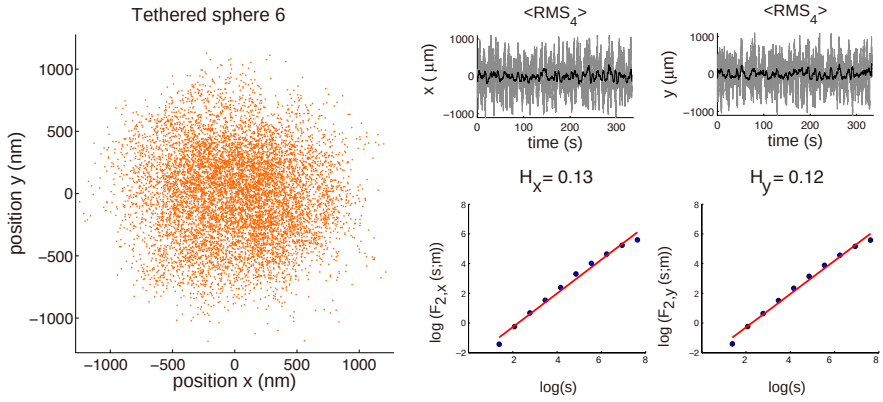

Figure 38: Same caption as in the previous figure, but different Hurst parameters: $H_x = 0.13$, $H_y = 0.12$.

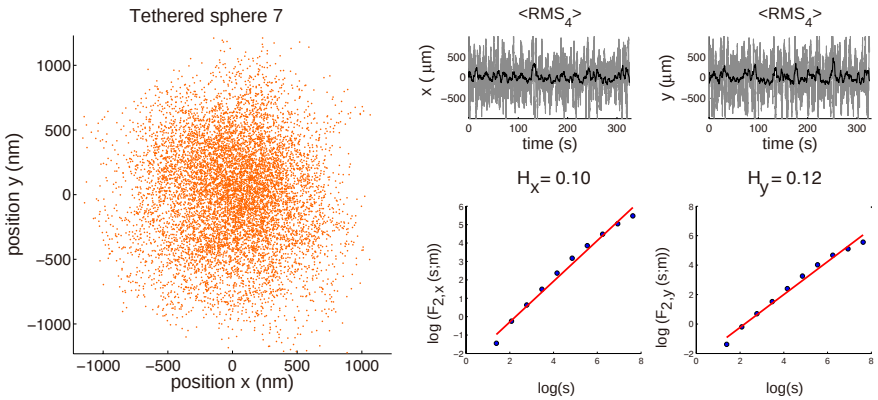

Figure 39: Sphere excursion in the focal plane of the microscope, time series of x and y displacements, and log-log plots of the fluctuation function F_2 of the two time series. The corresponding Hurst parameters are: $H_x = 0.10$, $H_y = 0.12$.

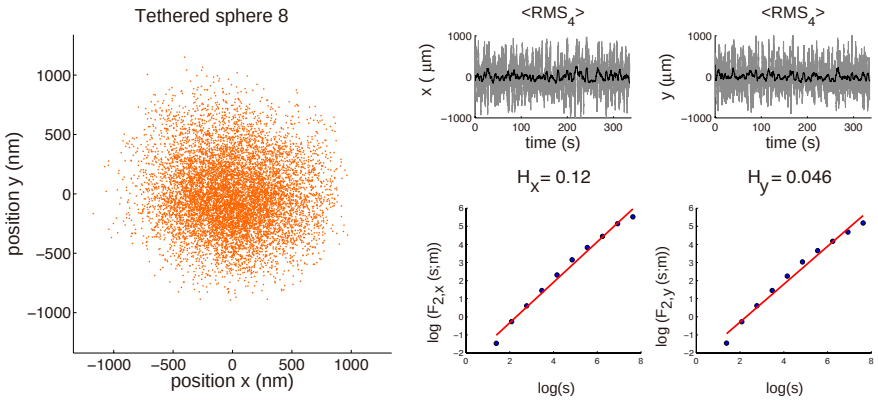

Figure 40: Same caption as in the previous figure, but different Hurst parameters: $H_x = 0.12$, $H_y = 0.046$.

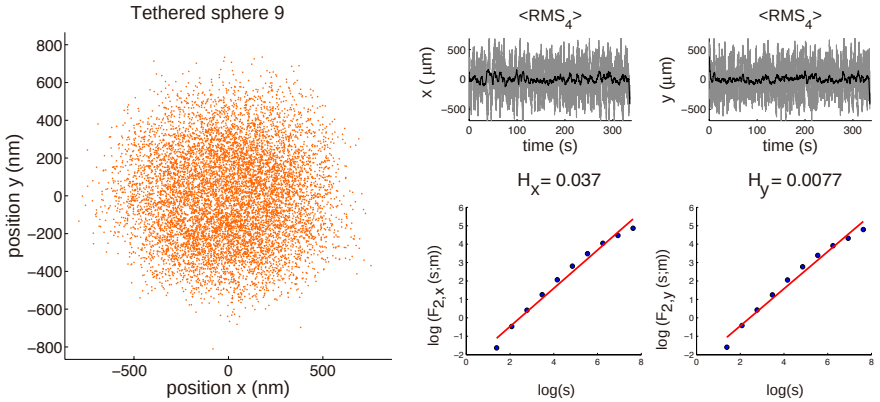

Figure 41: Sphere excursion in the focal plane of the microscope, time series of x and y displacements, and log-log plots of the fluctuation function F_2 of the two time series. The corresponding Hurst parameters are: $H_x = 0.037$, $H_y = 0.0077$.

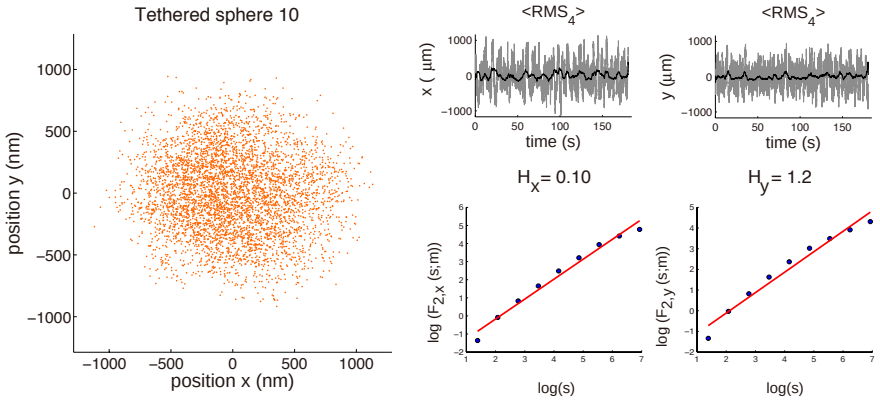

Figure 42: Same caption as in the previous figure, but different Hurst parameters: $H_x = 0.10$, $H_y = 1.2$.

HURST EXPONENTS: TBM

Tethered sphere	H_x	+/−	H_y	+/−
No. 1	0.99	+	1.0	+
No. 2	0.95	+	0.88	+
No. 3	0.87	+	0.90	+
No. 4	0.74	+	0.75	+
No. 5	0.68	+	0.76	+
No. 6	0.13	−	0.12	−
No. 7	0.10	−	0.12	−
No. 8	0.12	−	0.046	−
No. 9	0.037	−	0.0077	−
No. 10	0.10	−	1.2	+

Table 2: Hurst exponents of the time series of tethered spheres. Persistent series ($H > 0.5$) are indicated with a (+) sign, and antipersistent series ($H < 0.5$) are indicated with a (−) sign.

7

CELL MOTILITY: ANALYSIS AND RESULTS

In this chapter, we present an application of the Detrended Fluctuation Analysis method (DFA) by using a wavelet transform on the trajectories obtained experimentally from *Nitzschia* sp. diatoms. Moreover, a kinematic study over the same trajectories is presented.

7.1 STUDIES OF DIATOM TRAJECTORIES PREVIOUSLY REPORTED IN THE LITERATURE

Diatom trajectories have been studied since the 1960's [70] which according to their technique could be divided into three groups: (1) Studies that could only visualize diatom trajectories [135, 74, 96]. Such visualizing techniques are invasive. (See Figure 28 in p. 49). (2) Studies that incorporate object tracking and report kinematics [101, 129]. (3) Studies that involve fractal geometries and power laws from non-invasive observations of cell motion. Our work lies within this group which has not been reported in the diatom research literature.

7.2 APPLICATION OF THE WT-DFA ON *Nitzschia* SP. TRAJECTORIES

The motion of *Nitzschia* sp. cells was obtained by a post process of video microscopy and an in-house computer tracking routine. One hundred and forty one single diatoms were captured in video to which the WT-DFA analysis was performed.

Videos captured digitally (26 fps) from the cell motility assay went under a basic digital image processing of cropping, color inversion and file format conversion. The video frame format conversion and the tracking routine are fully detailed in Appendix B, p. 97.

Precision of the diatom position measurement

To determine the precision of the measured positions by the tracking routine, we use videos of cells at rest and assigned one diatoms as the reference position to which we compared the position of other immobile diatoms relative to the reference.

In Figure 43, the computed tracking positions of the reference diatom No. 1, diatom No. 2 and their corresponding time series (left and right columns, respectively) are shown. Lastly, their position difference is also shown. The standard deviation of the position difference is 0.0850 μm and 0.0754 μm for the x and y coordinates, respectively,

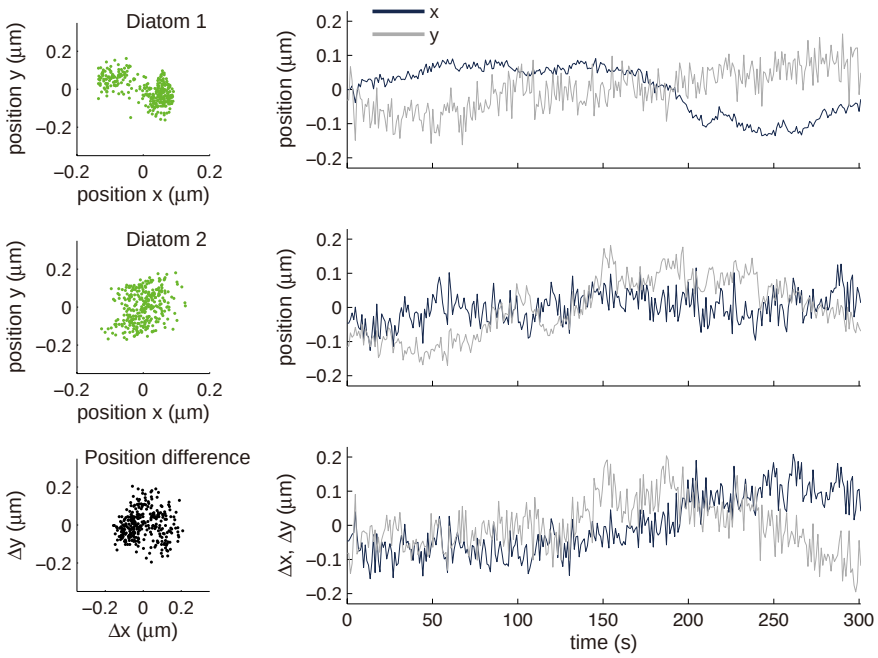

Figure 43: Precision measurement of individual diatoms. Each diatom is about 30 μm in length.

suggesting a precision of the measurements of microsphere positions of 0.5 – 1.0 μm or better can be obtained with the experimental equipment and computer tracking routine.

In the times series of diatom No. 1 (Figure 43), there was a slight focusing-and-defocusing effect due to the microscope at 200 seconds and it is observed as a steep decline in the measured position of the x coordinate. The reason of this behavior is due to fluctuations in the color intensities from one video frame to the next, causing the tracked coordinate to oscillate or eventually lose its intended spot. The reported measurements in this section are susceptible to the tracking error described.

In pp. 67-73 we present the WT-DFA applied to 20 *Nitzschia* sp. trajectories to analyze the correlation properties of their drift corrected time series using the algorithm described in Appendix B p. 97. In addition, in Table 3 (p. 74) the Hurst exponents and the particular correlations of each tethered sphere analyzed are shown. The rest of the trajectories are neatly presented in Appendix C p. 105.

Trajectories were recorded for 5 min. and only a few of them lasted less in the case of proximity to other diatoms which challenged the tracking routine.

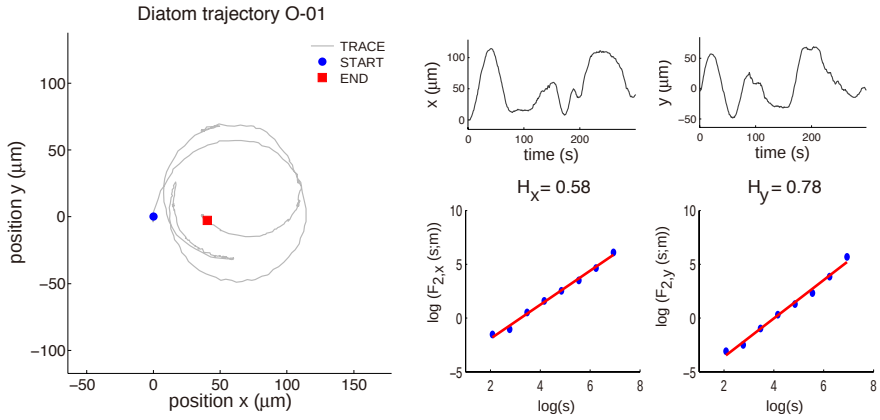

Figure 44: Diatom trajectory, x and y time series and log-log plots. Hurst exponent $H_x = 0.58$, $H_y = 0.78$.

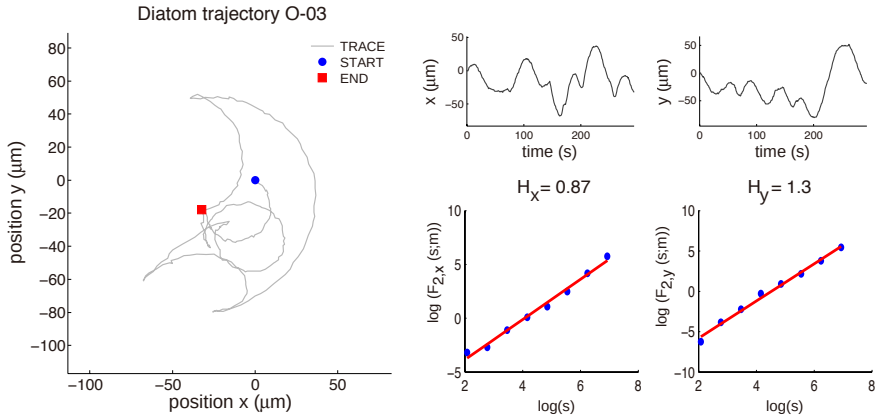

Figure 45: Diatom trajectory, x and y time series and log-log plots. Hurst exponent $H_x = 0.87$, $H_y = 1.3$.

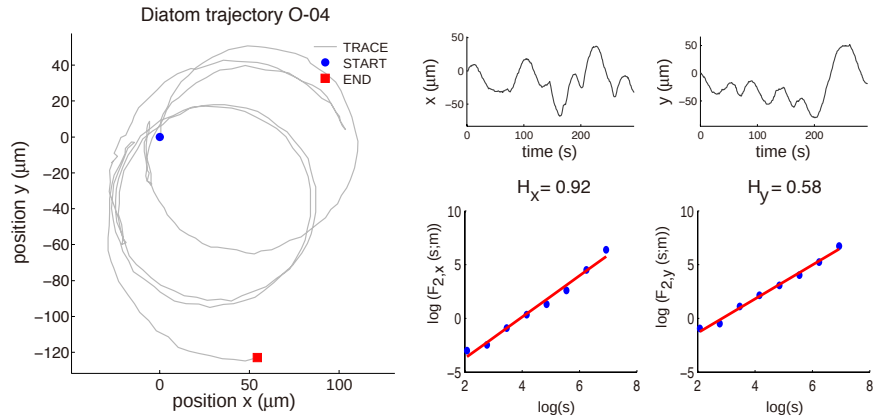

Figure 46: Diatom trajectory, x and y time series and log-log plots. Hurst exponent $H_x = 0.92$, $H_y = 0.58$.

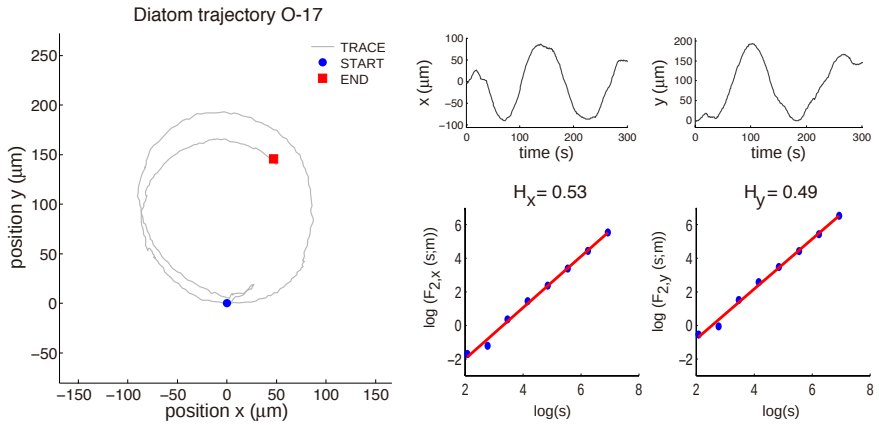

Figure 47: Diatom trajectory, x and y time series and log-log plots. Hurst exponent $H_x = 0.53$, $H_y = 0.49$.

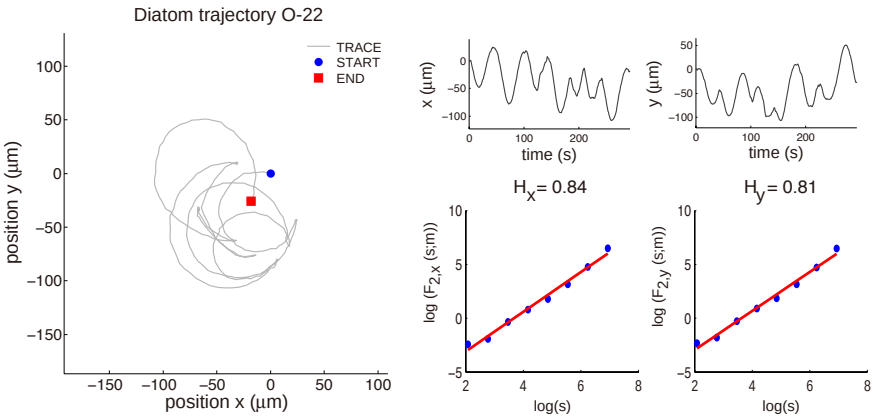

Figure 48: Diatom trajectory, x and y time series and log-log plots. Hurst exponent $H_x = 0.84$, $H_y = 0.81$.

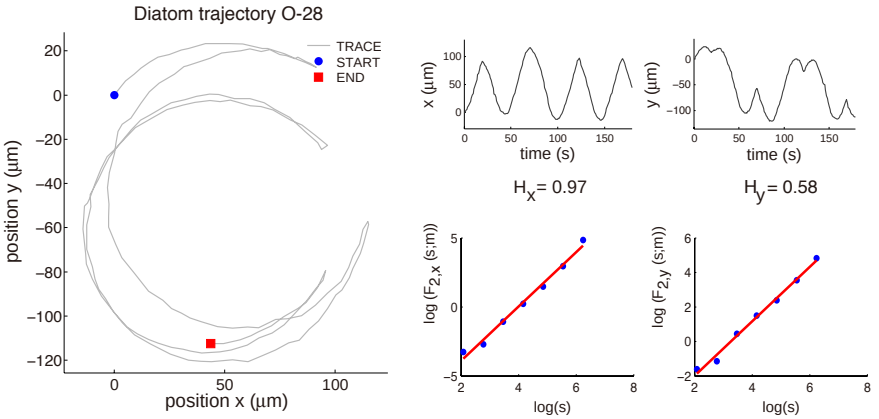

Figure 49: Diatom trajectory, x and y time series and log-log plots. Hurst exponent $H_x = 0.97$, $H_y = 0.58$.

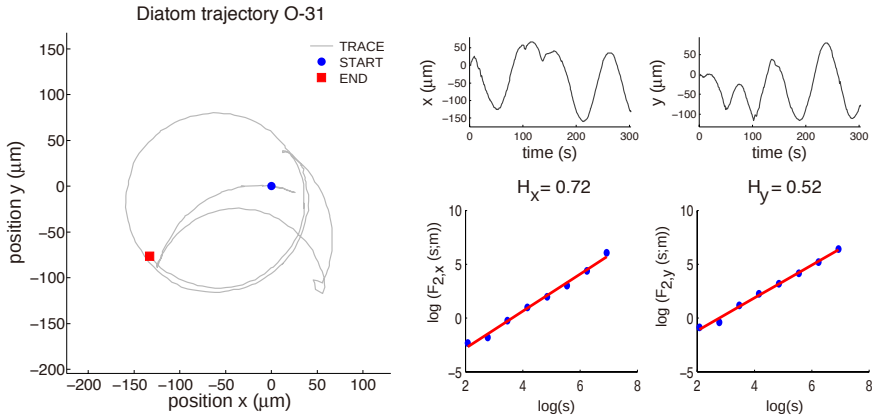

Figure 50: Diatom trajectory, x and y time series and log-log plots. Hurst exponent H_x = 0.72, H_y = 0.52 .

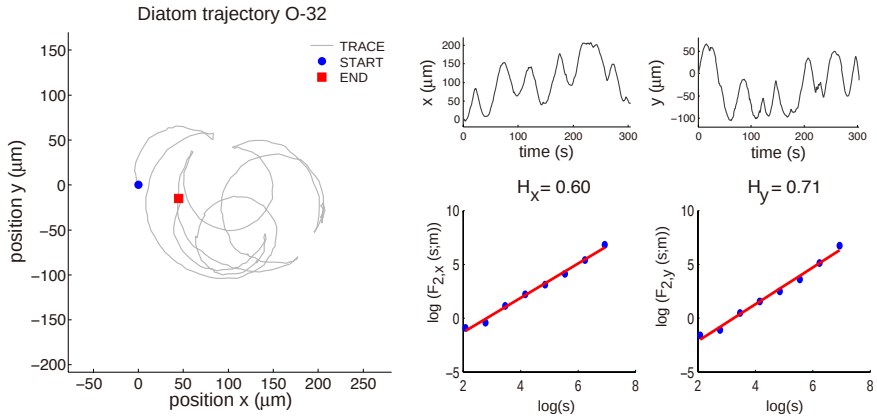

Figure 51: Diatom trajectory, x and y time series and log-log plots. Hurst exponent H_x = 0.60, H_y = 0.71 .

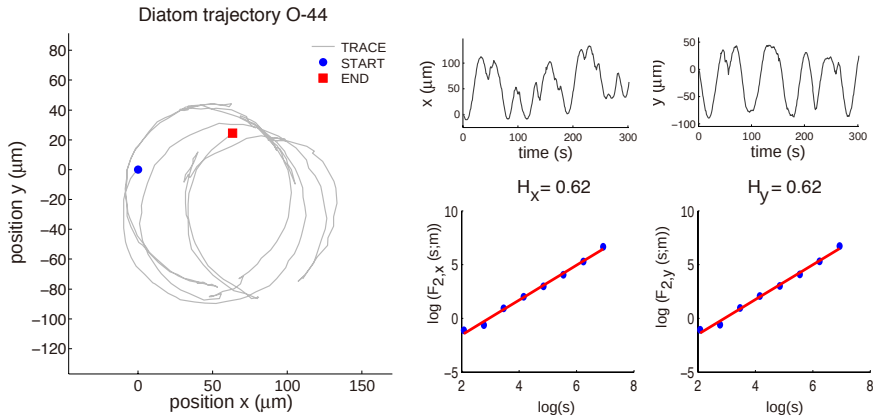

Figure 52: Diatom trajectory, x and y time series and log-log plots. Hurst exponent H_x = 0.62, H_y = 0.62 .

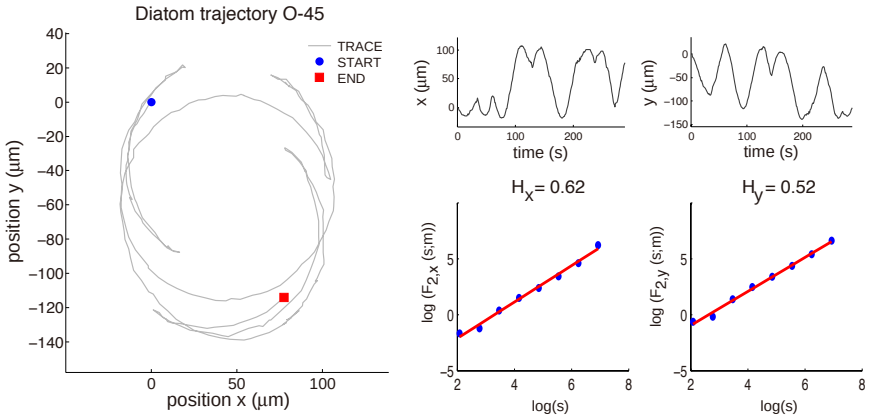

Figure 53: Diatom trajectory, x and y time series and log-log plots. Hurst exponent $H_x = 0.62$, $H_y = 0.52$.

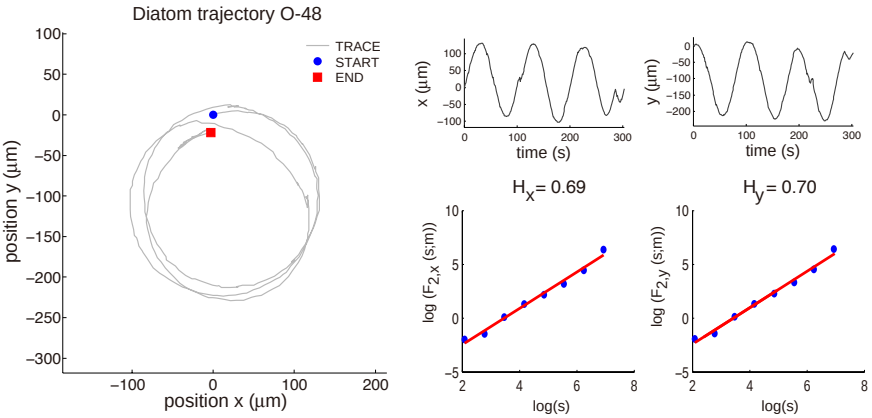

Figure 54: Diatom trajectory, x and y time series and log-log plots. Hurst exponent $H_x = 0.69$, $H_y = 0.70$.

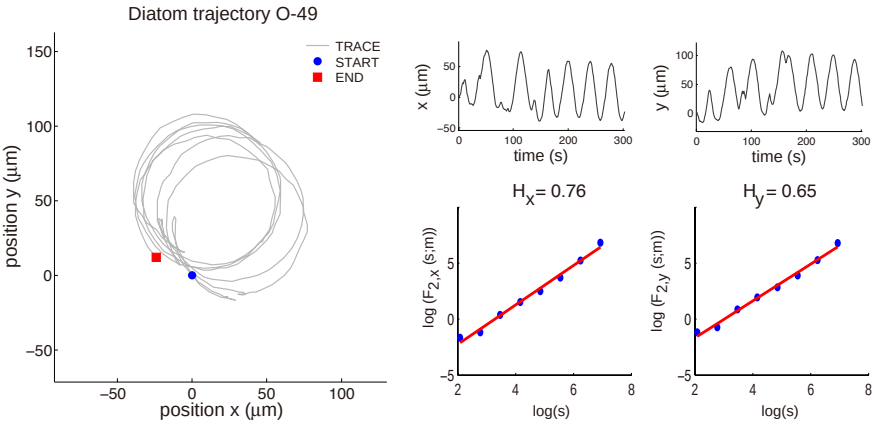

Figure 55: Diatom trajectory, x and y time series and log-log plots. Hurst exponent $H_x = 0.76$, $H_y = 0.65$.

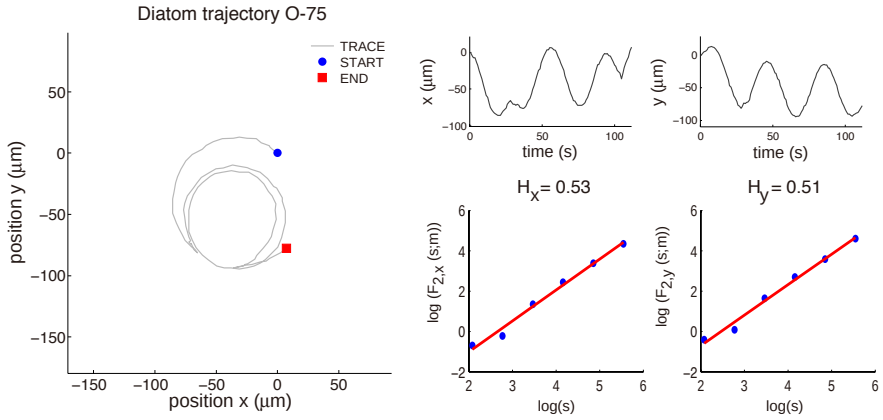

Figure 56: Diatom trajectory, x and y time series and log-log plots. Hurst exponent H_x = 0.53, H_y = 0.51 .

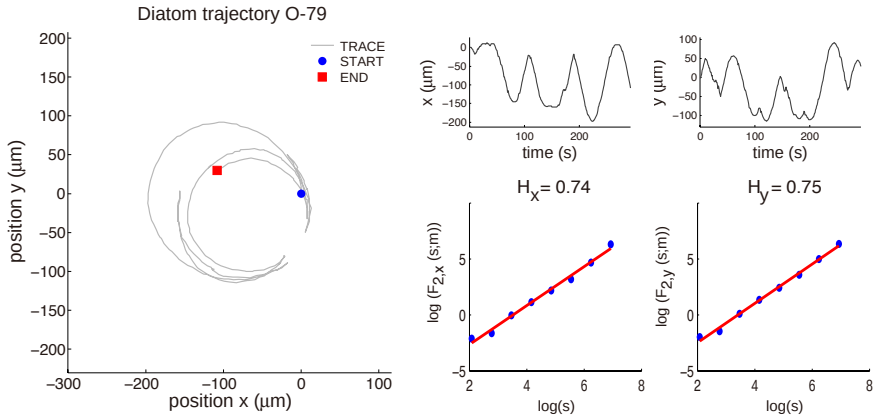

Figure 57: Diatom trajectory, x and y time series and log-log plots. Hurst exponent H_x = 0.74, H_y = 0.75 .

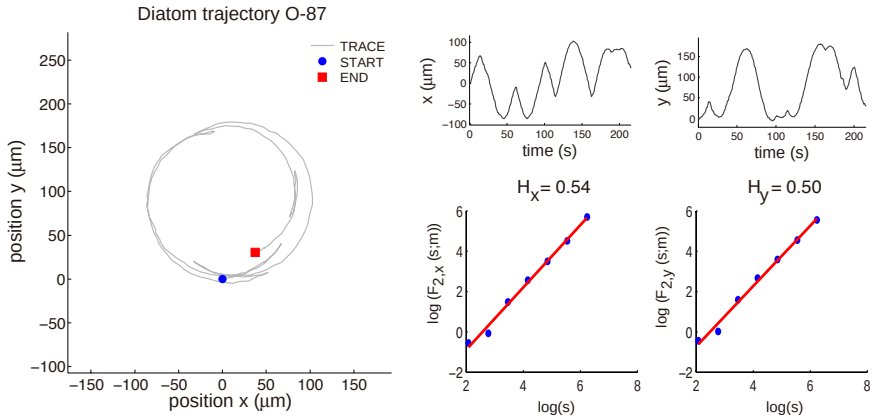

Figure 58: Diatom trajectory, x and y time series and log-log plots. Hurst exponent H_x = 0.54, H_y = 0.50 .

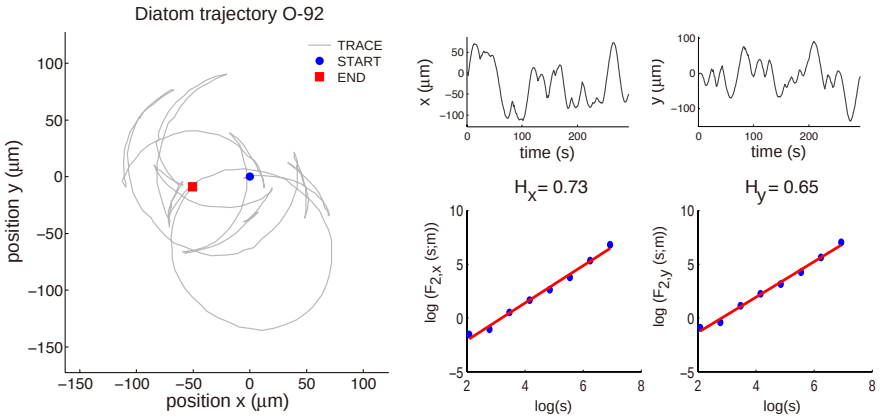

Figure 59: Diatom trajectory, x and y time series and log-log plots. Hurst exponent $H_x = 0.73$, $H_y = 0.65$.

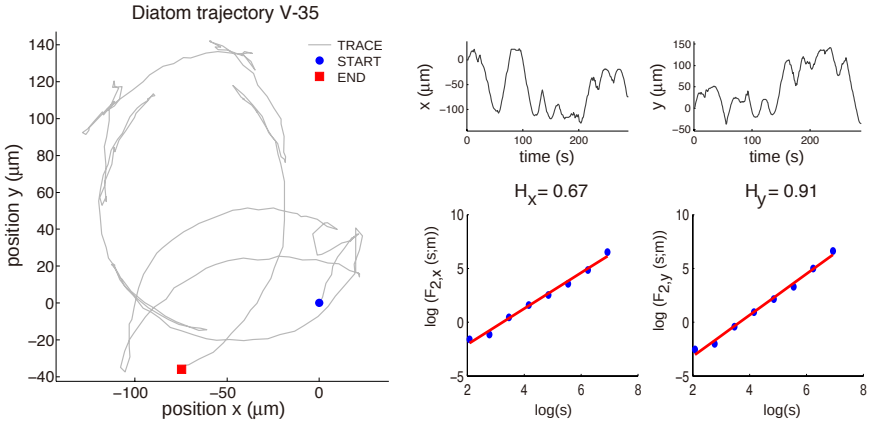

Figure 60: Diatom trajectory, x and y time series and log-log plots. Hurst exponent $H_x = 0.67$, $H_y = 0.91$.

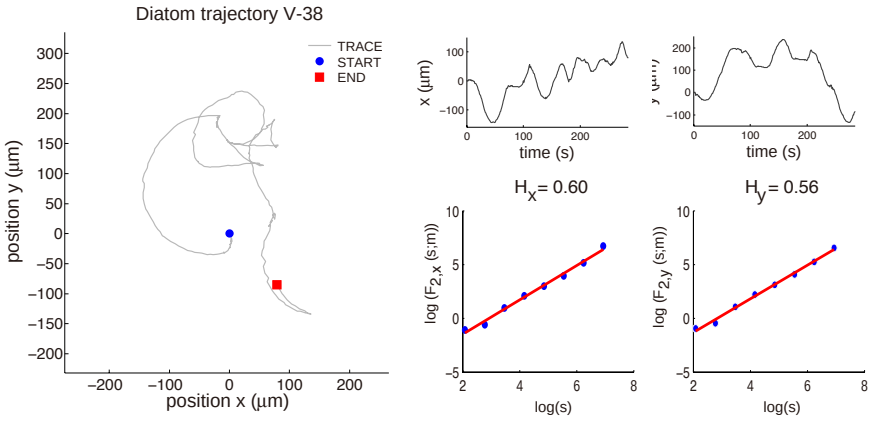

Figure 61: Diatom trajectory, x and y time series and log-log plots. Hurst exponent $H_x = 0.60$, $H_y = 0.56$.

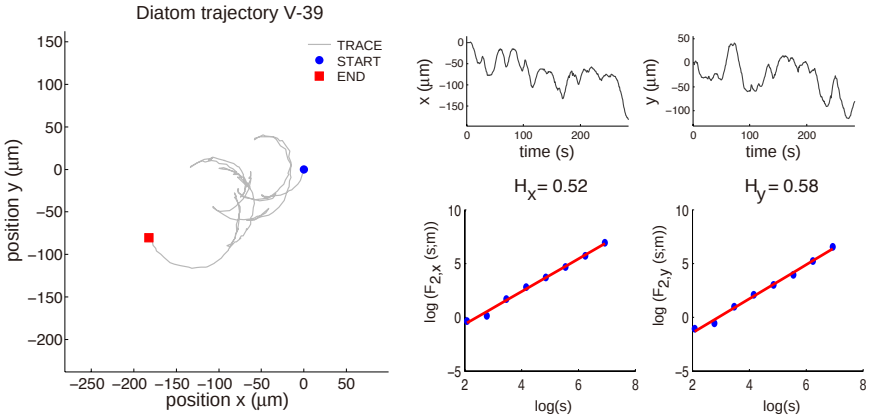

Figure 62: Diatom trajectory, x and y time series and log-log plots. Hurst exponent H_x = 0.52, H_y = 0.58 .

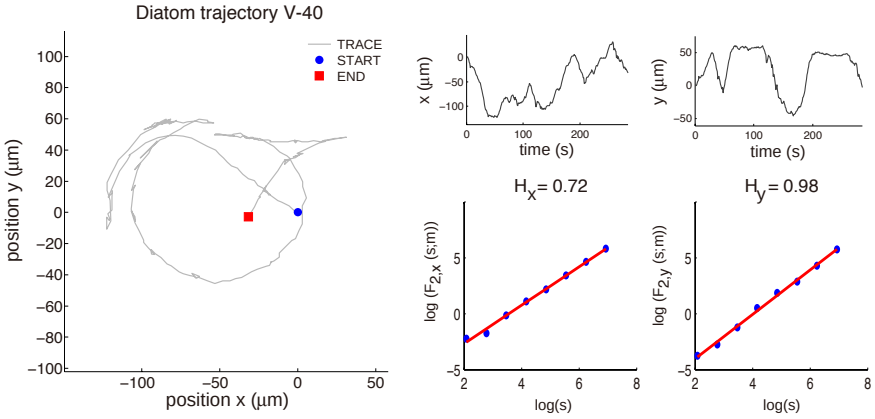

Figure 63: Diatom trajectory, x and y time series and log-log plots. Hurst exponent H_x = 0.72, H_y = 0.98 .

HURST EXPONENTS: TRAJECTORIES

Diatom code name	H_x	+/−	H_y	+/−
O-01	0.58	+	0.78	+
O-03	0.87	+	1.3	+
O-04	0.92	+	0.58	+
O-17	0.53	+	0.49	−
O-22	0.84	+	0.71	+
O-28	0.97	+	0.58	+
O-31	0.72	+	0.52	+
O-32	0.60	+	0.71	+
O-44	0.73	+	0.65	+
O-45	0.62	+	0.52	+
O-48	0.69	+	0.70	+
O-49	0.76	+	0.65	+
O-75	0.53	+	0.51	+
O-79	0.74	+	0.75	+
O-87	0.54	+	0.50	+
O-92	0.73	+	0.65	+
V-35	0.67	+	0.91	+
V-38	0.60	+	0.56	+
V-39	0.52	+	0.58	+
V-40	0.72	+	0.98	+

Table 3: Hurst exponents of the time series from diatom trajectories. Persistent series ($H > 0.5$) are indicated with a (+) sign, and antipersistent series ($H < 0.5$) are indicated with a (−) sign.

7.3 KINEMATICS OF THE *Nitzschia* SP. DIATOM TRAJECTORIES

This section contains measurements of the kinematics of single *Nitzschia* sp. diatom trajectories.

The trajectories were divided into two classes according to their radius of curvature described along various segments of the full trajectory. The first class of circular trajectories (Figure 64) shown to be smooth and therefore we assigned to them the letter O. The radius of curvature in the O-trajectories was $xx \pm 1.0$ µm. A second class of trajectories (Figure 64) was not smooth as the previous class, and we assigned to them the letter V. The radius of curvature in the V-trajectories was $xx \pm 1.0$ µm.

The rest of the O and V trajectories are in pp. 106-138 and pp. 138-153, respectively.

Total displacement of diatoms

The maximum distance covered by a cell, referred in this document as the maximum diatom total displacement, was 3473.6 ± 1.0 µm. The average was 746.3 ± 1.0 µm

Instantaneous speed of diatoms

The mean speed was 5.678 ± 1.005 µm/s, and the maximum speed was 20.30 ± 1.041 µm/s. The minimum speed was $0 + 0.236$ µm/s meaning that the diatom had stopped for at least one instant during the full recorded trajectory. For the O trajectories, 16 % of the diatoms stopped at least for one instant, whereas for the V trajectories 39 % of the diatoms stopped at least once.

Table 4 shows the kinematic parameters for the two classes of trajectories. In Tables 5, 6, 7, 8 and 9 the same parameters are shown for each trajectory.

Histograms for all the trajectories and for classes O and V are also provided in Figure 68, Figure 69 and Figure 70 respectively.

In Figure 71, histograms for the total displacement of all the trajectories and for classes O and V are shown.

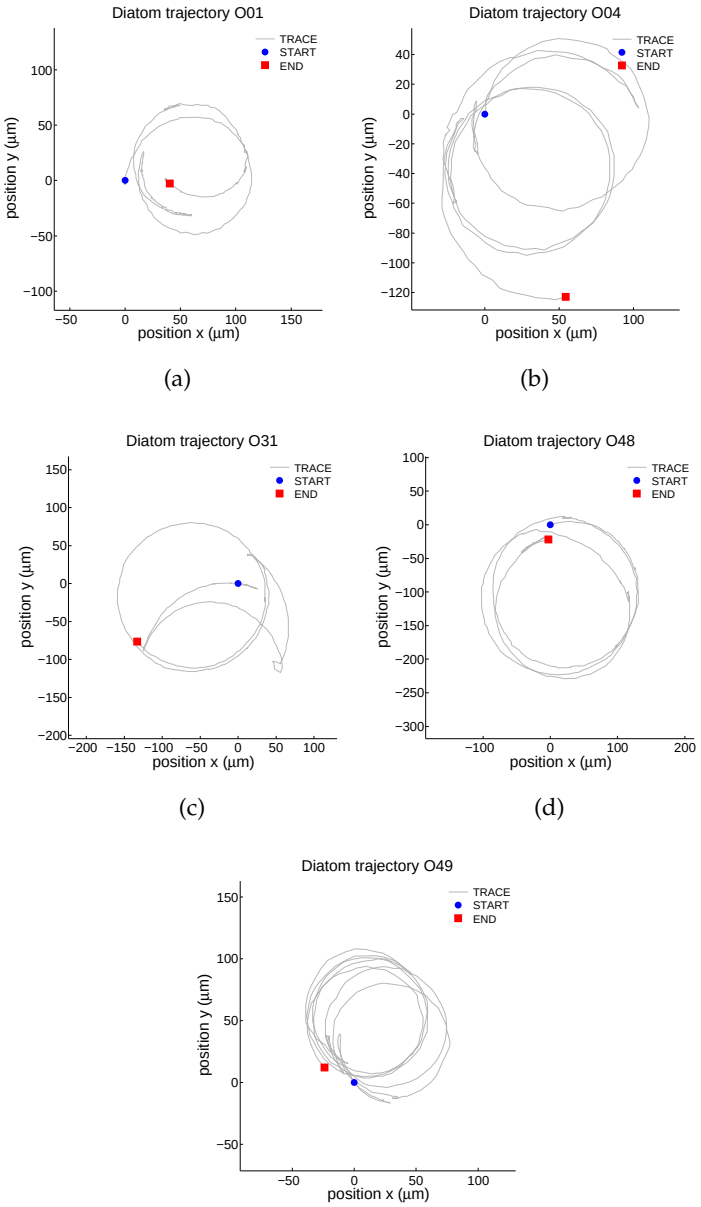

Figure 64: Representative *Nitzschia* sp. trajectories of the class O. This class is characterized by a radius of curvature of xx ± xx SE µm.

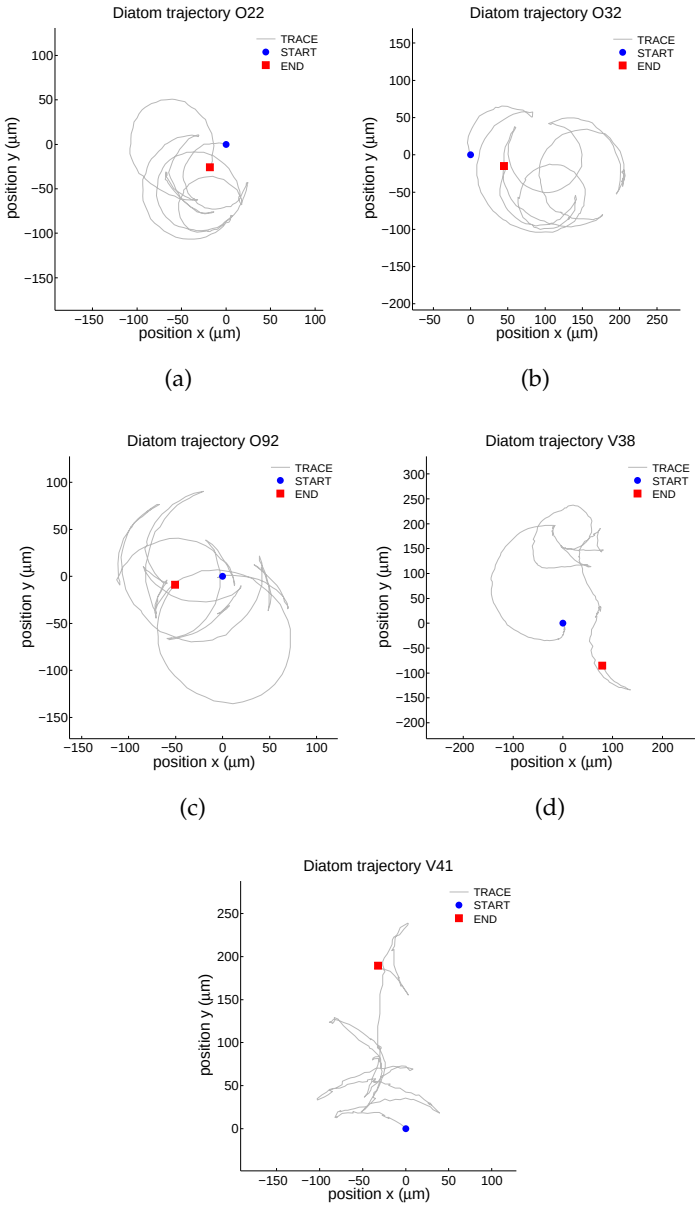

Figure 65: Representative *Nitzschia* sp. trajectories of the class V. This class is characterized by a radius of curvature of xx ± xx SE µm.

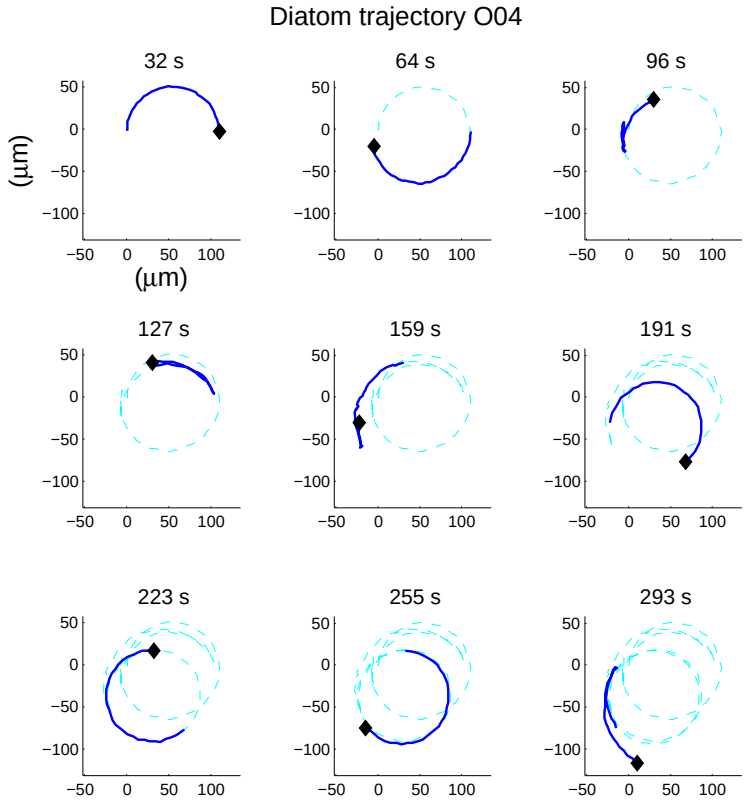

Figure 66: Representative time lapse trajectory

K				
Class	Mean speed ± σ (µm/s)	Max speed ± σ (µm/s)	Min speed ± σ (µm/s)	Displacement ± σ µm
O	5.678 ± 1.005	20.30 ± 1.041	0 + 0.236	3474 ± 1.0
V	3.796 ± 1.002	17.75 ± 1.035	0 + 0.236	2854 ± 1.0

Table 4: Kinematic parameters for 141 different diatoms classified by the features of their trajectories as smooth and circular (O), or as non-smooth and chaotic (V). See text for details.

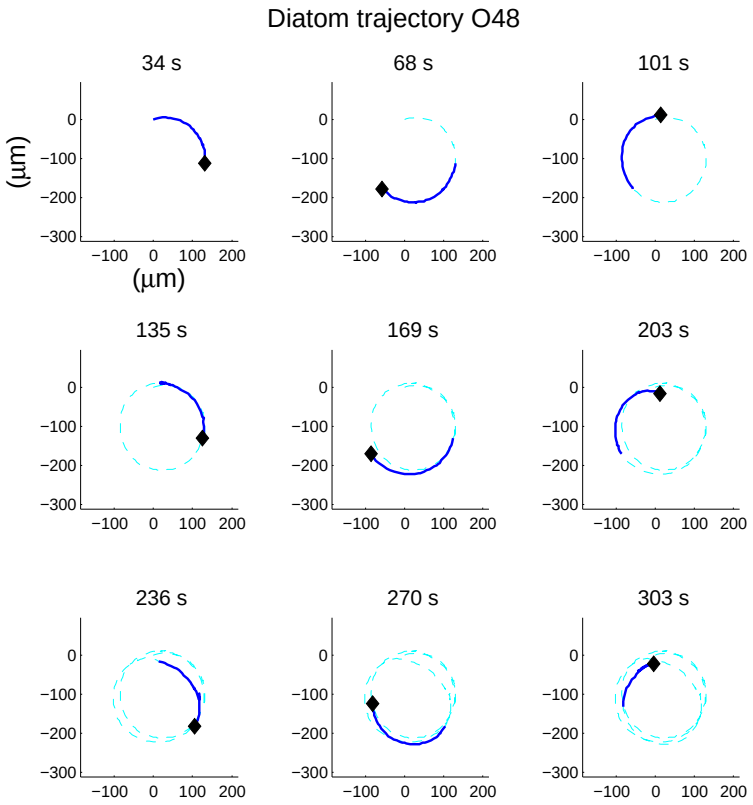

Figure 67: Representative time lapse trajectory

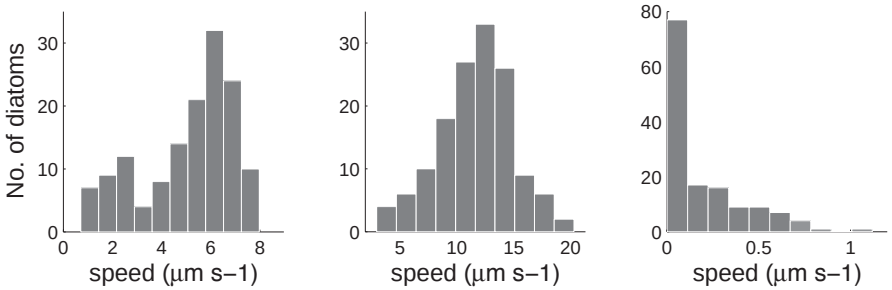

(a) Mean, maximum, and minimum speed distributions.

Figure 68: Speed distributions for 141 diatoms.

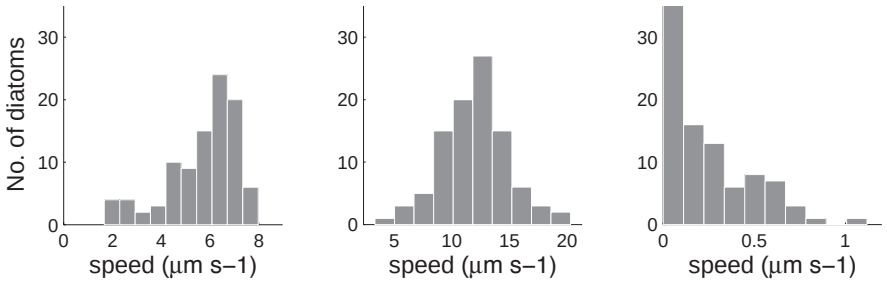

(a) Mean, maximum, and minimum speed distributions.

Figure 69: Speed distributions for 97 diatoms class O.

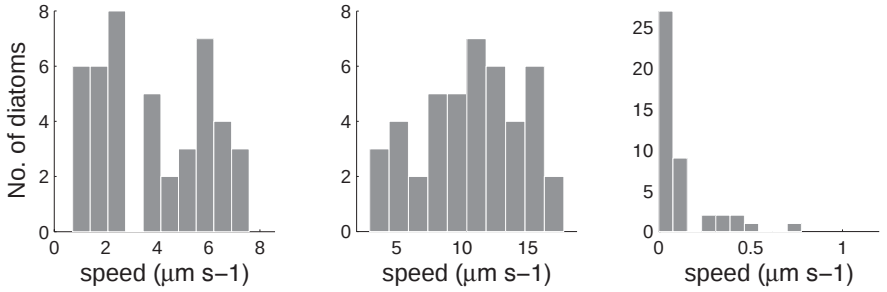

(a) Mean, maximum, and minimum speed distributions.

Figure 70: Speed distributions for 44 diatoms class V.

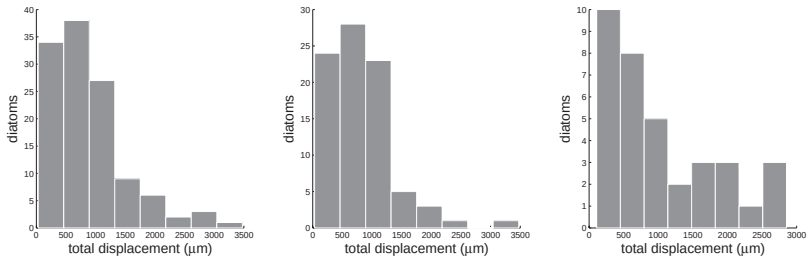

(a) All diatoms (b) Class O (c) Class V

Figure 71: Long caption. (a) Distribution of the displacement of 141 diatoms. Distribution of the displacement of 97 diatoms class O. Distribution of the displacement of 44 diatoms class V.

KO1					
Diatom	Displacement (μm)	Duration (s)	Mean speed (μm/s)	Max speed (μm/s)	Min speed (μm/s)
O1	400.6	299.0	3.028	7.362	0.155
O2	1003	300.0	7.034	11.84	0.519
O3	355.4	293.3	2.685	6.503	0.0223
O4	261.1	293.3	5.941	9.640	0.627
O5	526.7	287.5	6.196	9.358	0.367
O6	2221	287.5	5.163	11.41	0.541
O7	982.0	287.5	5.867	9.267	0.198
O8	532.8	184.6	4.918	9.591	0.316
O9	593.4	284.6	5.076	10.59	0.317
O10	469.2	298.1	6.493	9.615	0.29
O11	716.4	298.1	4.204	12.70	0.214
O12	569.3	298.1	4.684	7.830	0.104
O13	1792	288.5	6.312	11.05	0.322
O14	1045	288.5	5.540	10.03	0.083
O15	836.8	294.2	4.362	11.88	0.257
O16	298.5	301.0	6.158	10.39	0.359
O17	512.0	301.0	3.435	8.288	0.0412
O18	1593	301.0	5.720	9.534	0.163
O19	670.5	301.0	1.664	5.822	0.0181
O20	1662	125.0	5.995	9.431	0.717
O21	732.5	125.0	4.510	8.860	0.402
O22	619.4	293.3	5.140	9.988	0.373
O23	683.1	293.3	5.760	12.17	0.366
O24	1142	293.3	2.430	6.221	0.176
O25	361.9	293.3	6.792	15.19	0.575
O26	391.5	297.1	7.317	16.80	0.0518
O27	988.6	283.6	5.790	13.59	0.115
O28	653.4	178.8	6.355	11.65	0.583
O29	458.9	178.8	6.654	12.84	0.582
O30	1086	283.6	6.351	14.16	0.178
O31	625.6	302.9	5.433	13.30	0.149
O32	1047	303.9	6.749	12.94	0.13
O33	1198	303.9	6.517	11.72	0.0312

Table 5: Kinematic parameters O 1 – 33.

KO2					
Diatom	Displacement (μm)	Duration (s)	Mean speed (μm/s)	Max speed (μm/s)	Min speed (μm/s)
O34	1179	303.9	6.266	14.35	0.255
O35	1641	200.0	5.804	13.46	0.611
O36	424.8	142.3	6.147	13.21	0.0754
O37	864.1	275.0	5.506	11.93	0.0207
O38	440.7	241.3	5.620	11.73	0.0198
O39	415.7	301.9	5.861	12.64	0
O40	288.4	283.6	2.681	9.359	0.0115
O41	1221	283.6	6.914	16.99	0.622
O42	644.6	228.8	6.409	12.65	0
O43	3474	302.9	5.194	14.03	0.147
O44	543.9	301.9	6.645	17.84	0.103
O45	900.8	288.5	5.012	9.798	0.236
O46	696.3	288.5	3.696	10.51	0.0365
O47	661.1	236.5	7.507	13.56	0.703
O48	822.8	302.9	7.463	16.85	0.32
O49	357.5	301.9	6.822	12.57	0.37
O50	964.8	301.9	6.500	12.82	0.529
O51	909.7	301.9	6.759	13.46	0.204
O52	420.3	301.9	5.199	14.18	0
O53	208.2	209.6	2.009	7.948	0.0927
O54	198.0	126.9	6.491	13.42	0.2
O55	33.06	126.9	6.067	13.47	0.583
O56	74.73	127.9	4.386	11.91	0.466
O57	302.0	126.0	6.145	9.996	0.785
O58	1577	292.3	2.394	9.433	0.0104
O59	1786	292.3	6.777	12.11	1.12
O60	780.5	294.2	4.572	10.38	0.0461
O61	218.6	284.6	2.169	7.012	0.0333
O62	1368	271.1	6.343	12.05	0.236
O63	1071	283.6	6.571	12.03	0.506
O64	339.8	140.4	1.952	3.332	0.23
O65	1285	126.9	4.614	11.21	0
O66	873.4	298.1	4.496	10.53	0

Table 6: Kinematic parameters O 34 – 66.

KO3					
Diatom	Displacement (μm)	Duration (s)	Mean speed (μm/s)	Max speed (μm/s)	Min speed (μm/s)
O67	310.7	282.7	7.269	14.03	0
O68	317.3	282.7	6.328	10.98	0.259
O69	1349	129.8	6.248	12.09	0.0722
O70	107.3	301.9	6.806	13.72	0.0518
O71	32.00	301.9	6.301	11.41	0.0312
O72	1226	301.9	6.594	15.44	0.0104
O73	272.6	160.6	5.686	16.50	0.0268
O74	1724	289.4	4.196	11.33	0
O75	454.7	111.5	6.164	10.12	0
O76	181.1	163.5	5.766	10.77	0.121
O77	706.0	291.4	5.126	11.43	0
O78	431.4	293.3	4.392	17.05	0
O79	854.5	293.3	6.489	16.05	0
O80	1087	298.1	6.940	19.41	0.205
O81	860.8	292.3	3.873	12.25	0
O82	466.8	296.1	6.826	11.34	0.493
O83	484.2	292.3	7.974	14.45	0.044
O84	420.7	190.4	6.211	11.81	0.322
O85	1850	294.2	7.179	13.54	0.249
O86	334.6	299.0	7.542	13.76	0.503
O87	486.3	215.4	7.288	13.46	0.466
O88	799.3	297.1	7.122	13.33	0.114
O89	1004	301.0	7.208	20.30	0.0425
O90	936.1	300.0	6.782	11.75	0.0474
O91	347.5	300.0	6.757	12.52	0.68
O92	367.3	292.3	7.811	13.62	0
O93	340.1	125.0	7.461	15.06	0
O94	314.4	271.1	7.018	14.04	0.0104
O95	234.6	301.9	3.709	11.94	0
O96	1309	303.9	6.986	15.86	0.197
O97	582.1	292.3	5.457	11.47	0

Table 7: Kinematic parameters O 67 – 97.

KV1					
Diatom	Displacement (μm)	Duration (s)	Mean speed (μm/s)	Max speed (μm/s)	Min speed (μm/s)
V1	528.2	284.6	2.611	6.982	0.106
V2	1941	299.0	2.401	8.634	0.0938
V3	220.4	294.2	0.9444	5.745	0.138
V4	504.1	294.2	1.506	5.671	0.0969
V5	1073	295.2	4.734	8.995	0.0134
V6	920.6	293.3	2.528	11.10	0
V7	239.6	283.6	1.904	7.101	0.0515
V8	708.7	180.8	3.819	8.073	0
V9	1428	302.9	6.559	15.72	0.434
V10	2854	303.9	5.247	13.26	0.056
V11	888.8	89.42	6.227	10.44	0.319
V12	188.1	301.0	1.701	16.05	0
V13	1549	291.4	5.674	16.90	0
V14	57.70	126.9	0.709	2.954	0
V15	205.5	127.9	2.039	11.88	0.00722
V16	181.0	126.0	2.344	9.224	0.0912
V17	61.81	126.0	1.080	3.142	0.103
V18	371.0	292.3	0.9344	2.988	0.0908
V19	99.09	121.2	7.197	12.11	0.241
V20	395.5	285.6	1.409	7.855	0.0826
V21	1622	275.0	5.555	9.959	0.374
V22	1510	286.5	6.481	11.27	0.29

Table 8: Kinematic parameters V 1 – 22.

KV2					
Diatom	Displacement (μm)	Duration (s)	Mean speed (μm/s)	Max speed (μm/s)	Min speed (μm/s)
V23	178.2	284.6	1.131	5.582	0
V24	2705	283.6	5.795	13.50	0.0227
V25	695.9	237.5	2.540	8.512	0.0477
V26	307.6	48.08	5.697	9.499	0.487
V27	468.2	298.1	2.121	10.76	0
V28	150.2	114.4	4.067	10.39	0.0392
V29	139.4	185.6	1.303	5.497	0
V30	1941	226.9	3.509	13.06	0
V31	342.3	293.3	1.646	8.110	0
V32	663.2	290.4	2.197	8.903	0.0112
V33	2478	212.5	6.153	14.70	0
V34	110.2	257.7	2.766	12.07	0
V35	997.2	287.5	5.651	13.59	0.0677
V36	2010	208.7	4.735	15.16	0
V37	489.9	57.69	7.586	11.41	0.777
V38	593.4	283.6	6.213	14.91	0
V39	868.4	283.6	4.974	14.93	0.111
V40	634.8	283.6	3.833	17.75	0
V41	851.7	283.6	5.025	13.22	0.0489
V42	115.7	248.1	3.571	15.00	0
V43	1188	282.7	7.106	14.08	0
V44	721.6	160.6	5.812	10.70	0.411

Table 9: Kinematic parameters 23 – 44.

8

CONCLUSIONS AND PERSPECTIVES

In this thesis, the results of two types of experiments of the single cell level for the case of *Nitzschia* sp. diatom. are reported. Both of them are performed using optical microscopy.

One refers to the tethered particle motion type of experiments similar to the well-stablished experiments with DNA. The difference is that the tethered material is made of the adhesive nanofibers (ANFs) from diatom biofilms.

In case of DNA this experiments report conformational changes in the DNA molecule, but for the *Nitzschia* sp. ANFs this was not possible in the conditions for our experiments. However, we determined the Hurst parameter of this kind of motion imposed to the microspheres attached to these diatom ANFs.

We obtained both persistent and antipersistent fractional Brownian motions. The Hurst exponent of the antipersistent motion is very low (close to zero) and according to the literature[1] the corresponding time series are not relevant. Thus, we claim that the tethered Brownian motion with ANFs is a fractional Brownian motion of persistent type because we obtained more confident time series in the latter case. To the best of our knowledge, results of this type have not been reported in the literature.

In the second experiment, the live diatom trajectories recorded by video microscopy have been analyzed by means of the Detrended Fluctuation Analysis (DFA) which has been optimized by using the discrete wavelet transform. We examined only the time series originated from individual diatoms and the cases of intersecting trajectories between diatoms were scarce.

The Hurst parameters determined in this way indicate a fractional Brownian motion of persistent type. This, in some way, is an expected result if one takes into account that this microscopic live motion is in general sensitive to external light sources. As a matter of fact, the majority of the trajectories recorded in the central spot of the field of view are circular, or contain circled arcs, which makes us to believe that the diatoms performed an adaptive migration guided by phototaxis.

Similar experiments in diatom cell motility could be performed using various stimuli such as different light, chemical and thermal condi-

1 *Rule of thumb 2: When a time series is treated as a random walk process and the estimated* H *parameter is close to* 0*, do not trust your result.* in Gao et al. (2006) [56].

tions and apply the same type of analyses in order to see their effects on diatoms.

We believe that these type of analyses have a promising potential in diatom research because of their properties in eliminating any artifact that does not belong to the true signal of the biological system.

■

Part III

APPENDICES

A

DIATOM CULTURE, MEDIUM PREPARATION, AND CELL OBSERVATIONS

In this appendix, we present the protocols used to grow a *Nitzschia* sp. diatom culture and the preparation method for the freshwater Woods Hole culture medium. In addition, based on our observations of their cell motility, we suggest simple procedures for preparing optimal diatom samples in which diatoms display sufficient motility during the observation time.

A.1 GROWTH OF A *Nitzschia* SP. DIATOM CULTURE

Nitzschia sp. cells were previously isolated by members of IM-UASLP from biofilms in rock and soil surfaces that were submerged in a freshwater location near a thermoelectric power plant (San Luis Potosí, México. Summer 2012).

I was responsible of growing subcultures every 10 – 14 days. Axenic subcultures were grown in Woods Hole medium at 25 °C under a 14 : 10 h light/dark cycle with cool white fluorescent light at the IM-UASLP Geomicrobiología lab[1].

Cells were inoculated and grown in either 24 well cell culture plates made of polystyrene (Costar; Corning Incorporated, catalog no. 3524, Corning, New York, NY) or in 1-L conical flasks with continuous oxygen supply (see Figure 72). Cultures grown in flasks were used throughout the experiments or otherwise noted.

The subcultures used in this work had *Nitzschia* sp. diatoms that were able to perform and sustain both cell adhesion and diatom cell motility.

A.2 PREPARATION OF WOODS HOLE CULTURE MEDIA

This method for preparing Woods Hole culture medium (WHM) for freshwater algae and cyanoprokaryota follows from Nichols (1973) [106].

1 Contact: Dr. J. Viridiana García Meza
550 Sierra Leona, Lomas 2a, 78210, San Luis Potosí, SLP, México
Phone: 52 (444) 825 – 3426, jvgm@uaslp.mx

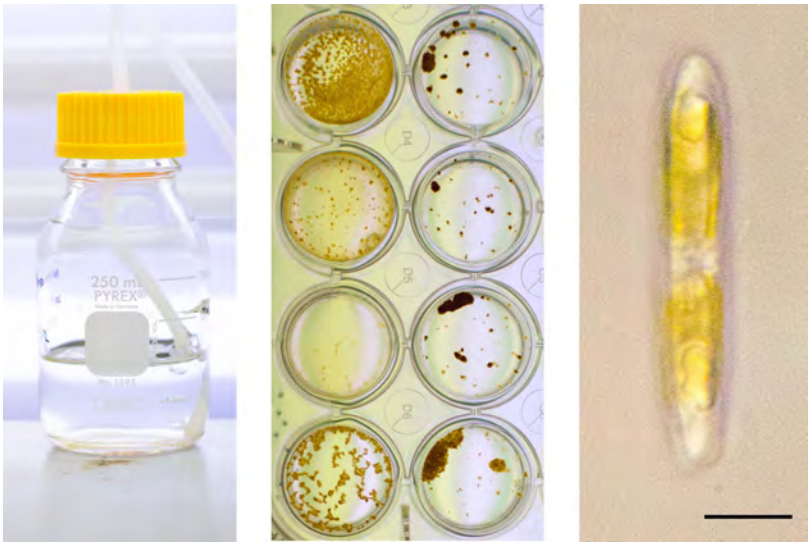

Figure 72: Photographs of *Nitzschia* sp. diatom culture grown in a flask with continuous oxygen supply (left) and in a culture plate (middle). The diameter of each well is 15.6 mm. (right) *Nitzschia* sp. shown in valve view taken by the author at IPICYT, 2013. Scale bar, 6 µm.

MACRONUTRIENTS	
	g/L
$CaCl_2 \cdot 2H_2O$	36.76
$MgSO_4 \cdot 7H_2O$	36.97
$NaHCO_3$	12.60
K_2HPO_4	8.71
$NaNO_3$	85.01

Table 10: WHM stock solutions. Macronutrients.

Stock solutions

To prepare 1 liter of WHM; prepare 5 stock solutions of macronutrients, one solution per line in Table 10 and; 1 stock solution of micronutrients[2], from the list in Table 11.

Macro- and micronutrient solution

Once the stock solutions are available, follow these instructions to make a neutral solution of macro and micronutrients including HEPES and EDTA;

- Add 1 mL of each macronutrient solution, and 1 mL of the micronutrient solution to a 1-L flask with cap.

2 $CCl_2 \cdot 6H_2O$ was not available in the laboratory stock and was not included in the WHM that I prepared for the assays presented in this work.

MICRONUTRIENTS	
	g/L
$MnCl_2 \cdot 4H_2O$	0.18
$ZnSO_4 \cdot 7H_2O$	0.022
$(NH_8)4Mo_7O_{24} \cdot H_2O$	0.0046
$CCl_2 \cdot 6H_2O$	0.012
$CuSO_4 \cdot 5H_2O$	0.01
H_3BO_3	0.06

Table 11: WHM stock solutions. Micronutrients.

- Add 500 mg of HEPES buffer to the solution.
- Adjust the pH of the solution to 7.0 with drops of HCl or NaOH.
- Let the solution sit in the autoclave for 20 min at 120 °C.
- While the macro and micronutrients solution cools down to room temperature, prepare another solution by dissolving Na_2EDTA in deionized water, and $FeCl_3 \cdot 6H_2O$ with the concentrations given in Table 12. (It is recommended to work in a laminar flow hood using a filter to add the reactants following the order listed in Table 12).
- Once the macro and micronutrients solution is at room temperature add 1 mL of the EDTA solution.

Vitamin solution

To prepare a vitamin solution first add biotin and cyanocobalamin as listed in Table 13 (adding 2 drops of HCl). Lastly, add thiamin and let the solution dissolve during night time.

Once the vitamin solution has dissolved, use a filter to add the vitamin solution in deionized water and dissolve in a 500-mL volumetric flask. (It is recommended to work in a flow hood).

Final solution

The final solution of the WHM is made by mixing the macro and micronutrients solution with the vitamin solution plus a silicate solution as follows:

- Add 0.5 mL of the vitamin solution to the macro and micronutrients solution using a filter. (It is recommended to work in a flow hood).

EDTA SOLUTION	
	g/L
Na_2EDTA	4.36
$FeCl_3 \cdot 6H_2O$	3.15

Table 12: EDTA solution.

VITAMINS	
	mg/mL
Biotin	0.1
Cyanocobalamin	1.0
Thiamin-HCl	100

Table 13: Vitamin solution.

- Finally, add 2.0 mL of a $NaSiO_3 \cdot 9H_2O$ silicate solution (14.21 g/L) and stir to dissolve the final solution.

Considerations for using WHM in diatom assays

- WHM is best when used within the preparation day (when the vitamin and silicate solutions were added), and any remaining medium is stored in a refrigerator and covered in aluminum foil to prevent light from degrading the vitamins.
- Stock solutions must be stored in glass flasks in a refrigerator. Flasks are pre-washed in an acid bath for 24 hours, and rinsed in distilled water prior to use. (Waste water should be neutralized afterwards).
- The vitamin stock solution must be stored in a refrigerator and covered in aluminum foil or in an amber flask.

A.3 SUGGESTIONS FOR PREPARING DIATOM SAMPLES

a. Removal of the soluble EPS found dissolved in the medium

It is known that in the medium of *Nitzschia* sp. cultures, a fraction of soluble EPS is found dissolved in the medium as reported by de Brouwer & Stal (2002) [29].

We have seen that the presence of soluble EPS lowers the percentage of observed gliding *Nitzschia* sp. diatoms by more than 30 percent.

We prepared two diatom samples simultaneously, one had an inoculate of diatoms straight from the culture plate with presence of soluble EPS. The other sample had diatoms with fresh medium that replaced the original medium of the culture plate. After two hours of settling the samples in a flow cell (see p. 46 for details about the flow cell), using a microscope we counted the number of diatoms that were gliding continuously an appropriate distance (of a few micrometers) in both samples, and compared the percentage of gliding and non-gliding cells. (Using a 10× objective, the uncertainty in counting gliding cells is about 1 – 3 cells). We repeated the experiment obtaining results that were in agreement with previous days.

The diatom samples in fresh medium (without soluble EPS) had 30 percent more diatoms gliding than those in non-fresh medium. In all of our assays we removed most of the soluble EPS through centrifuging and rinsing, then minimizing the effect it had on the diatom gliding capability.

Method

- Inoculate 300 µL of diatoms in a 2-mL centrifuge tube.
- Centrifuge at 5000 rpm for 1 minute.
- Carefully remove 275 µL of supernatant leaving a diatom pellet.
- Add 275 µL of fresh WHM and vortex for a few seconds until the dilution has no visible aggregates and looks homogeneous.
- Repeat two times centrifuging and replacing with fresh medium.
- Transfer the content to a new centrifuge tube as to avoid EPS being left on the walls of the tube.

b. Time-monitoring of diatom cell motility

We performed a time-monitoring of *Nitzschia* sp. cells to quantify the rate of cell motility and of those that remained immobile. Diatoms within the first four hours presented higher motility rates and nearly all cells were immobile by the first twenty four hours. The complete data is presented in Table 14.

The culture used was 7 days since cultivation date and grown in a cell plate. The diatom sample was prepared as follows:

Method

- An inoculate of 300 µL of diatoms from the stock culture was placed into a centrifuge tube.
- The soluble EPS was removed by centrifuging three times.

Hour (hr)	Time	No. of diatoms/ total	Gliding percentage	Growth day (days)
0	1 PM	44/71	62	7
1	2 PM	62/67	92	7
2	3 PM	81/97	83	7
3	4 PM	84/108	77	7
4	5 PM	60/73	82	7
5	6 PM	87/127	68	7
6	7 PM	97/136	71	7
24	1 PM	7/62	11	8

Table 14: Time-monitoring of diatom cell motility. Diatoms were counted for 15 min. every hour (for six consecutive hours) and after 24 hours since the diatom sample was prepared.

- A diatom sample of 7 μL was flown inside a flow cell.
- Immediately after, the sample was observed in a microscope were cells were counted for 15 minutes starting from the bottom of the flow cell until the length of time was reached.
- Once the cell counting was completed the microscope illumination was turned off.
- We repeated the 15-minute counting every hour for 6 consecutive hours and after 24 from the initial preparation of the sample.

B

COMPUTER ALGORITHMS AND ROUTINES USED IN THIS WORK

In this appendix, algorithms used in our data analyses are presented

We digitized between 5000 to 8000 video frames per assay in the two experiments done in this work (5 min. at 25 fps, using VirtualDUB 1.9.11, Source-forge.net). Each frame went under a basic digital image processing of cropping, color inversion, and batch exporting of frames as 'text files' (ImageJ 1.46, National Institutes of Health). The next step was to use the frame sequence as input into an in-house tracking routine that analyzes each frame and determines the overall in-plane positions in time of individual diatoms or microspheres.

B.1 DIGITAL VIDEO PROCESSING

Uncompressed video files (`.avi`) were opened separately in ImageJ as grayscale virtual stacks, and color inversion was applied to the entire stack. Furthermore, a macro was run for exporting each frame as a text image in a dedicated folder for a single video.

For the TBM experiment, the macro in Listing 1 was used. Otherwise, for the diatom motility experiment, the macro in Listing 2 was used.

B.2 CELL AND PARTICLE TRACKING

This LabVIEW routine was largely developed by Braulio Gutiérrez,[1] and I collaborated only in optimizing run-times. To perform the tracking of a diatom cell or a particle from video frames using this VI,[2] each frame must be a text image. Use the ImageJ macros available above.

Front panel: How to use the tracking routine

SETTING UP THE VI:

- Use the `folder` button on the top left corner to choose the folder containing the video frames (stored as text images).

1 Contact: Dr. Braulio Gutiérrez Medina
2055 Camino a la Presa San José, Lomas 4a, 78216, San Luis Potosí, SLP, México
Phone: 52 (444) 834 – 2000, bgutierrez@ipicyt.edu.mx

2 The name associated with programs created using LabVIEW (National Instruments, Austin, TX).

Listing 1: Tethered Brownian motion. ImageJ macro.

```
// ImageJ 1.46 macro. It saves a frame as a "text image."
// diatoms-biofilm tethered brownian motion. Spring 2013

// Creates a directory using the filename and location.

dir = getDirectory("image");
name = getTitle;
path = dir + name;
myDir = path + "_ij" + File.separator;
File.makeDirectory(myDir)

// Saves a text image for each chosen frame.

i = 1;
j = 1;
currentslice=i;

   while (j<=10000) {
saveAs("Text Image",myDir + name + "_" + j);
currentslice=j; // When it's equal to "i" it does a time-lapse,
    otherwise saves all frames.
setSlice(currentslice);
i = (j * 25) + 1;
j = j + 1;
}
```

Listing 2: Diatom motility. ImageJ macro.

```
// ImageJ 1.46 macro. It saves a frame as a "text image."
// diatom motility. Spring 2013

// Creates a directory using the filename and location.

dir = getDirectory("image");
name = getTitle;
path = dir + name;
myDir = path + "_ij" + File.separator;
File.makeDirectory(myDir)

// Saves a text image for each chosen frame.

i = 1;
j = 1;
currentslice=i;

   while (j<=10000) {
saveAs("Text Image",myDir + name + "_" + j);
currentslice=i; // When it's equal to "i" it does a time-lapse,
    otherwise saves all frames.
setSlice(currentslice);
i = (j * 25) + 1; // Saves a text image every 25 frames including
     the first  frame.
j = j + 1;
}
```

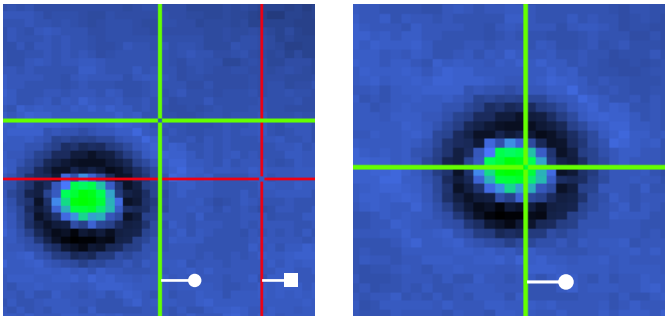

(a) (b)

Figure 73: Cell and particle tracking GUI. (a) A rectangular region applied for background subtraction is delimited by a green (indicated with a circle) and red (indicated with a square) cursors. (b) The initial in-plane position of a microsphere is localized by a green cursor (circle) before background is subtracted and the actual unassisted tracking is started. Video frames shown have colors linearly interpolated.

- In the front panel, change `image prefix` and `affix`. For example, if your text images have filenames;

  `100_1.txt, a100_2.txt, a100_3.txt`; the image prefix is "`a100_`" and the affix "`_1`".

- Next, type the `number of frames` and next to the `Load` button type "`1`" for loading the first frame.

Run the VI with `Command + R` or the white arrow in the LabVIEW menubar.

LOADING A FRAME: Use the `Load` button to load the first frame. The first frame appears in the front panel but with different colors than the original video frame. These correspond to different intensities; having dark blue as the lowest value, and bright green as the highest.

NOISE REMOVAL: The tracking algorithm works best when the object of interest in the image contrasts with its background. By reducing its background noise, its in-plane position is determined with ease when averaging over intensity values that differ largely and gives accurate positional coordinates.

- Once the first frame has loaded (see Figure 73a), with the green and red cursors, indicated by a circle and a square respectively, draw a region that is not over the object of interest (region of interest, ROI).

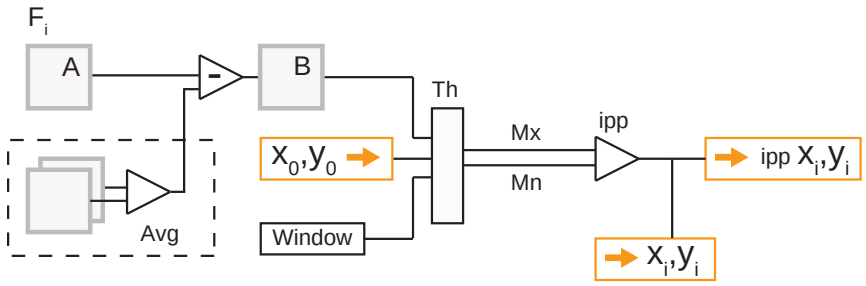

Figure 74: Flow diagram of digital image processing and tracking of the position of an object. See text for complete description.

The green cursor must be in the upper left edge of the region, while the red cursor in the lower right as shown in Figure 73a.

- To reduce noise effectively, select a region with bright pixels.
- Lastly, hit the `Remove` button and the VI will register the background noise intensity value in its memory and will use it for all remaining frames.

PARTICLE TRACKING: Place the green cursor (circle indicator) on top of the object of interest where it has the highest intensity you could see. It doesn't need to align the *highest* value perfectly, as in Figure 73b, because this is done only for helping the program to know what object it should track.

- Click on the `Init` button to define the first coordinate of its center of mass.
- Finally, click on the `TRACK` button to start the tracking algorithm. While it collects data, the "CM Cursor-1" graphs the position versus time, in pixels and frames respectively, and stores the coordinates in a text file under a `Results/` folder.

Hit the `STOP` button to end running the VI.

Flow diagram: Operations for the digital image processing of the tracking routine

In Figure 74, a video frame F_i is input into the tracking routine where its colors are interpolated into a broad intensity spectrum. In the dashed area, F_i is shown to go through operations of background acquisition and subtraction. Frame B is the same as A but with the background subtracted. A function *Th* computes the threshold maximum (Mx) and minimum (Mn) values of the inputs B, an initial position (x_0, y_0), and a window size delimiting the ROI. The values Mx and Mn are applied to B to compute the in-plane position (x_i, y_i) of the object of interest, shown by an operator *ipp*, and it is saved in

a text file. The position is used in subsequent frames F_{i+1} resulting in the tracking of the object.

For each frame iteration, a collection of in-plane positions is saved in a text file that we further use in our data analysis.

B.3 ALGORITHMS FOR DATA ANALYSIS

TBM RMS_t moving average algorithm

Listing 3: RMS_t moving average algorithm for a time series X(k).

```
Constants for X(k):
time_window <-- INPUT

for all rounds r > 0
        X(k) <-- TIME SERIES
        sum X(k+r) <-- INCR_r
        mean INCR_r
OUTPUT (RMS_t)
```

Diatoms, crossings algorithm

Listing 4: Crossings algorithm for diatom time series X(k).

```
Constants for X(k):


For all rounds r > 0
```

Wavelet transform DFA

Following from Ihlen [80].

Listing 5: Wavelet transform Detrended Fluctuation Analysis (WT-DFA) algorithm.

```
Constants for X(k):
fi

For all rounds r > 0
```

B.4 OTHER CODE AND SIMULATIONS

Brownian and TBM simulation

Listing 6: Brownian and TBM simulation.

```
Constants for X(k):
random_distribution  <-- INPUT
```

```
tether_length <-- INPUT

for all rounds r > 0
        rand <-- RANDOM
        if rand > .5
                sum rand(k+r) <-- INCR_r
                X(k) <-- TIME SERIES
                if      k > tether_length
                                k = k - randm
                                X(k) <-- TIME SERIES
        if rand < .5
                sum rand(k-r) <-- INCR_r
                X(k) <-- TIME SERIES
                if      k > tether_length
                                k = k - randm
                                X(k) <-- TIME SERIES
OUTPUT (X(k))
```

C

DIATOM TRAJECTORIES

In this appendix, all the trajectories from individual diatoms that were analyzed are shown along with their corresponding time-lapsed sequence.

C.1 TRAJECTORIES

The trajectories were divided into two classes according to their radius of curvature described along various segments of the full trajectory. The first class of circular trajectories shown to be smooth and therefore we assigned them the letter O. A second class of non-circular trajectories was not smooth as the previous class, and we assigned to them the letter V.

C.1.1 *Circular trajectories: O*

Trajectories O1-O97, Figure 75 to Figure 107, respectively, are found in pp. 106-138.

C.1.2 *Non circular trajectories: V*

Trajectories V1-V44, Figure 107 to Figure 122, respectively, are found in pp. 138-153.

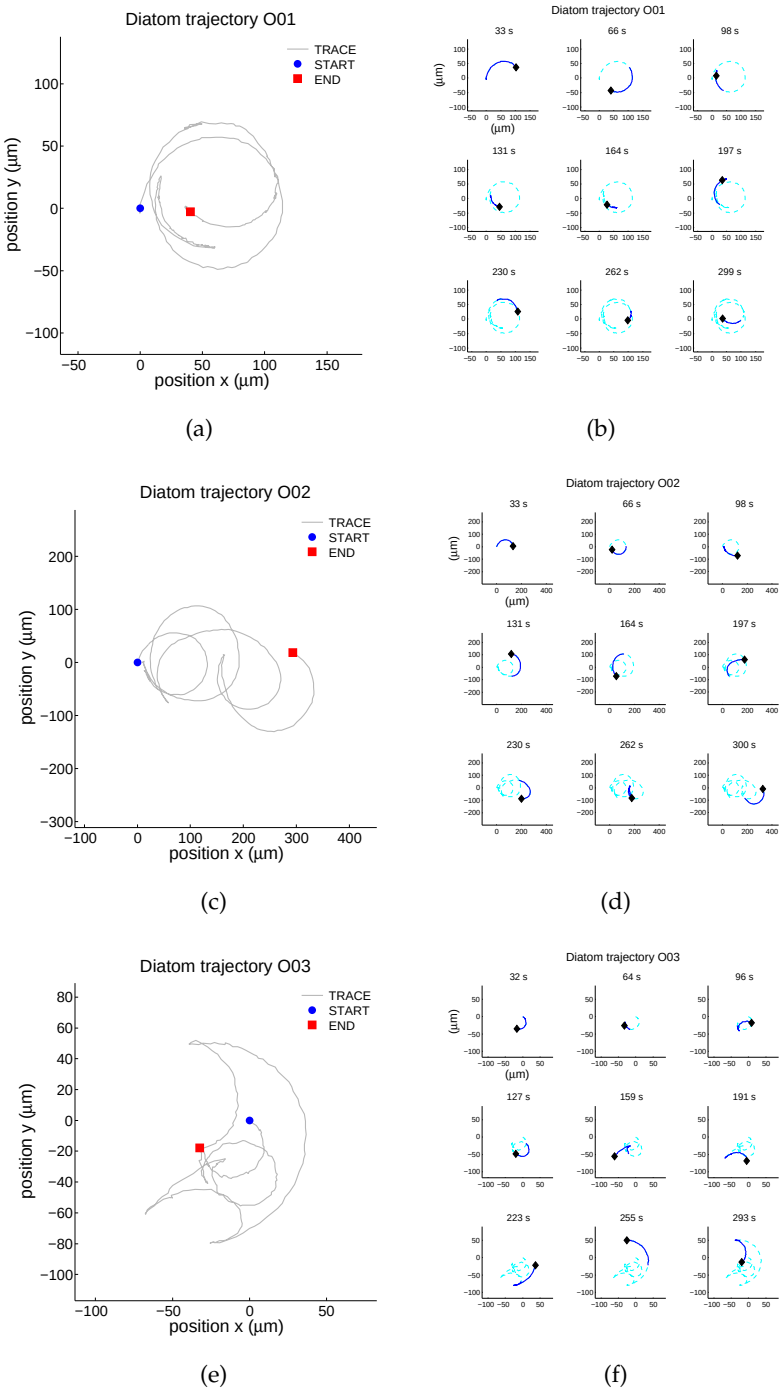

Figure 75: *Nitzschia* sp. diatom trajectories O 1-3. (a, c, e) Trajectory (b,c f) Time-lapsed trajectories.

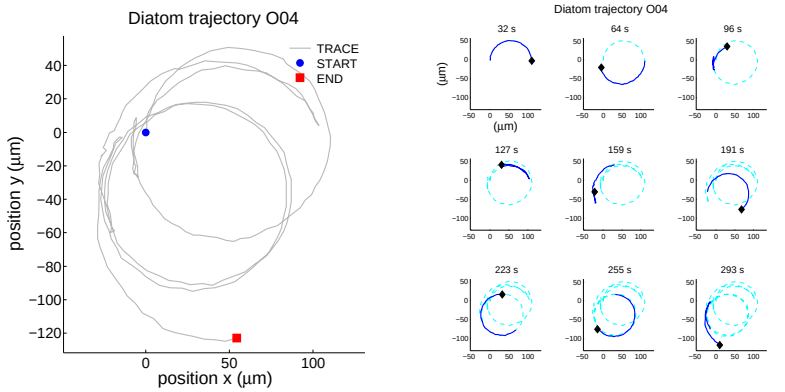

(a) (b)

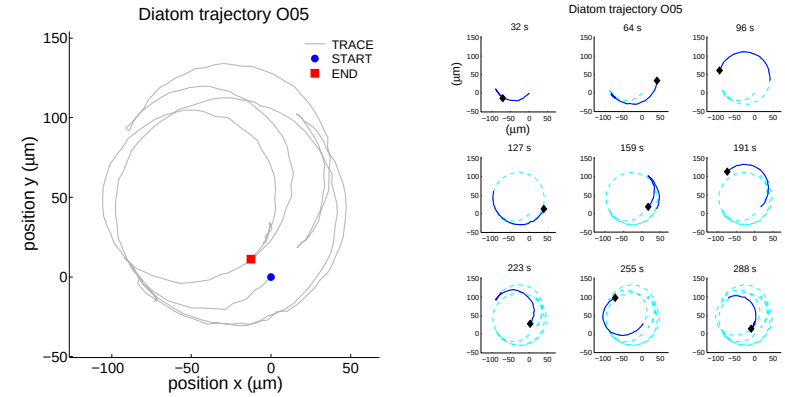

(c) (d)

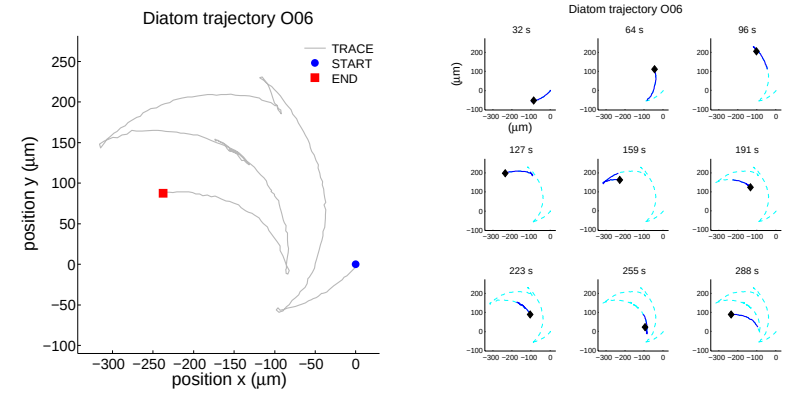

(e) (f)

Figure 76: *Nitzschia* sp. diatom trajectories O 4-6

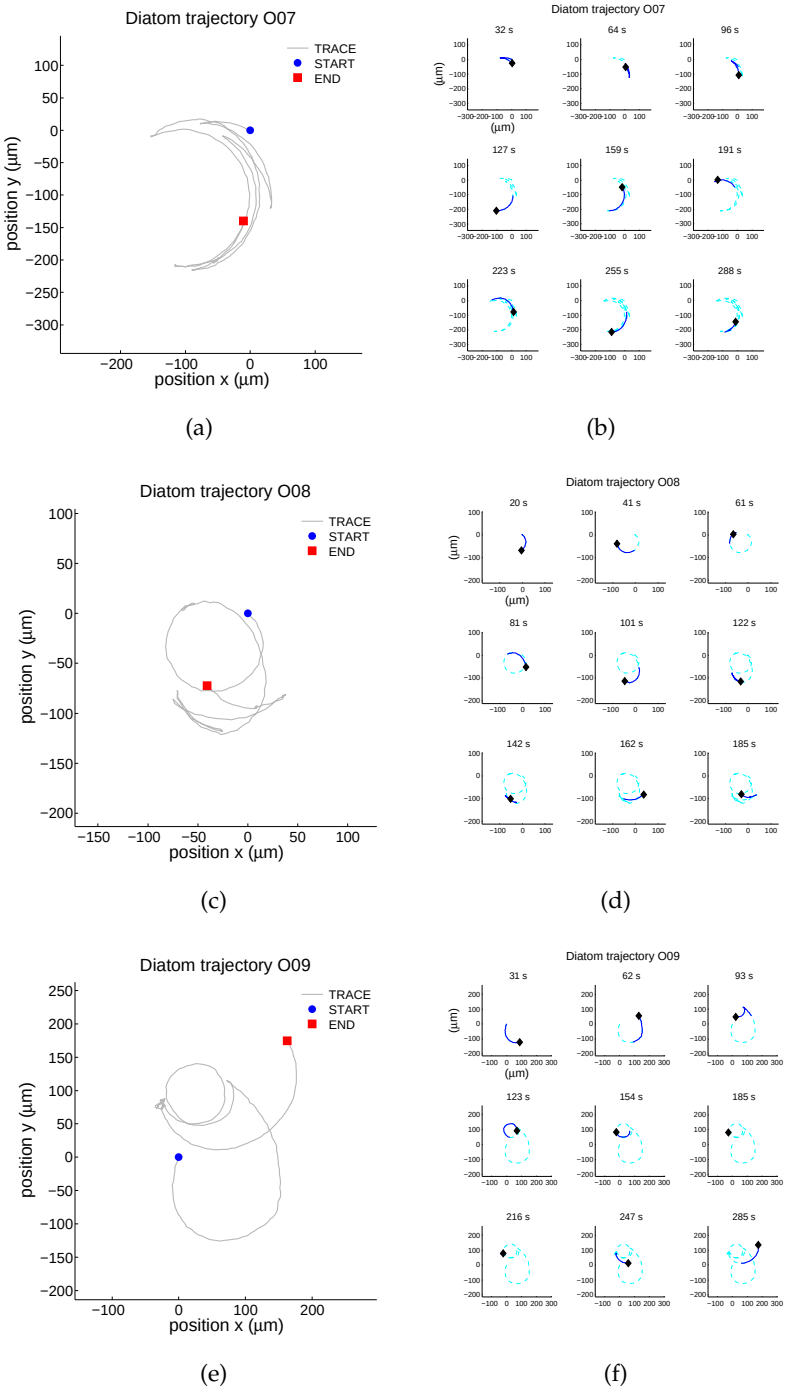

Figure 77: *Nitzschia* sp. diatom trajectories O 7-9. (a, c, e) Trajectory (b,c f) Time-lapsed trajectories.

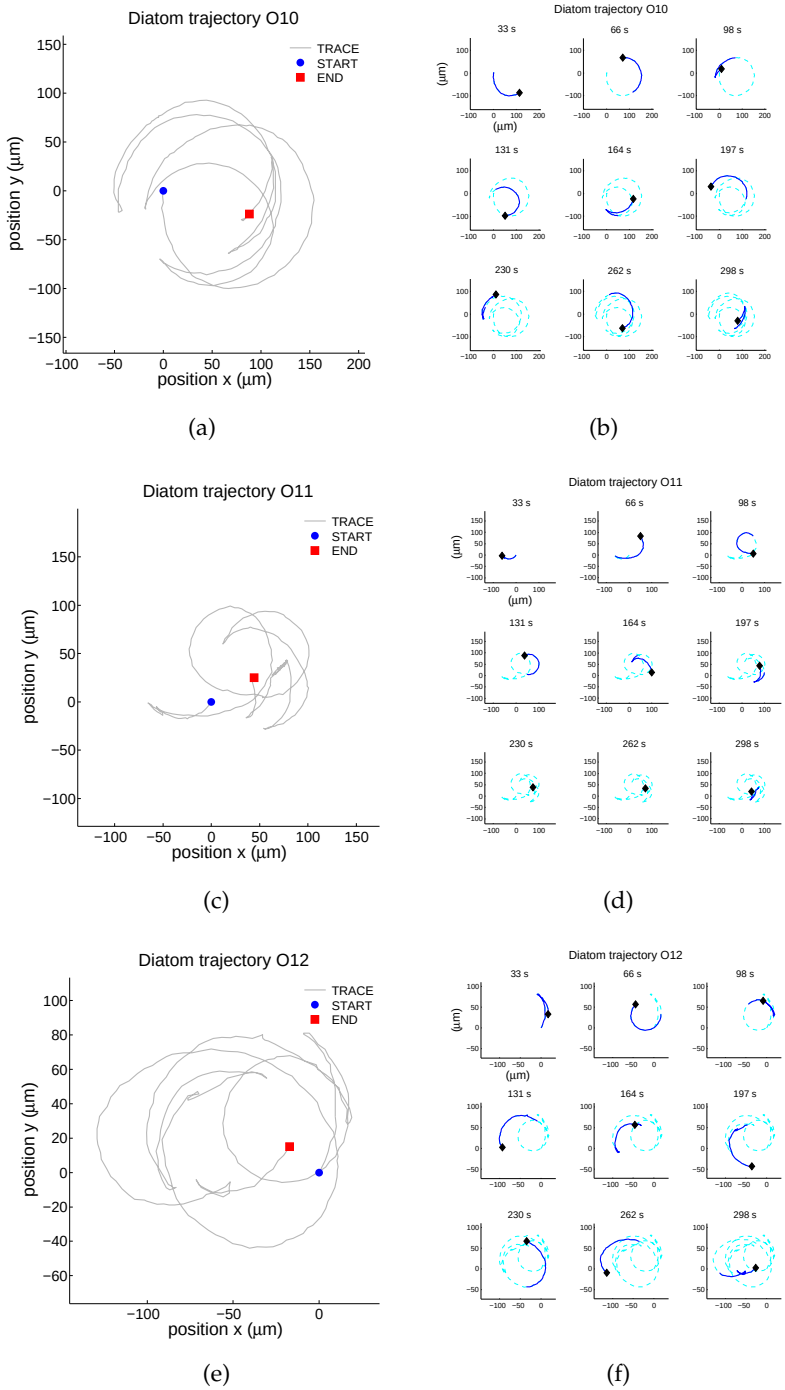

(a) (b)

(c) (d)

(e) (f)

Figure 78: *Nitzschia* sp. diatom trajectories O 10-12

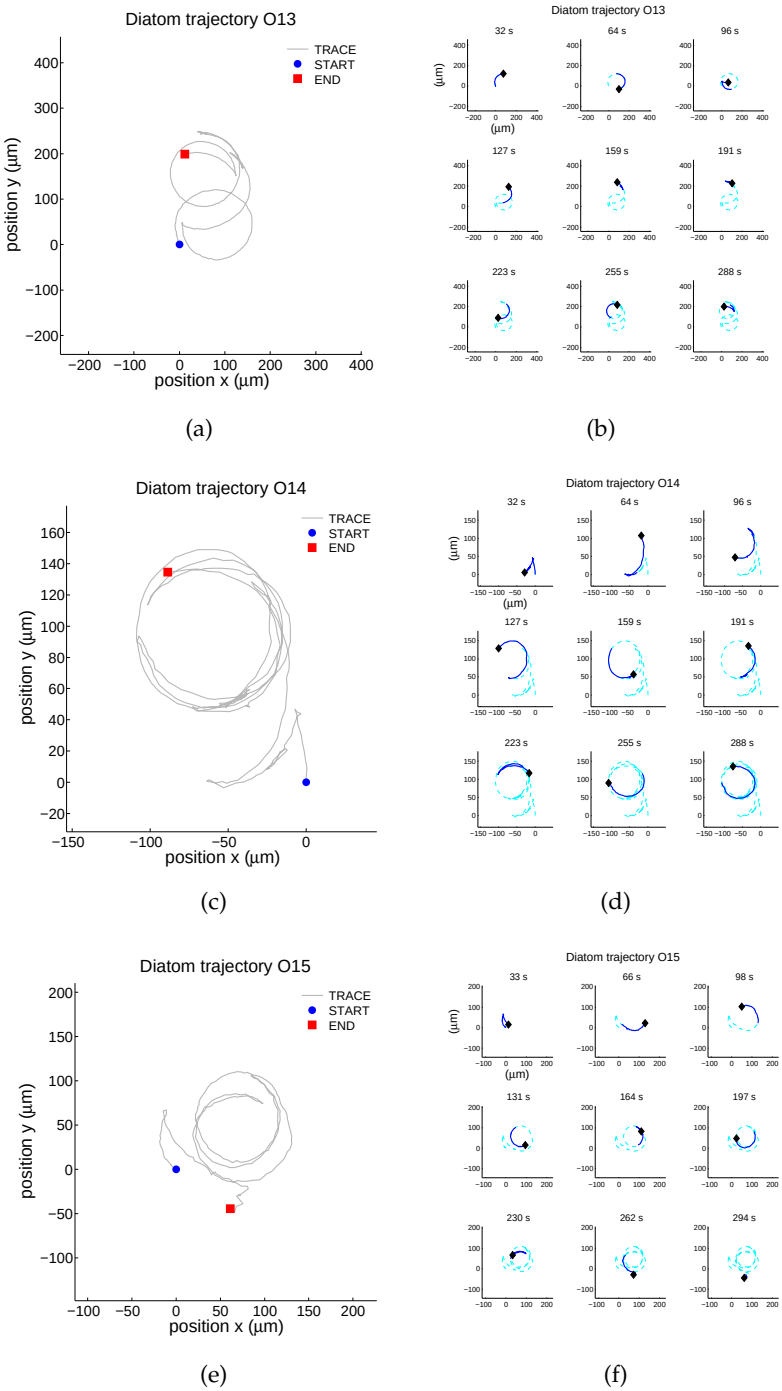

Figure 79: *Nitzschia* sp. diatom trajectories O 13-15. (a, c, e) Trajectory (b,c f) Time-lapsed trajectories.

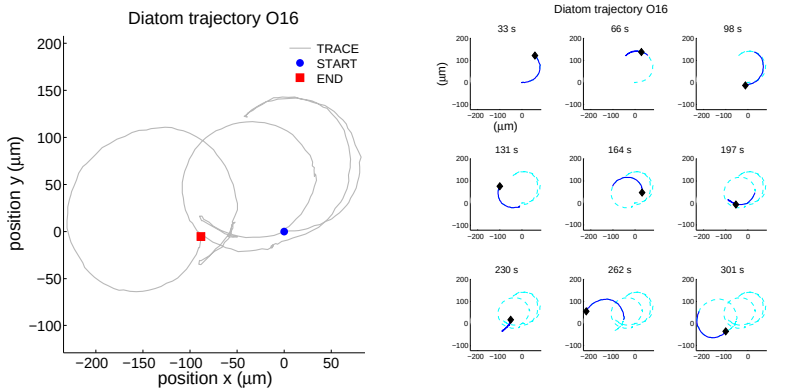

(a) (b)

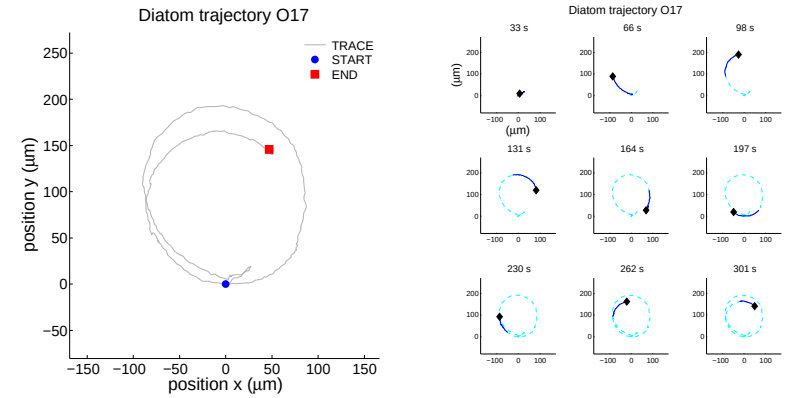

(c) (d)

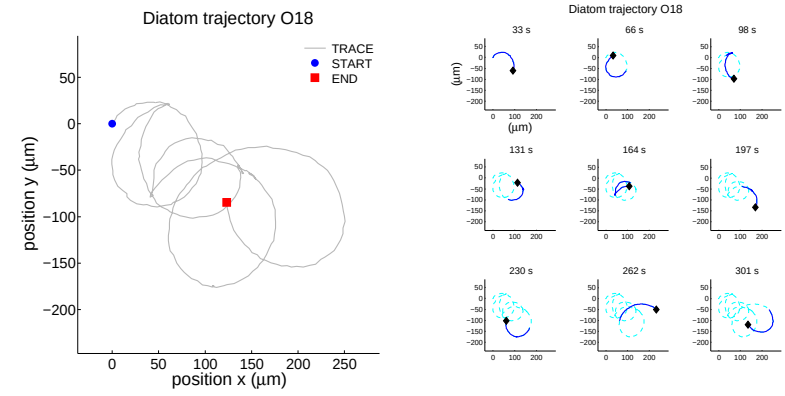

(e) (f)

Figure 80: *Nitzschia* sp. diatom trajectories O 16-18

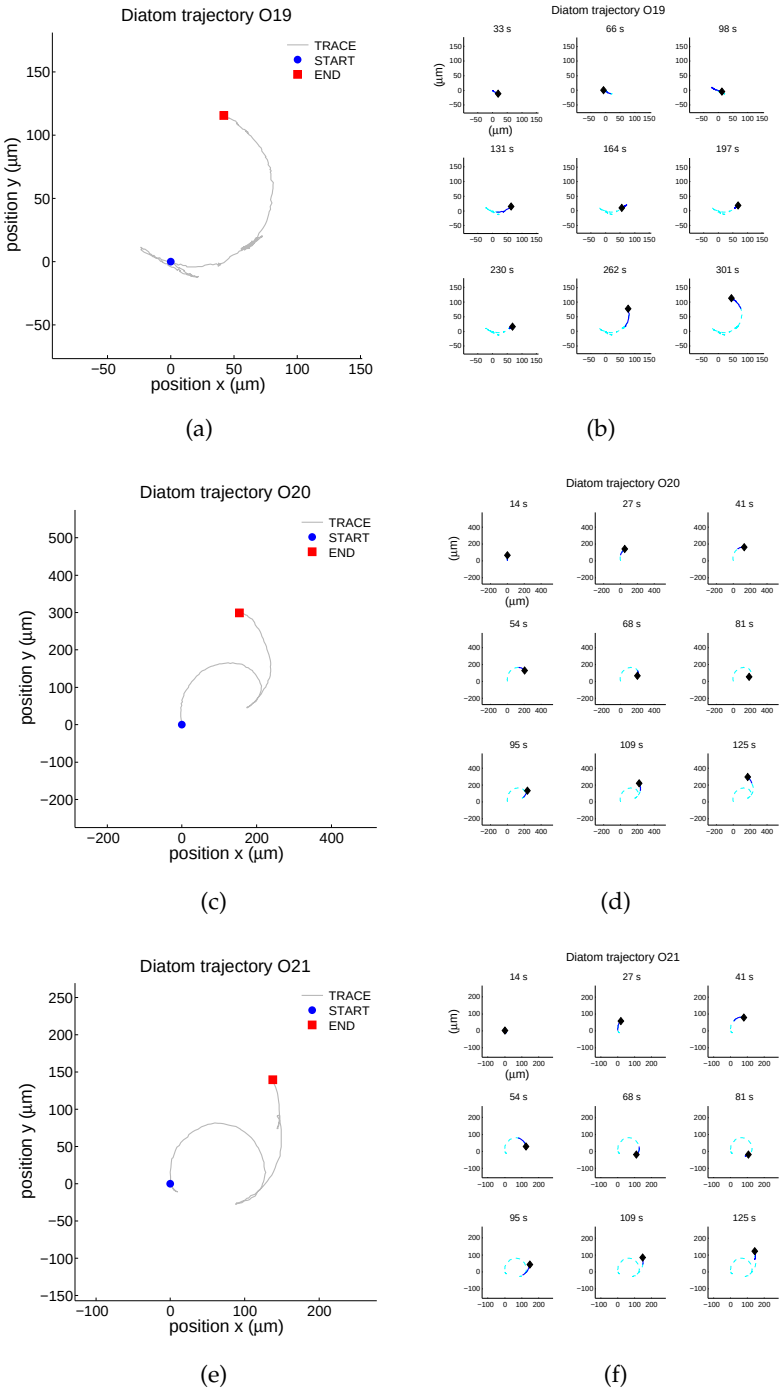

Figure 81: *Nitzschia* sp. diatom trajectories O 19-21. (a, c, e) Trajectory (b,c f) Time-lapsed trajectories.

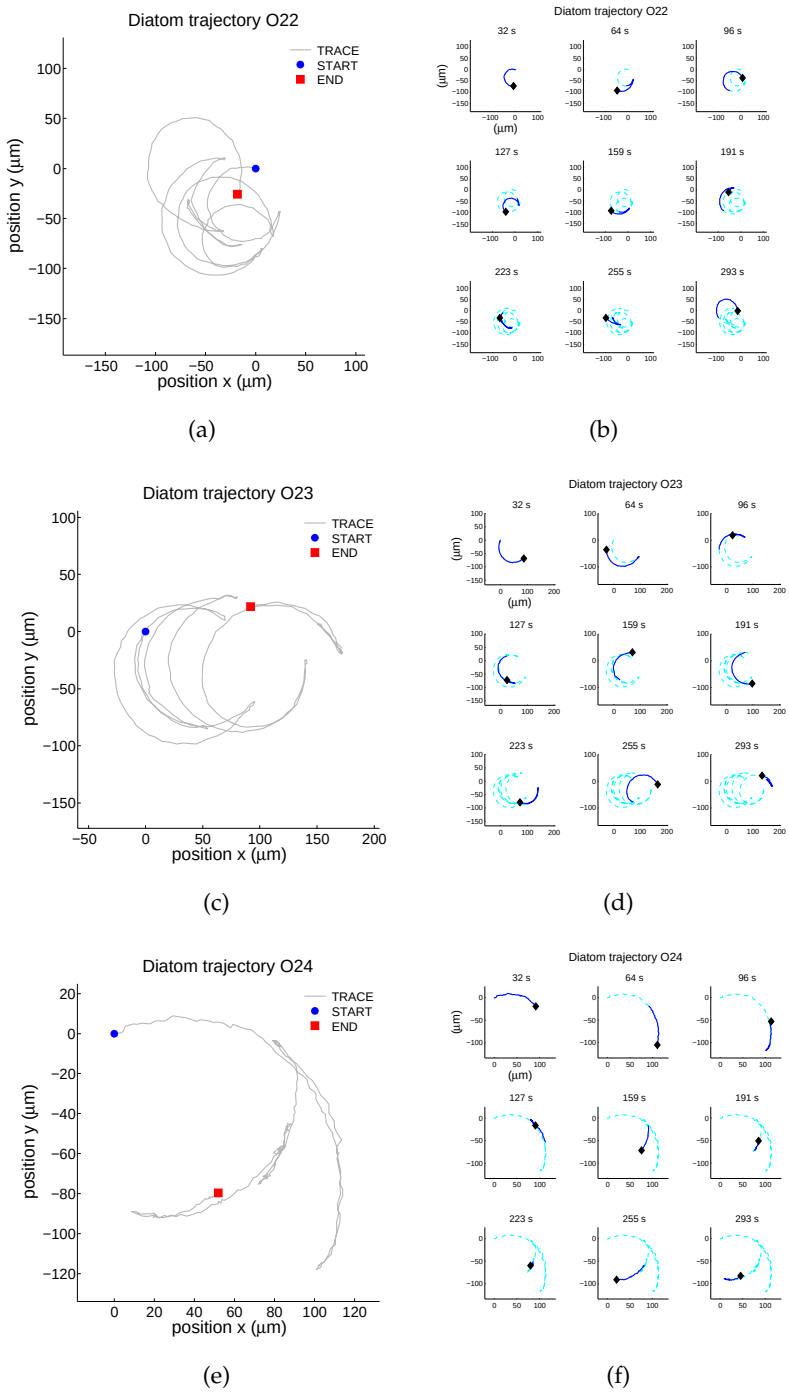

Figure 82: *Nitzschia* sp. diatom trajectories O 22-24

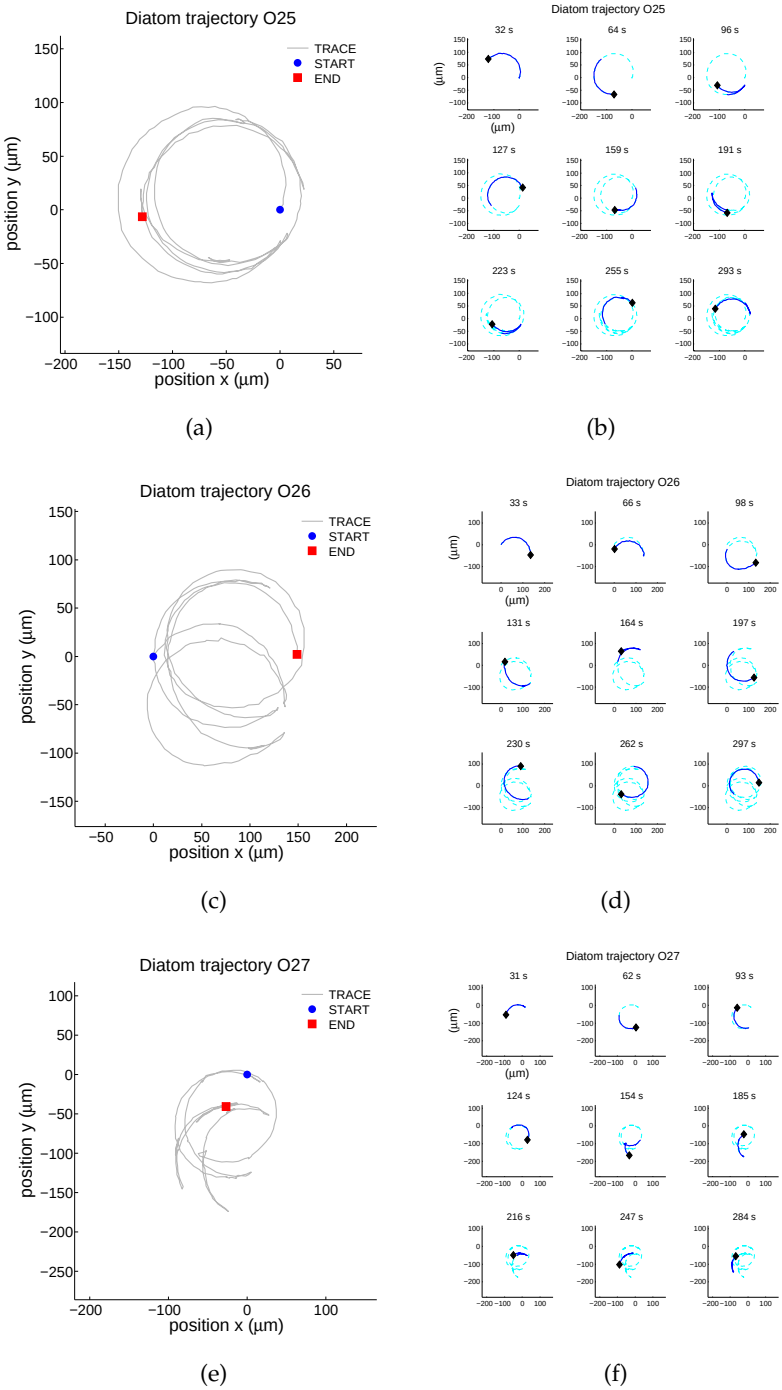

Figure 83: *Nitzschia* sp. diatom trajectories O 25-27. (a, c, e) Trajectory (b,c f) Time-lapsed trajectories.

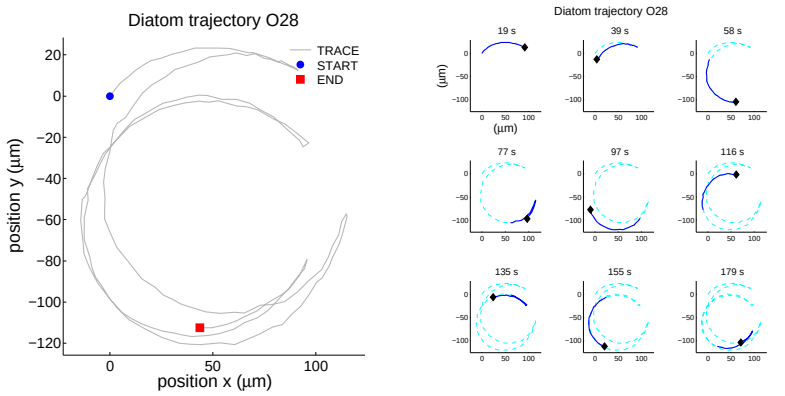

(a) (b)

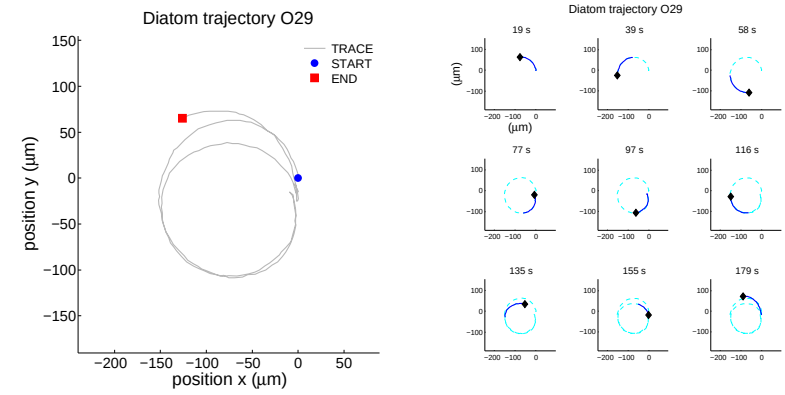

(c) (d)

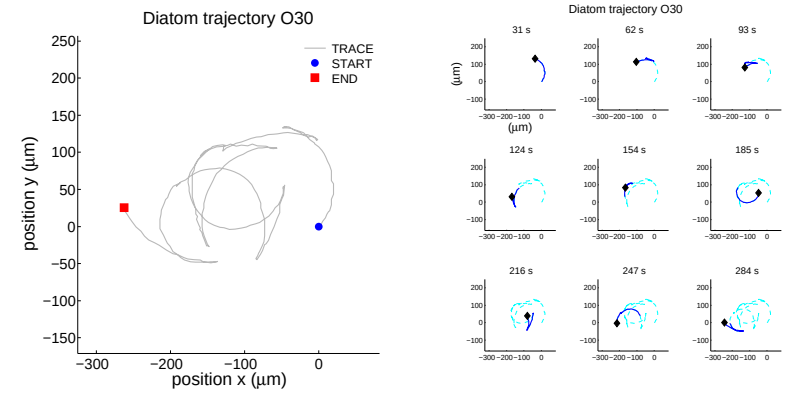

(e) (f)

Figure 84: *Nitzschia* sp. diatom trajectories O 28-30

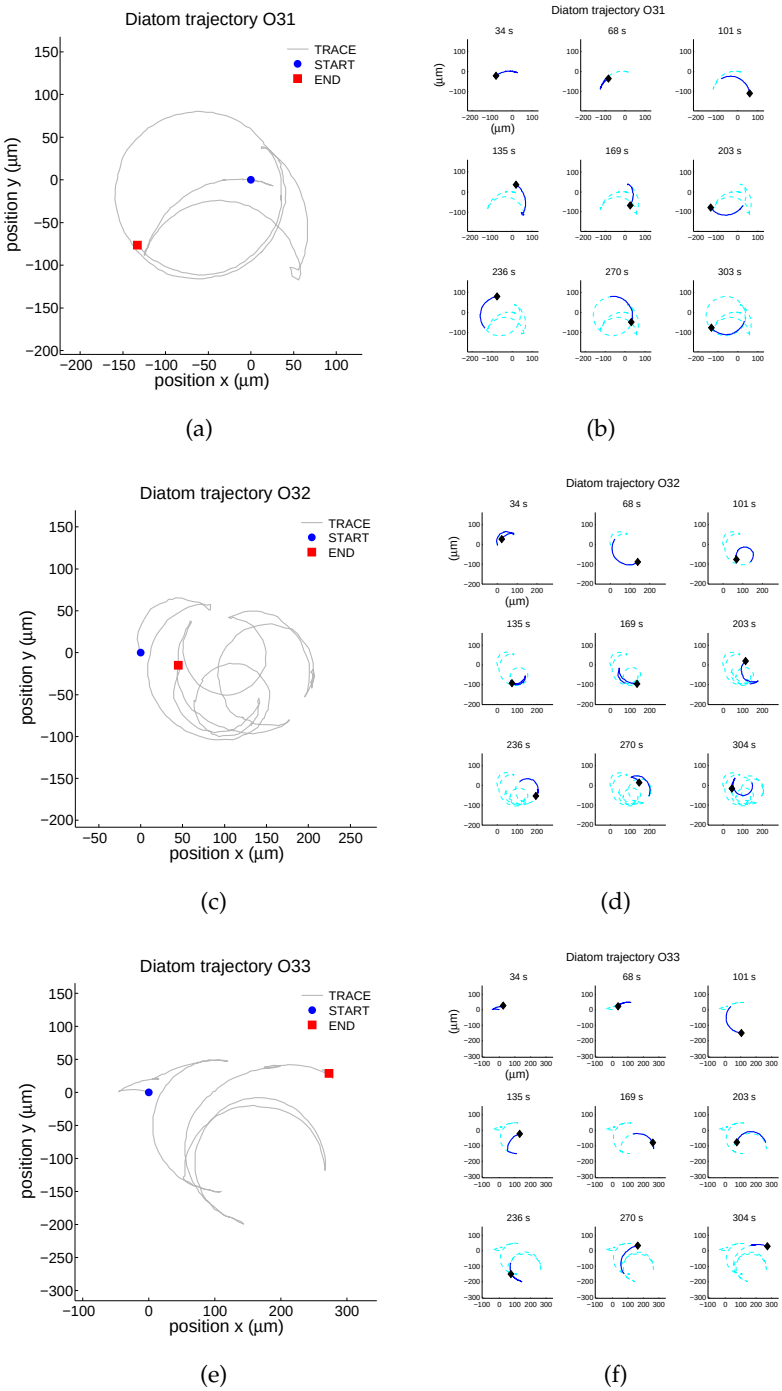

Figure 85: *Nitzschia* sp. diatom trajectories O 31-33. (a, c, e) Trajectory (b,c f) Time-lapsed trajectories.

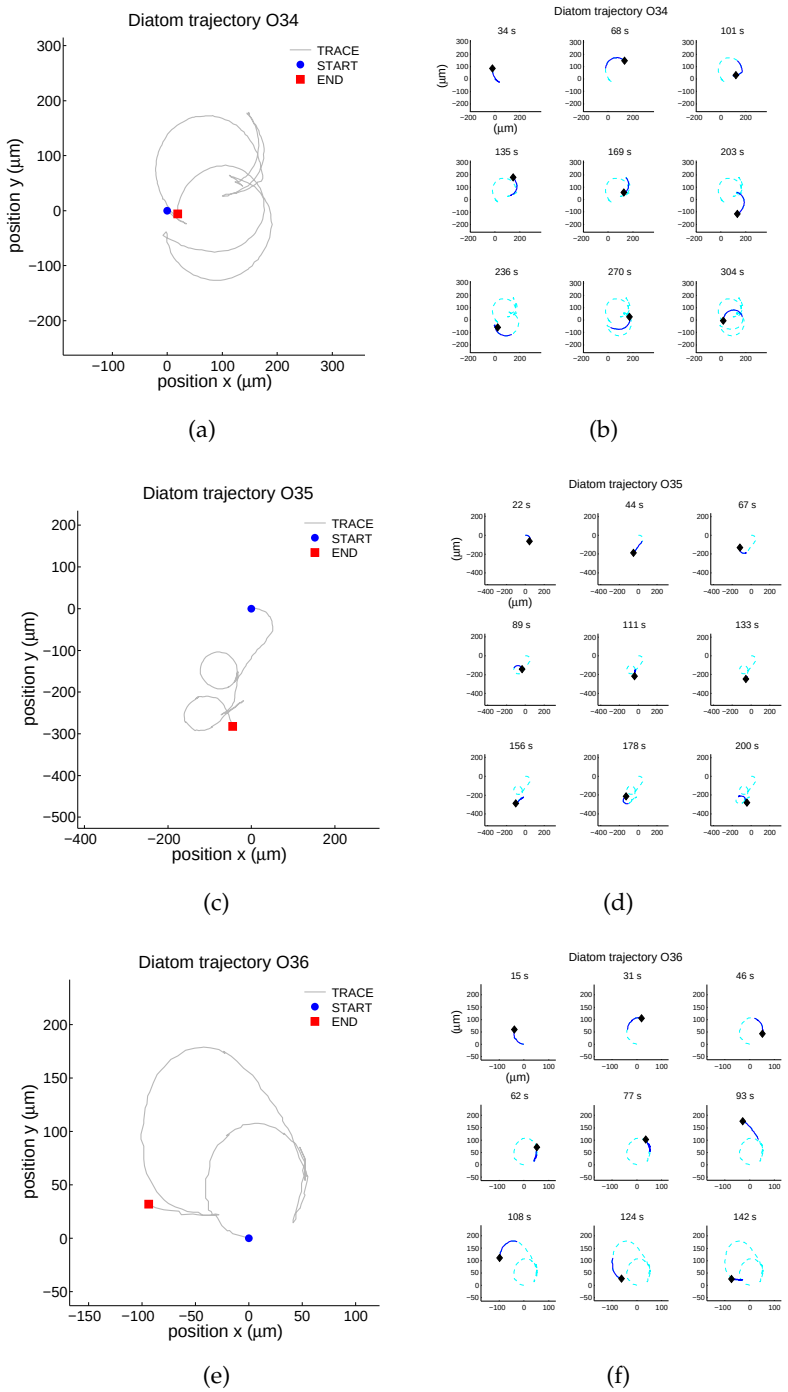

Figure 86: *Nitzschia* sp. diatom trajectories O 34-36

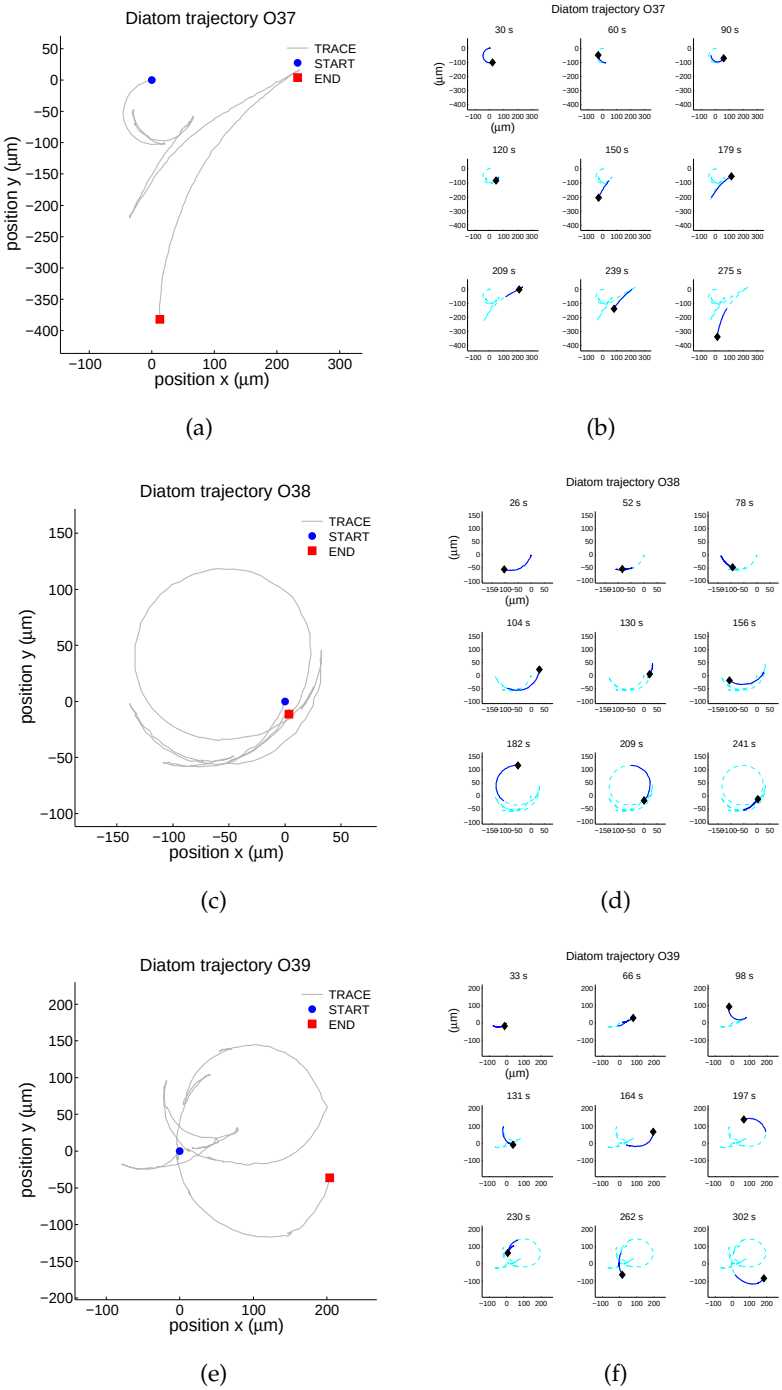

Figure 87: *Nitzschia* sp. diatom trajectories O 37-39. (a, c, e) Trajectory (b,c f) Time-lapsed trajectories.

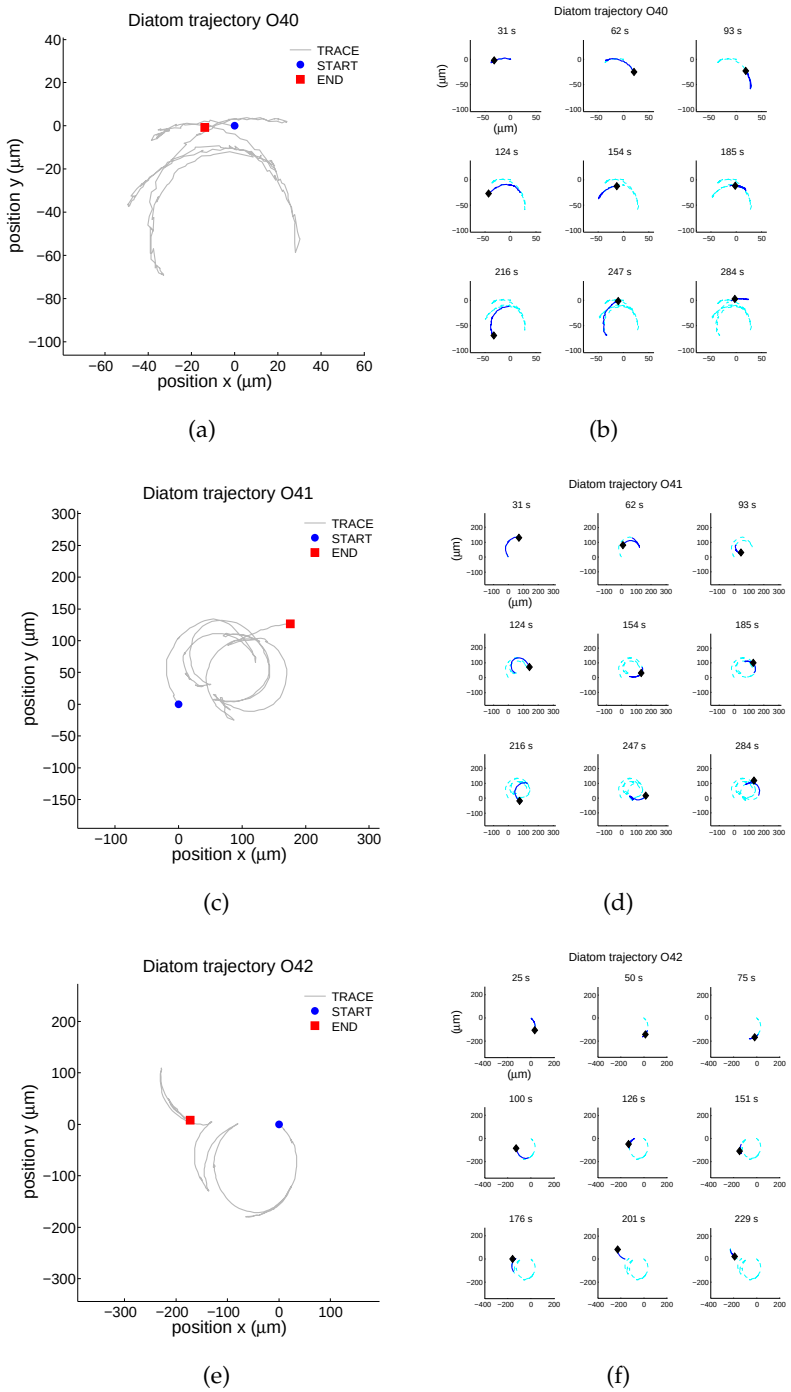

Figure 88: *Nitzschia* sp. diatom trajectories O 40-42

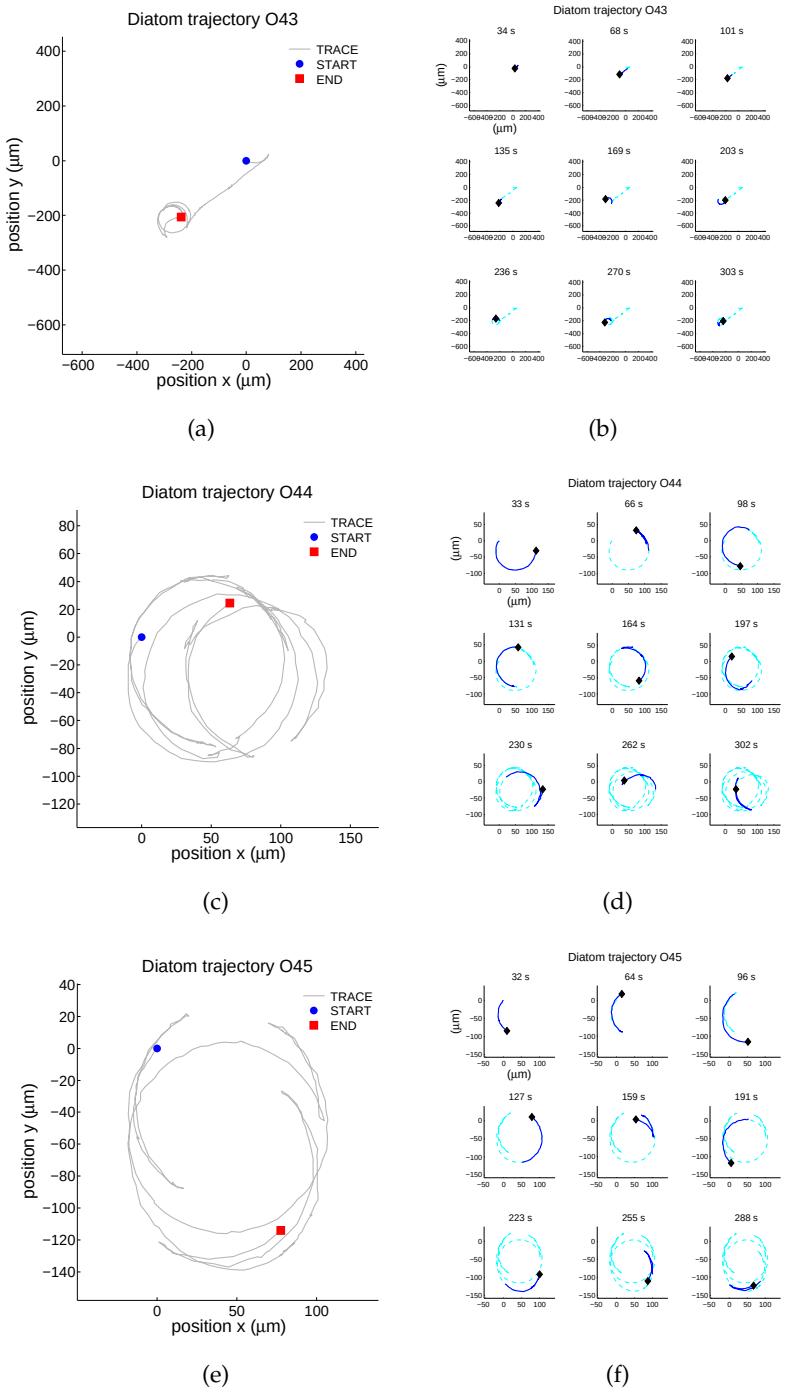

(a) (b)

(c) (d)

(e) (f)

Figure 89: *Nitzschia* sp. diatom trajectories O 43-45. (a, c, e) Trajectory (b,c f) Time-lapsed trajectories.

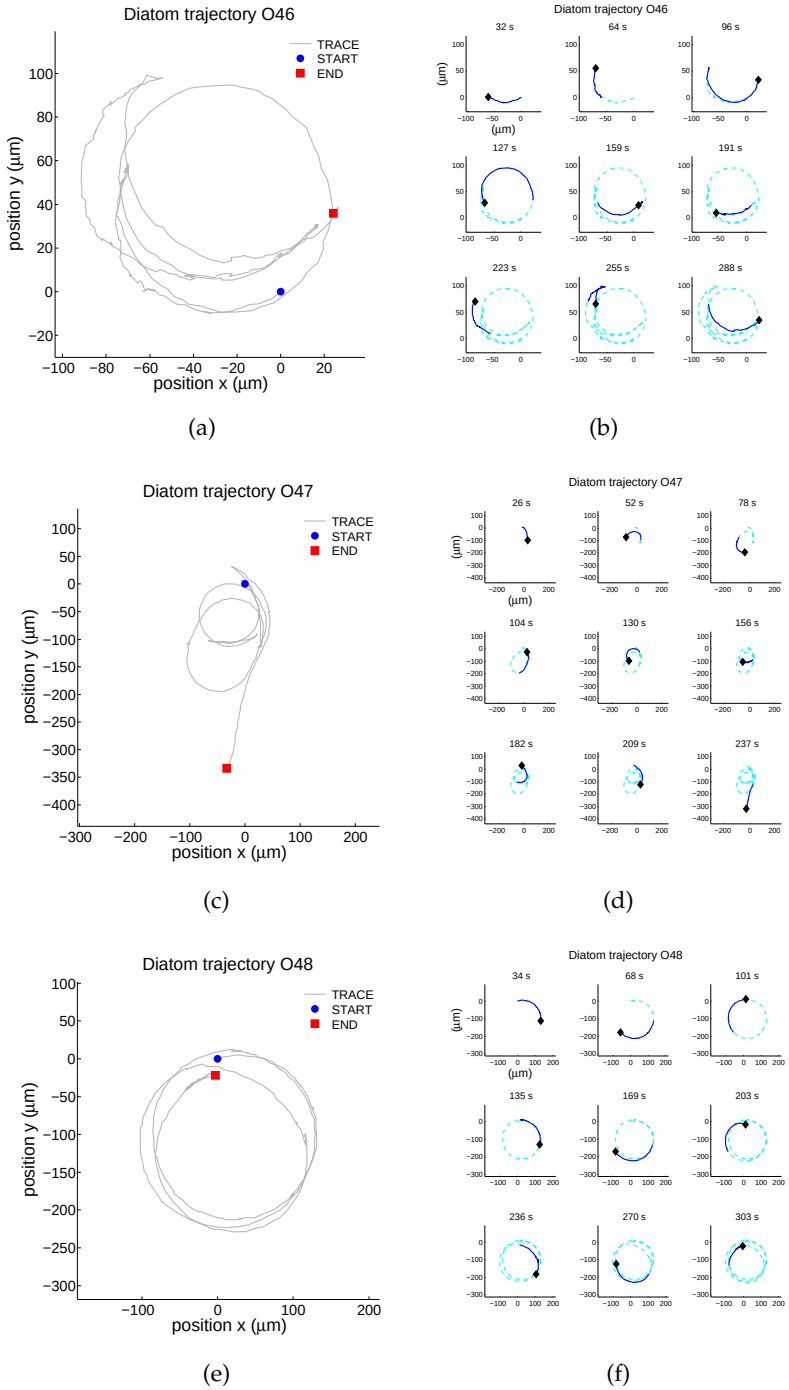

Figure 90: *Nitzschia* sp. diatom trajectories O 46-48

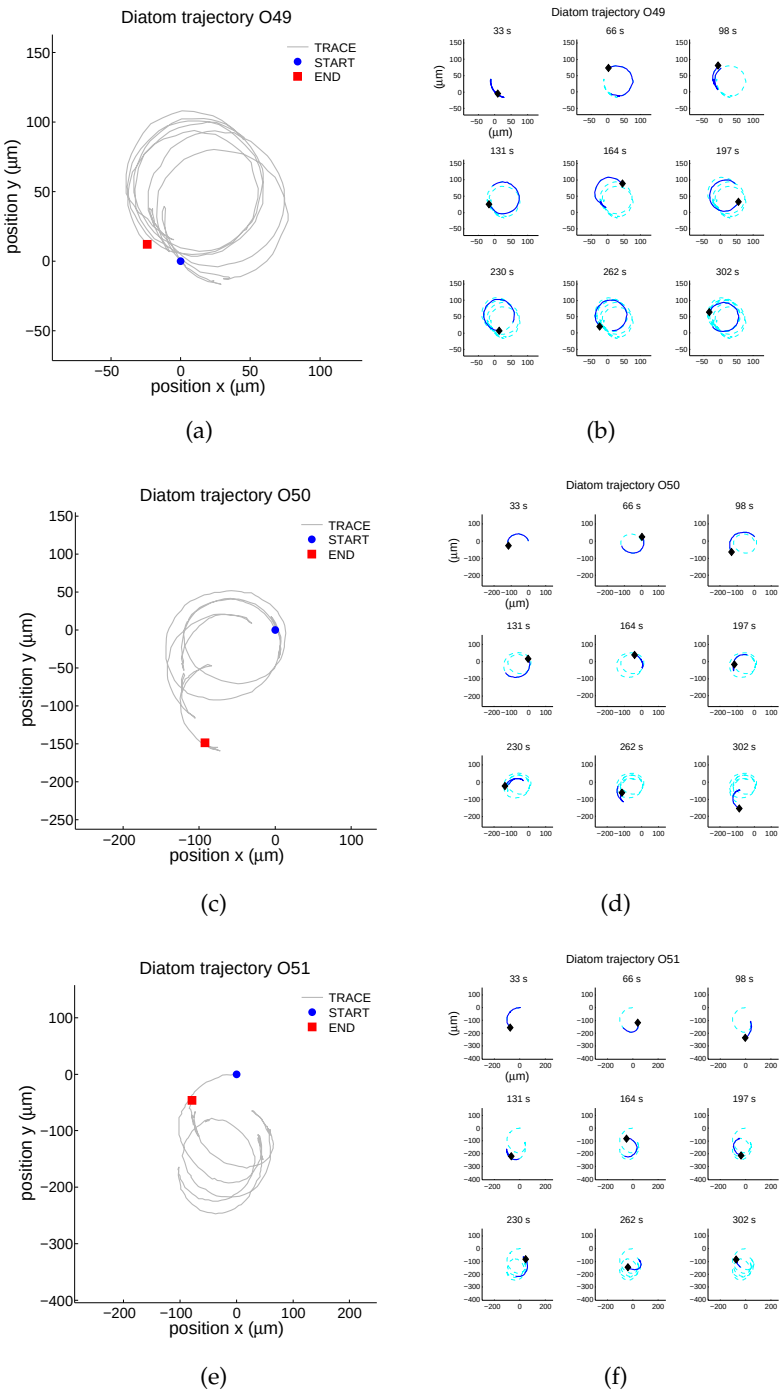

Figure 91: *Nitzschia* sp. diatom trajectories O 49-51. (a, c, e) Trajectory (b,c f) Time-lapsed trajectories.

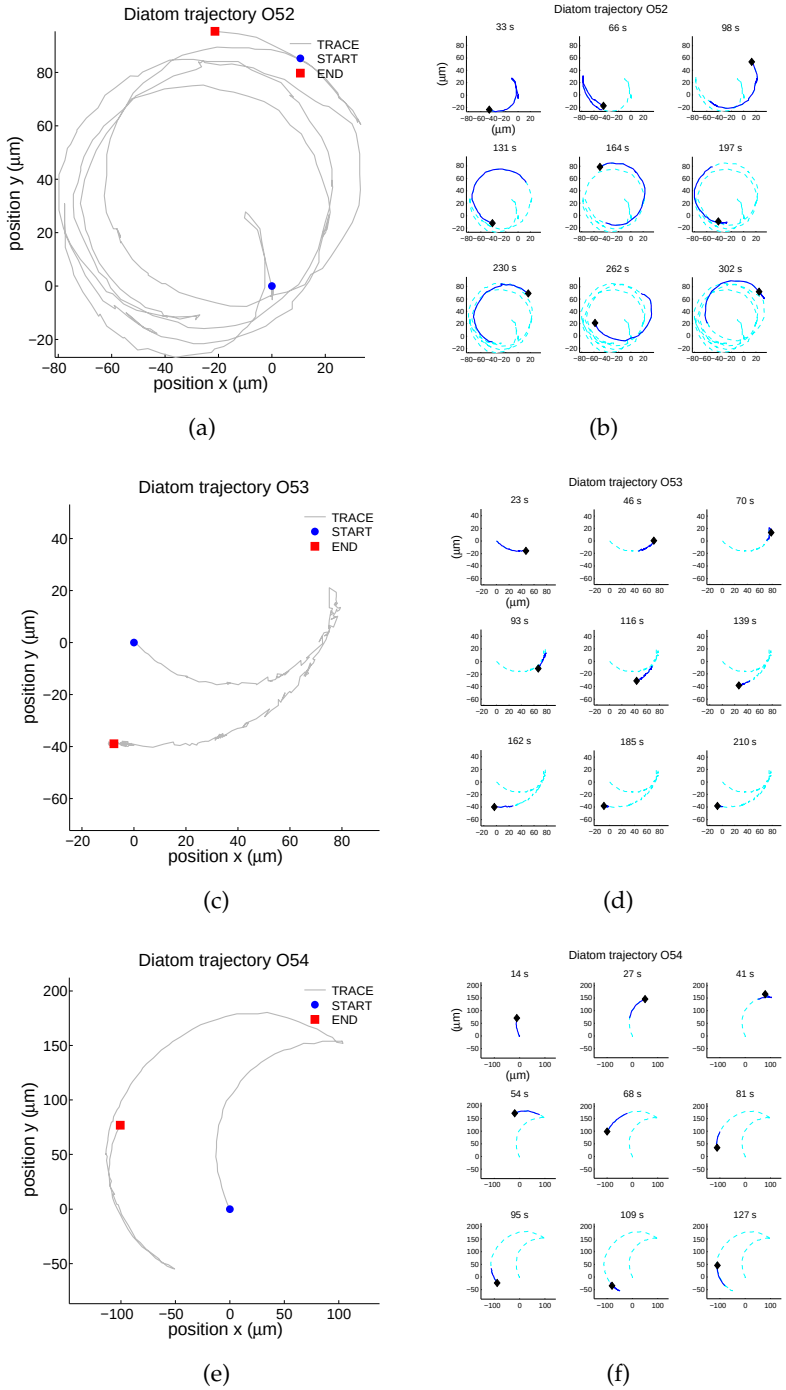

Figure 92: *Nitzschia* sp. diatom trajectories O 52-54

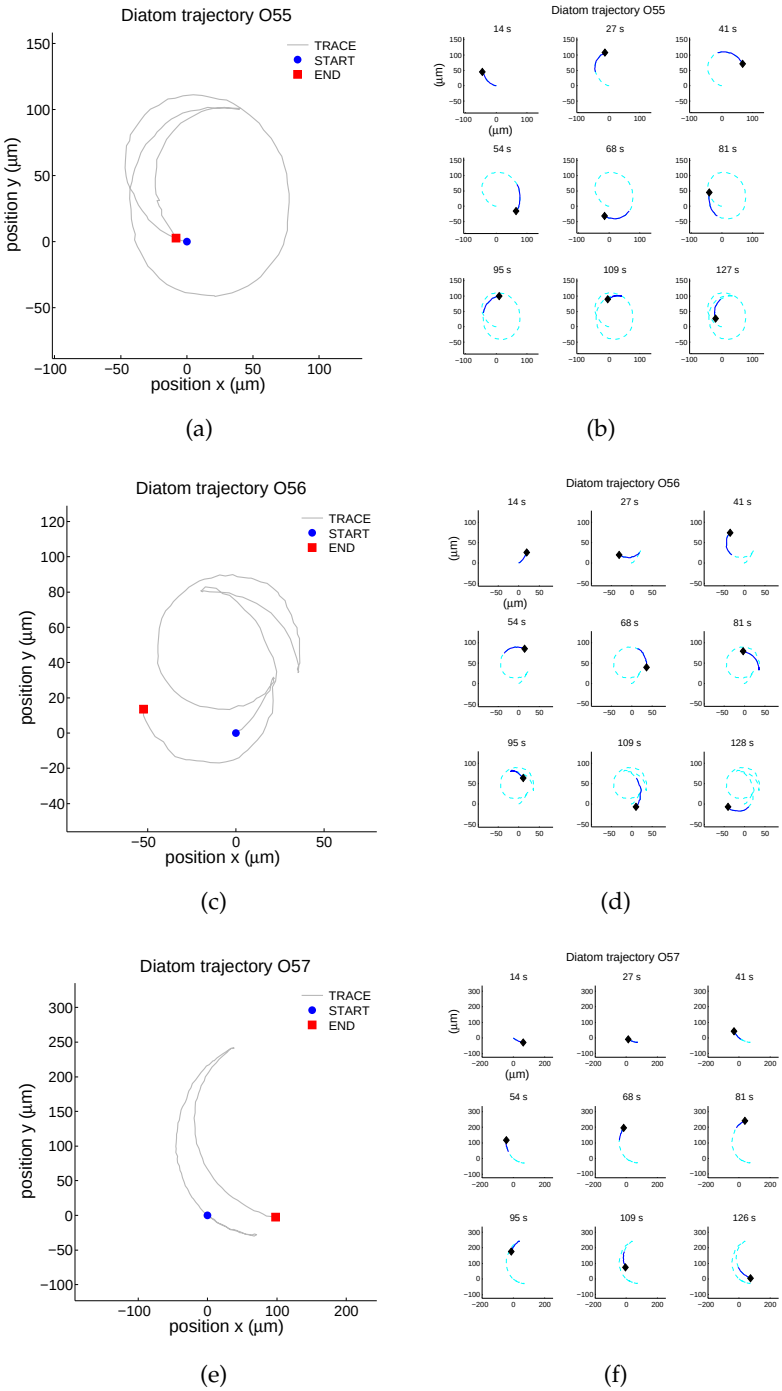

Figure 93: *Nitzschia* sp. diatom trajectories O 55-57. (a, c, e) Trajectory (b,c f) Time-lapsed trajectories.

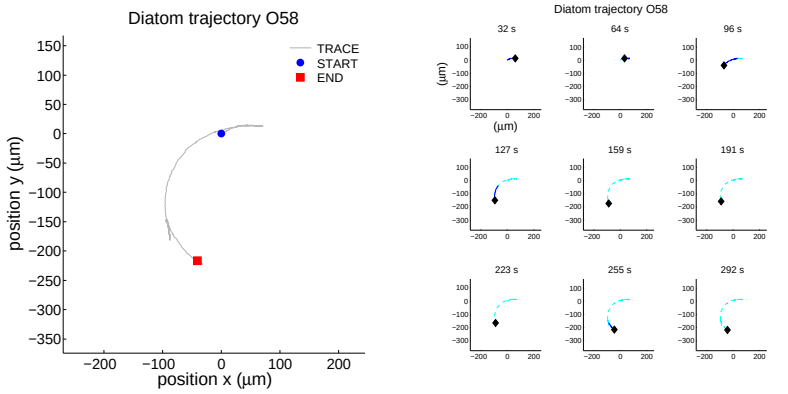

(a) (b)

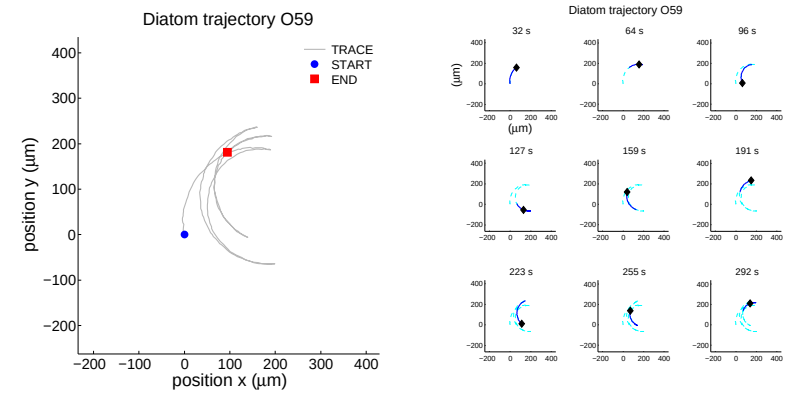

(c) (d)

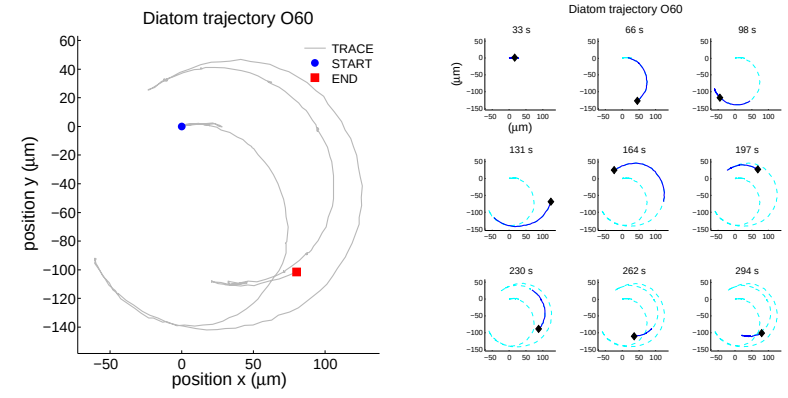

(e) (f)

Figure 94: *Nitzschia* sp. diatom trajectories O 58-60

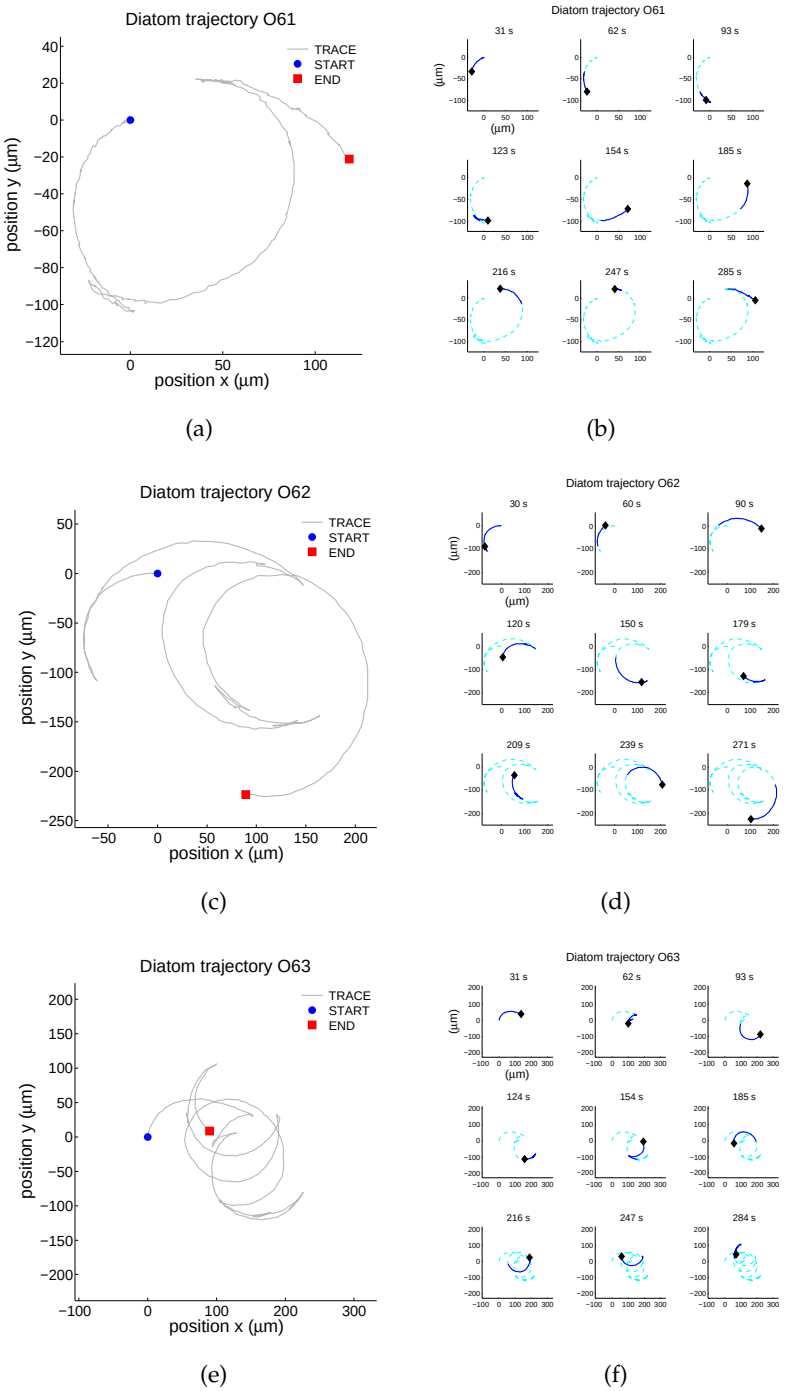

Figure 95: *Nitzschia* sp. diatom trajectories O 61-63. (a, c, e) Trajectory (b,c f) Time-lapsed trajectories.

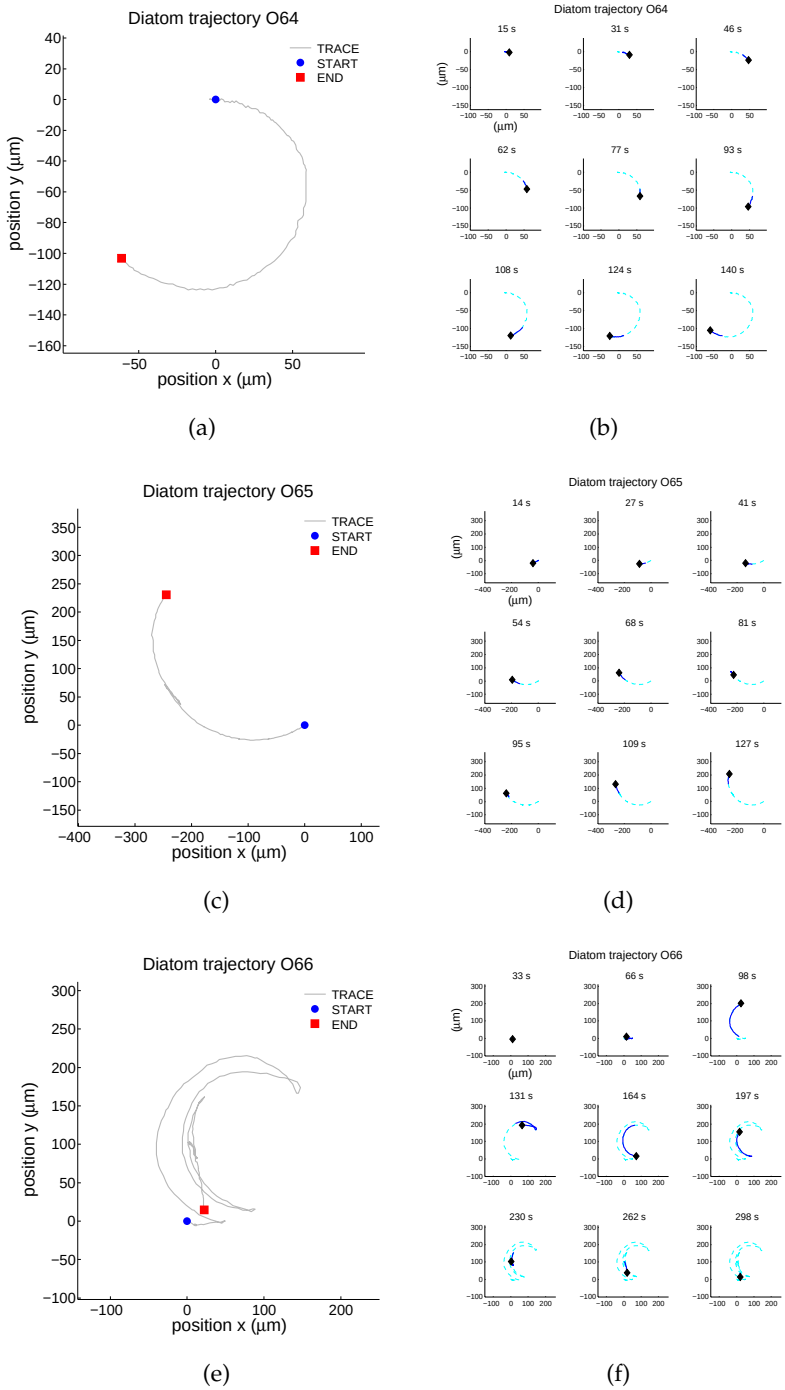

Figure 96: *Nitzschia* sp. diatom trajectories O 64-66

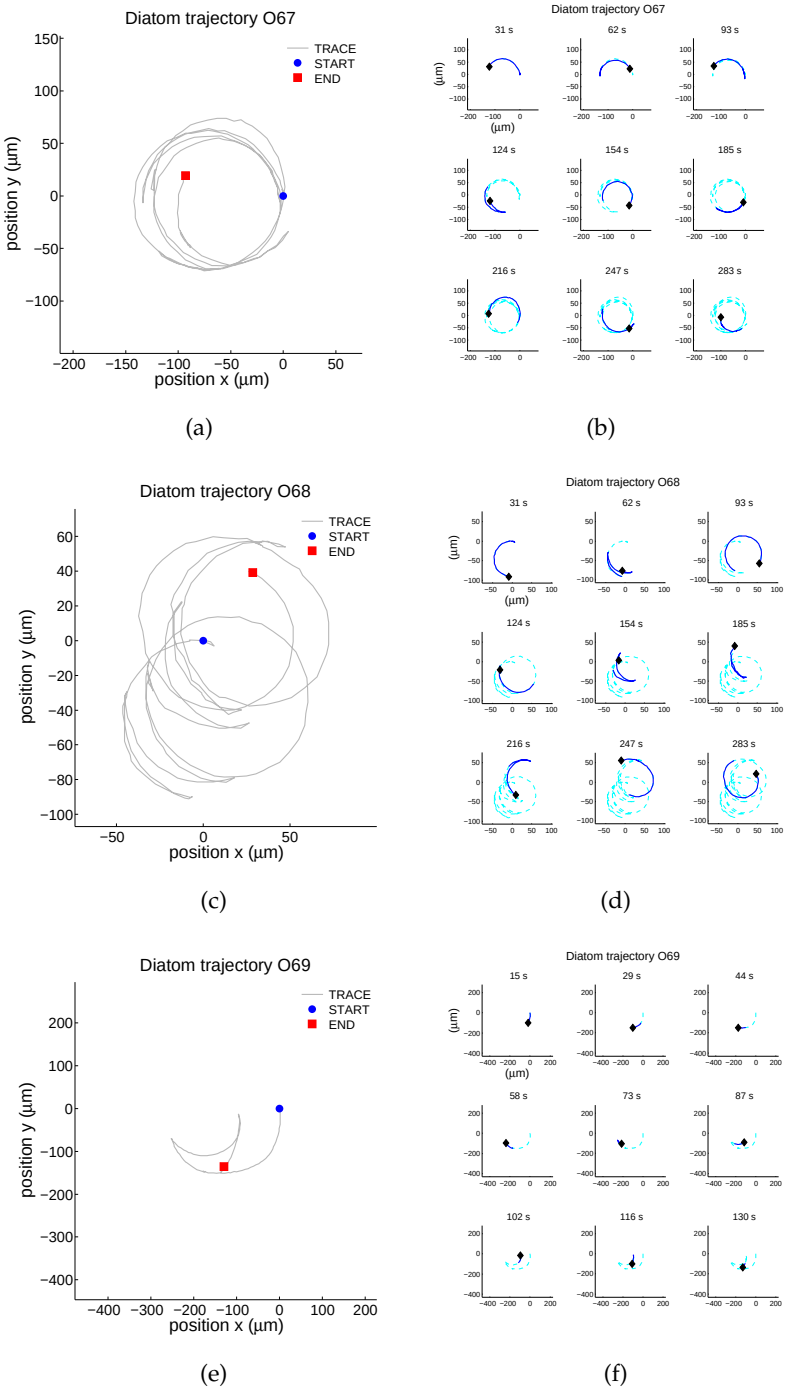

Figure 97: *Nitzschia* sp. diatom trajectories O 67-69. (a, c, e) Trajectory (b,c f) Time-lapsed trajectories.

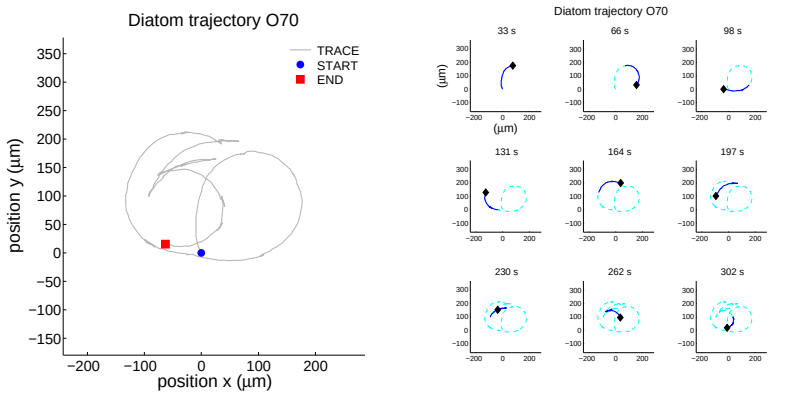

(a) (b)

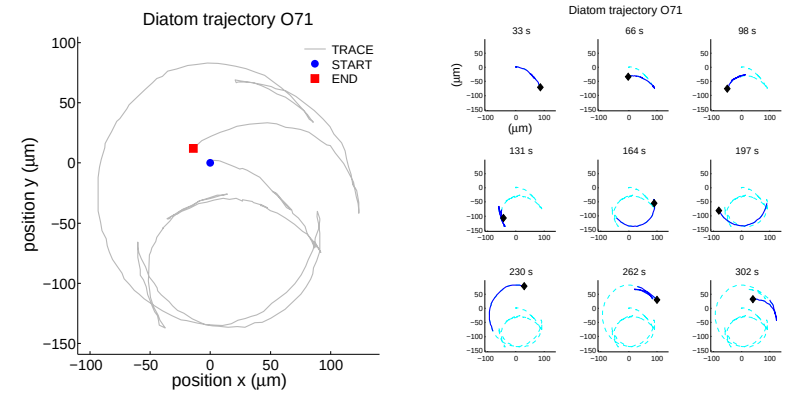

(c) (d)

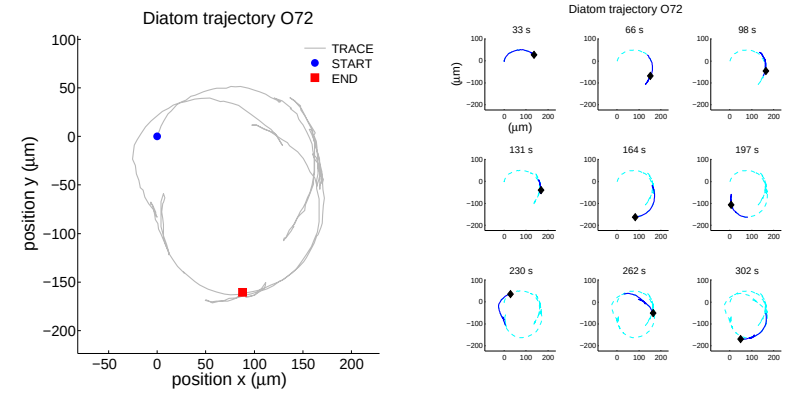

(e) (f)

Figure 98: *Nitzschia* sp. diatom trajectories O 70-72

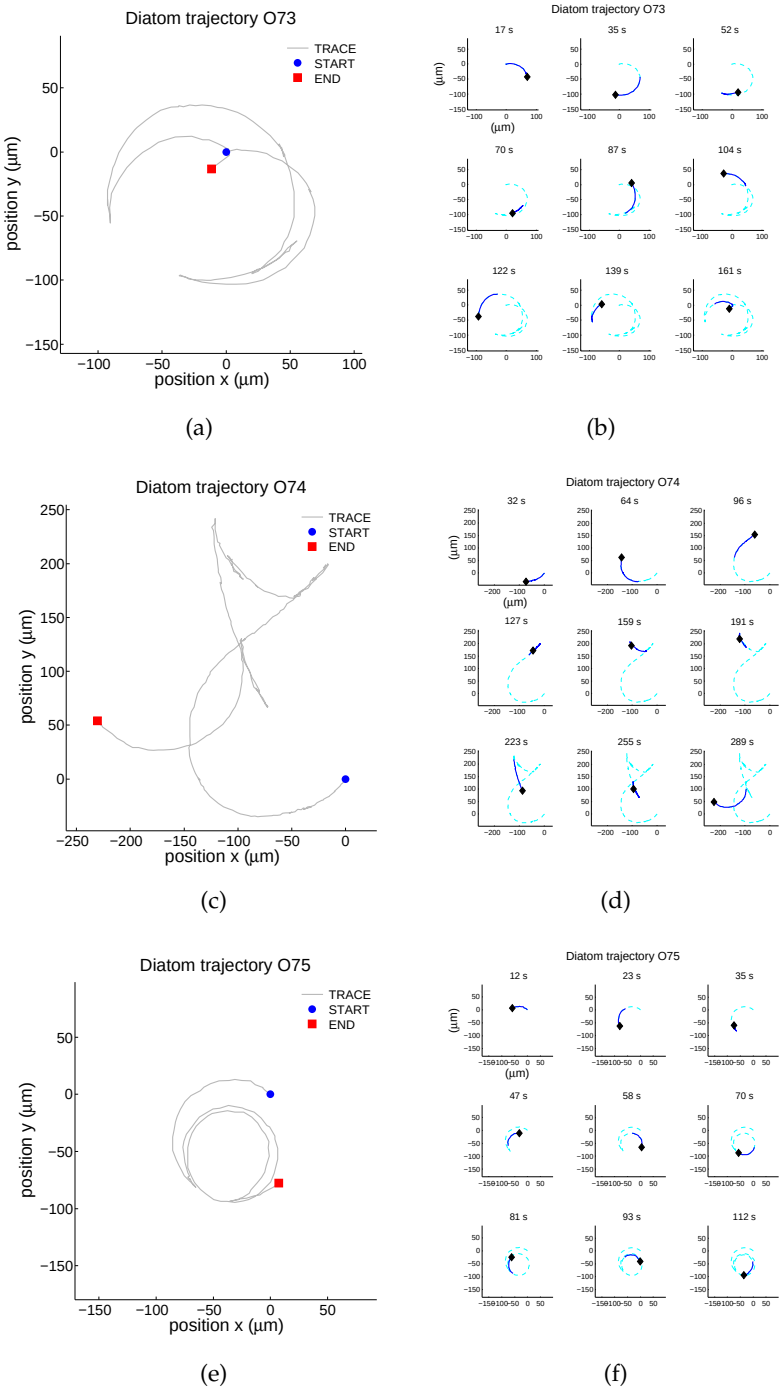

Figure 99: *Nitzschia* sp. diatom trajectories O 73-75. (a, c, e) Trajectory (b,c f) Time-lapsed trajectories.

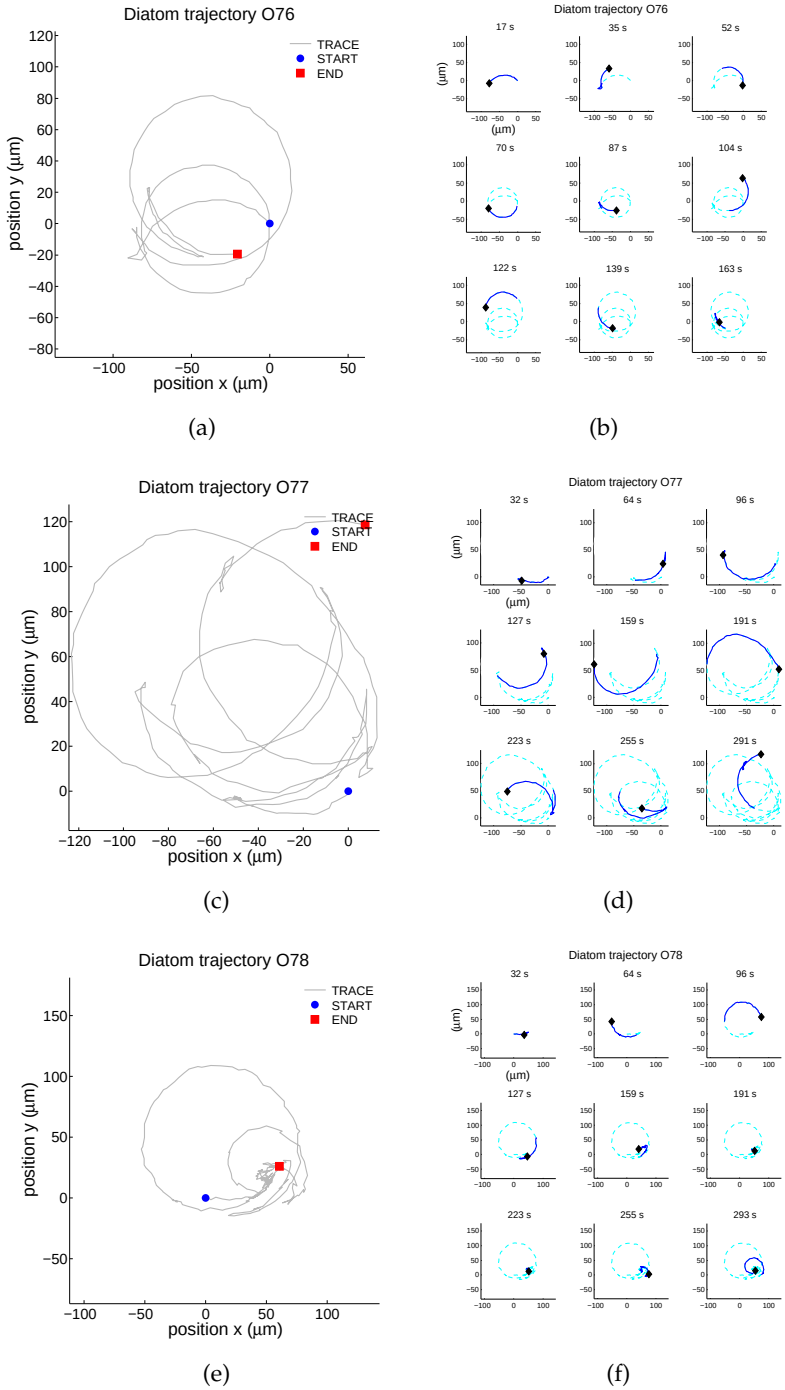

Figure 100: *Nitzschia* sp. diatom trajectories O 76-78

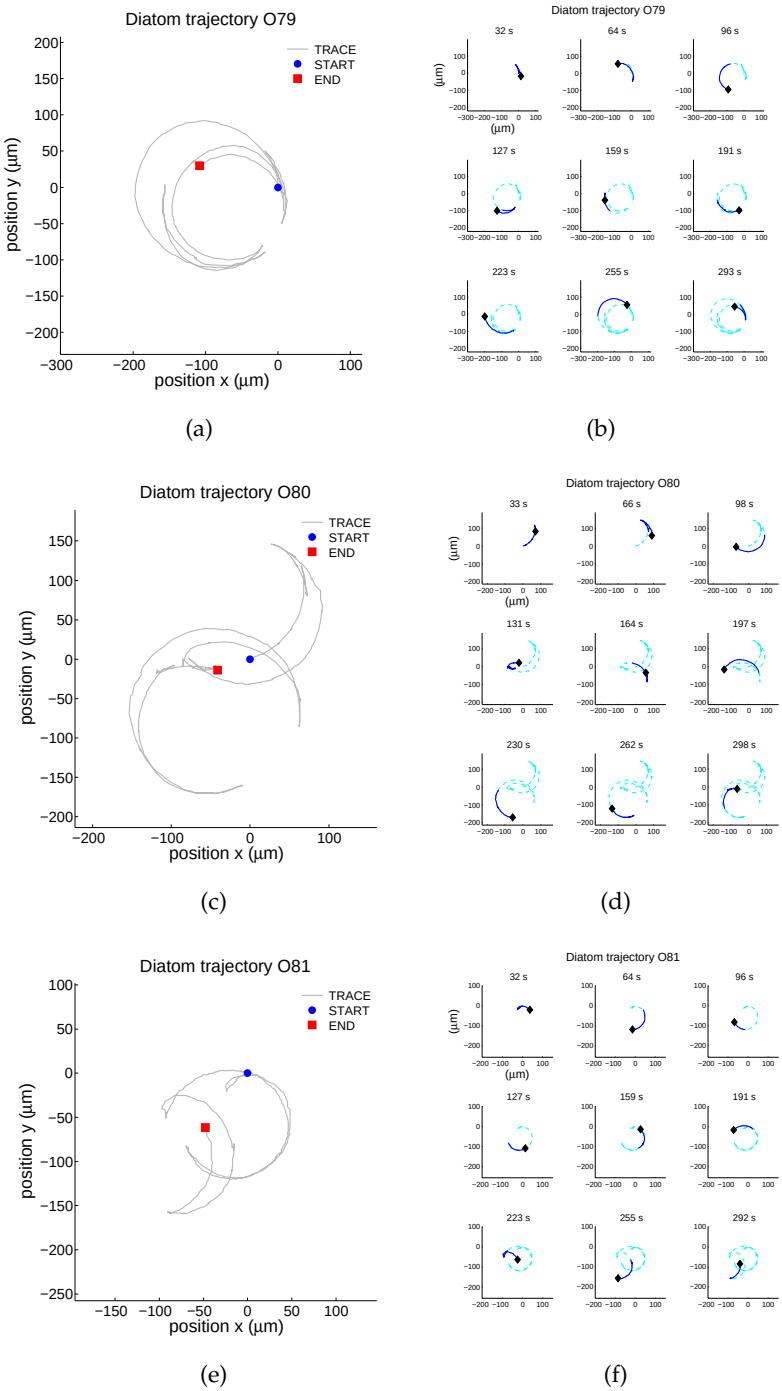

Figure 101: *Nitzschia* sp. diatom trajectories O 79-81. (a, c, e) Trajectory (b,c f) Time-lapsed trajectories.

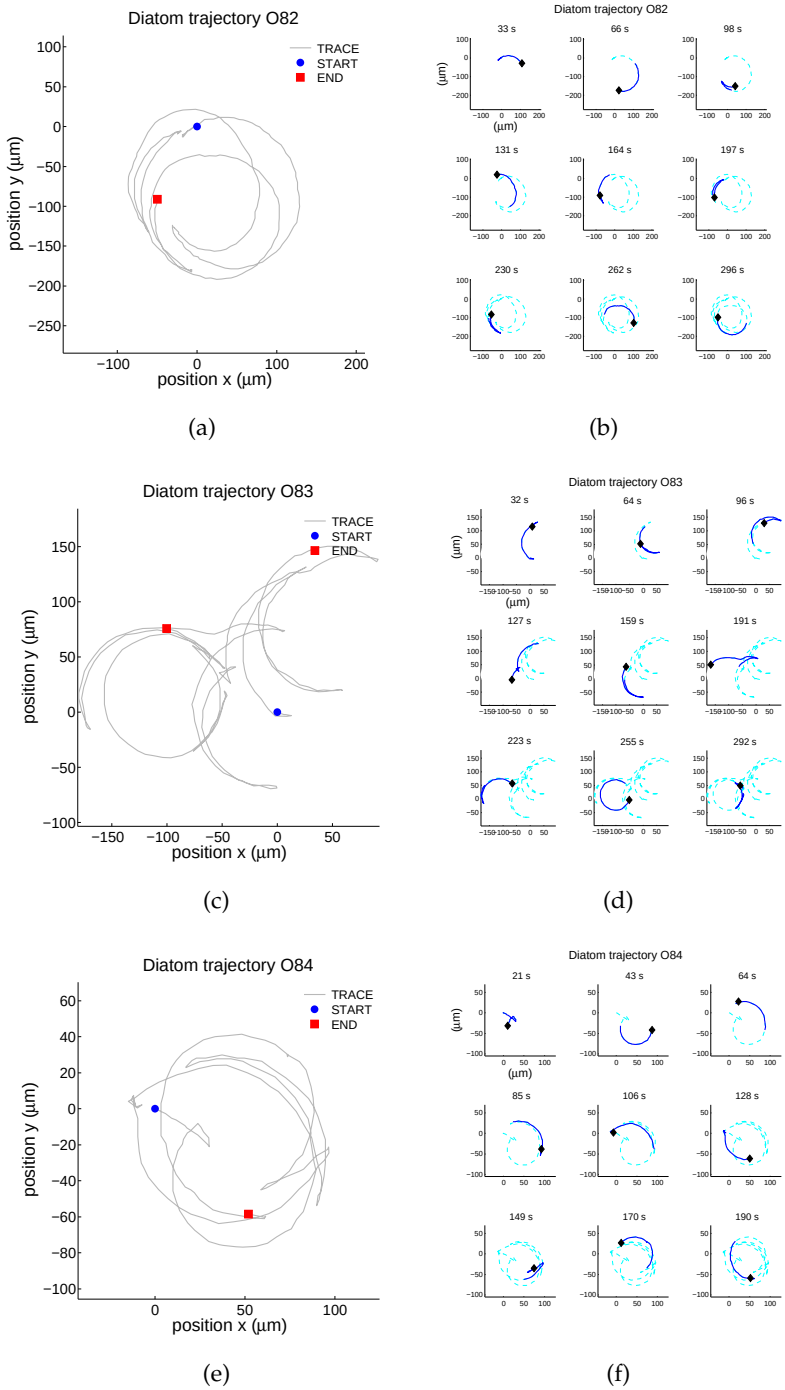

Figure 102: *Nitzschia* sp. diatom trajectories O 82-84

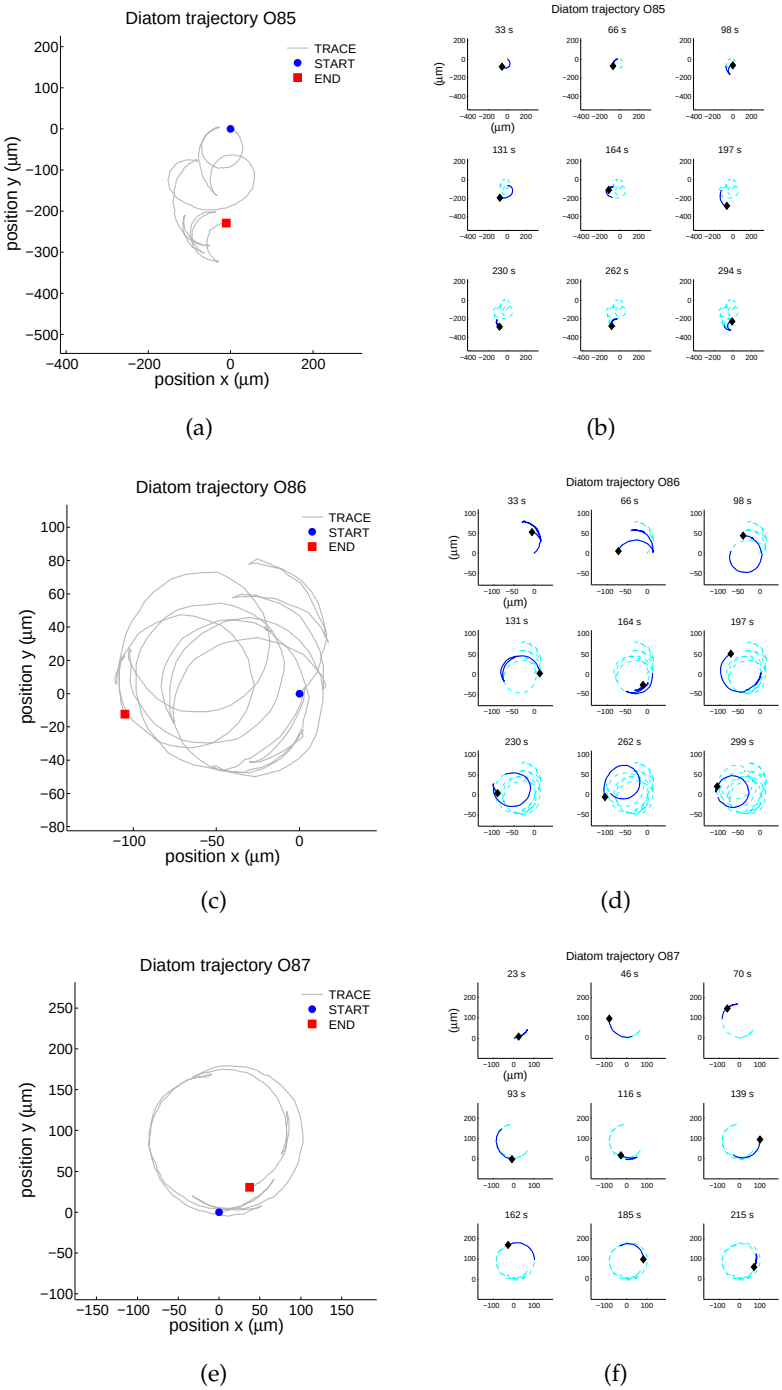

Figure 103: *Nitzschia* sp. diatom trajectories O 85-87. (a, c, e) Trajectory (b,c f) Time-lapsed trajectories.

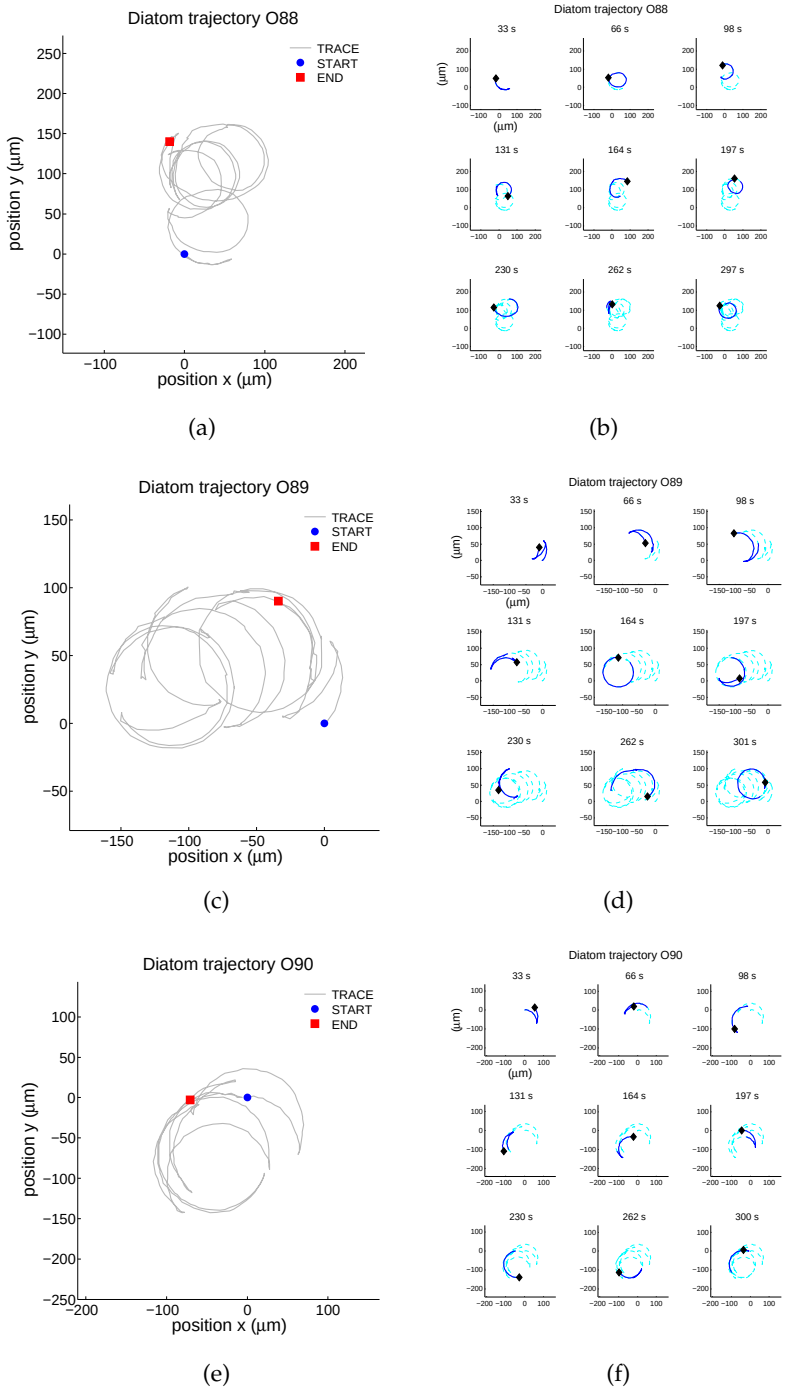

Figure 104: *Nitzschia* sp. diatom trajectories O 88-90

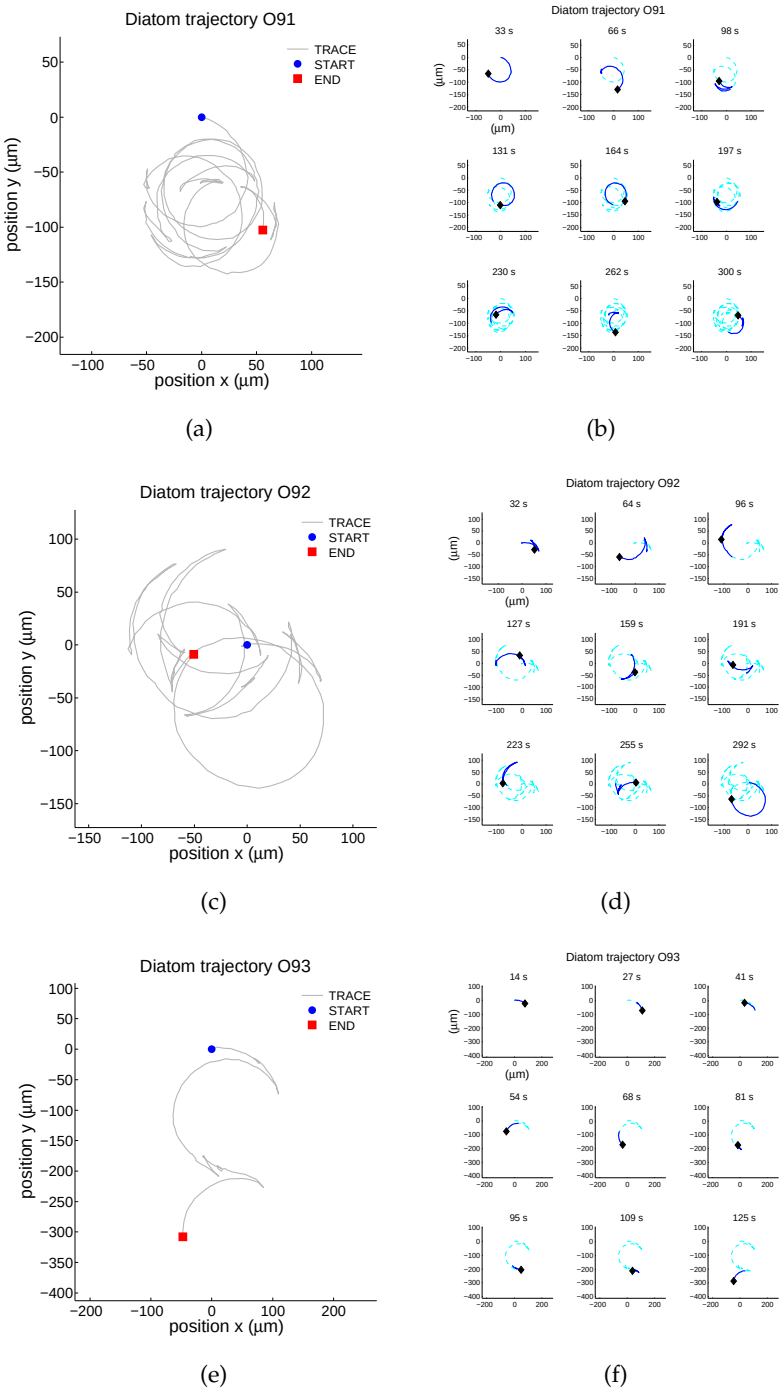

Figure 105: *Nitzschia* sp. diatom trajectories O 91-93. (a, c, e) Trajectory (b,c f) Time-lapsed trajectories.

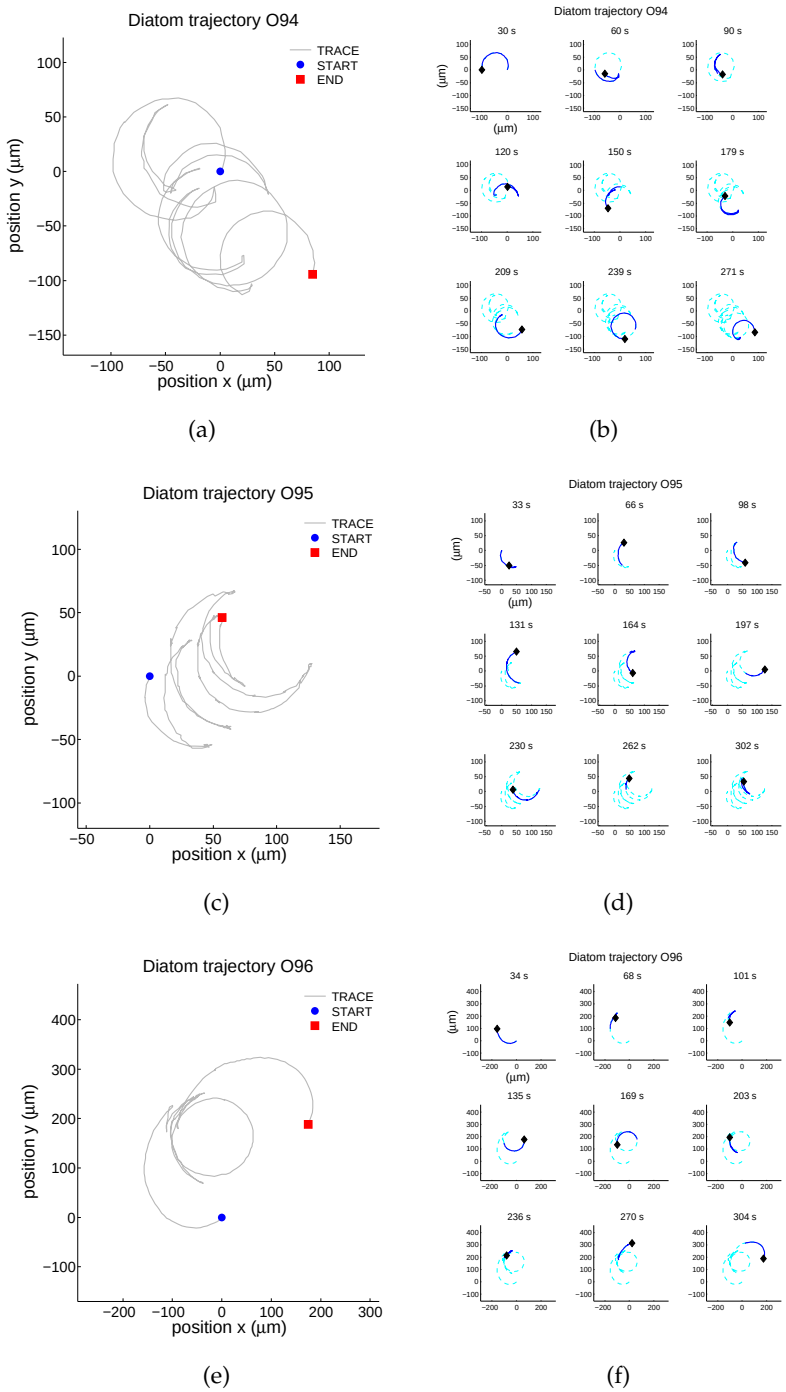

Figure 106: *Nitzschia* sp. diatom trajectories O 94-96

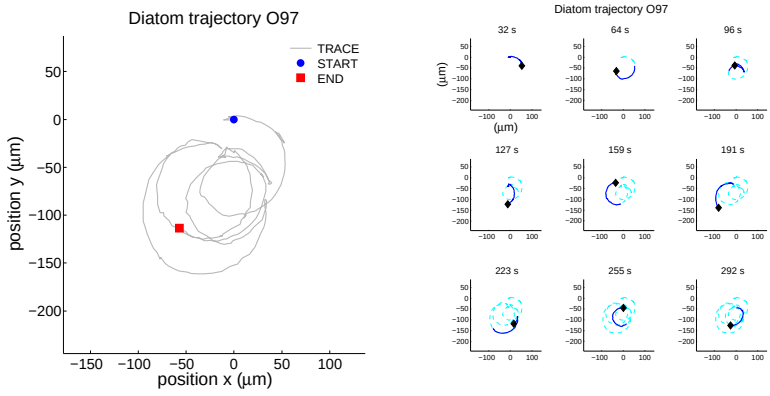

(a) (b)

Figure 107: *Nitzschia* sp. diatom trajectory O 97. (a) Trajectory (b) Time-lapsed trajectory.

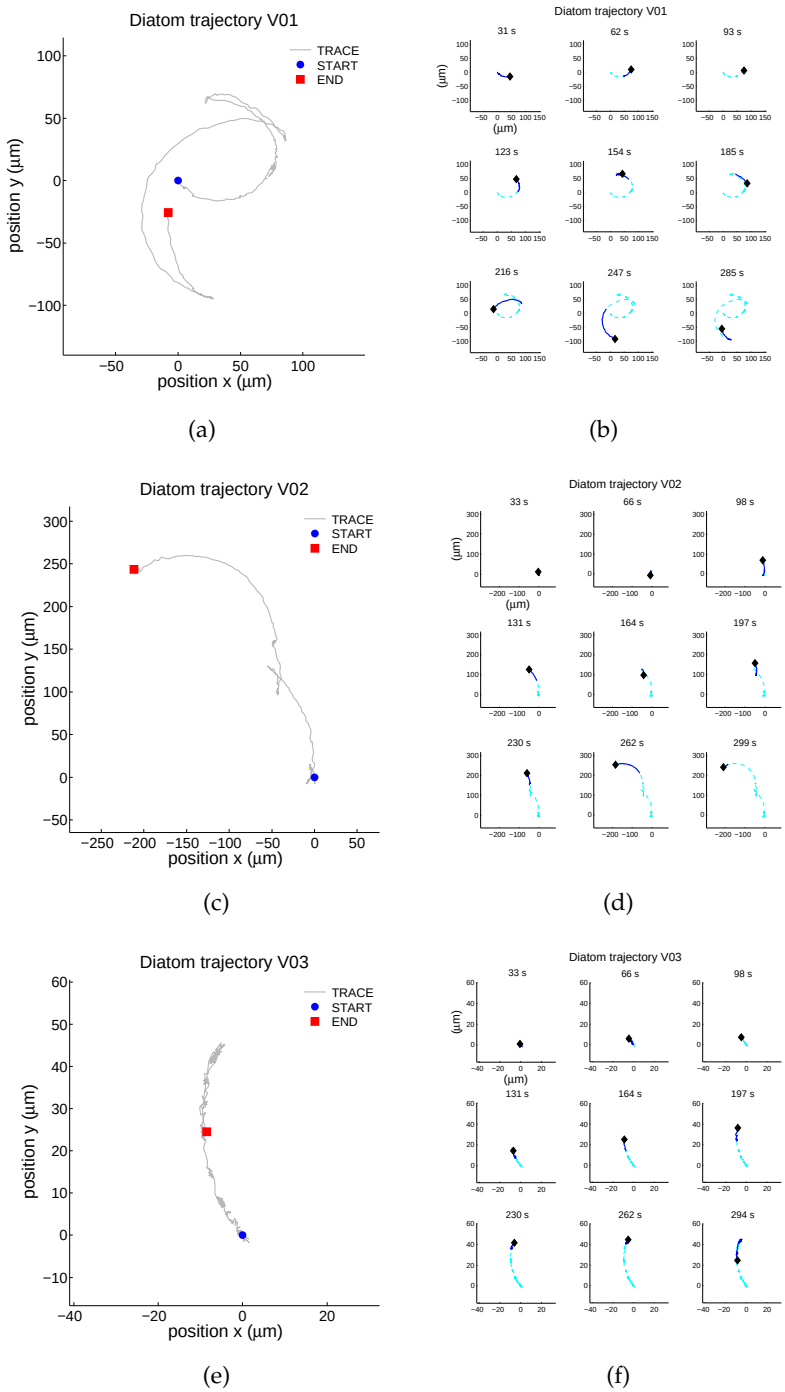

Figure 108: *Nitzschia* sp. diatom trajectories V 1-3

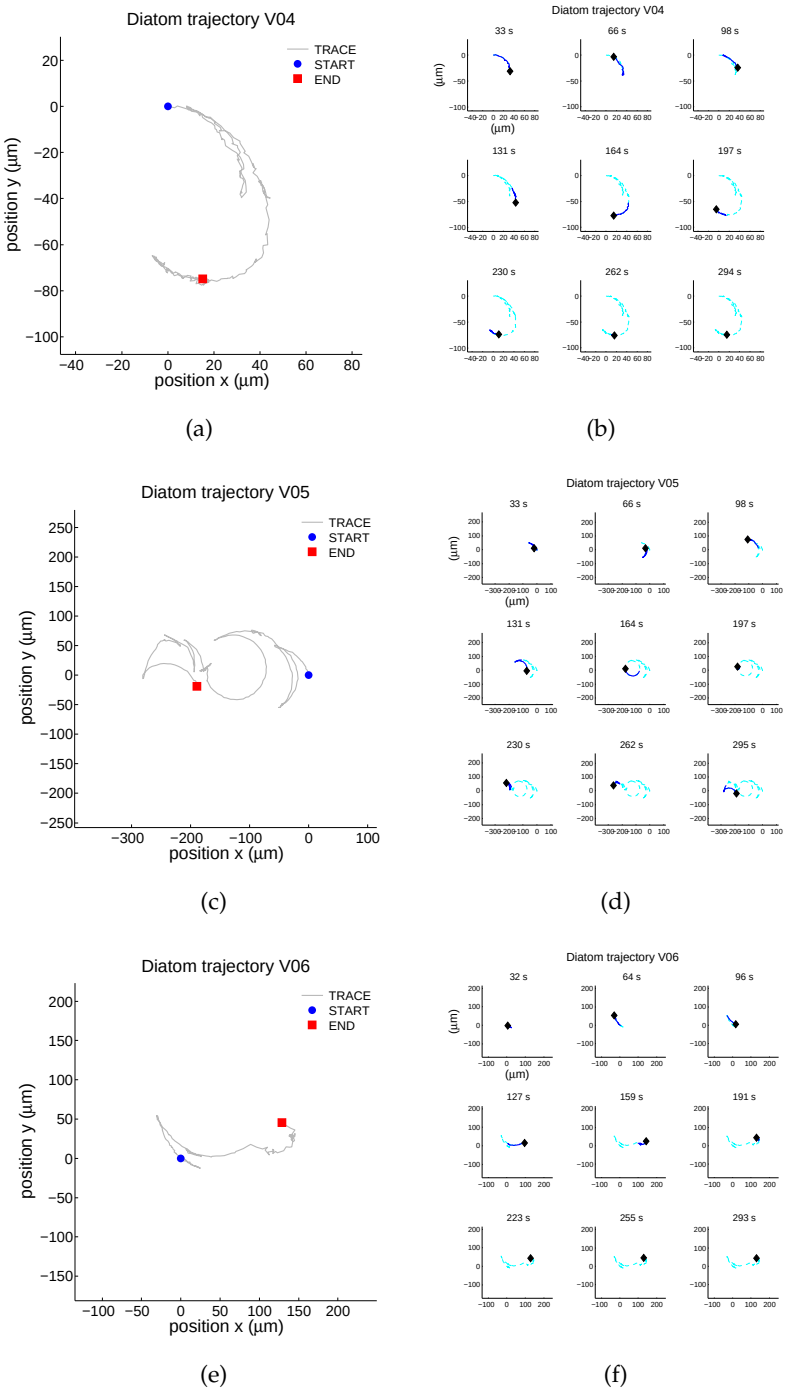

Figure 109: *Nitzschia* sp. diatom trajectories V 4-6. (a, c, e) Trajectory (b,c f) Time-lapsed trajectories.

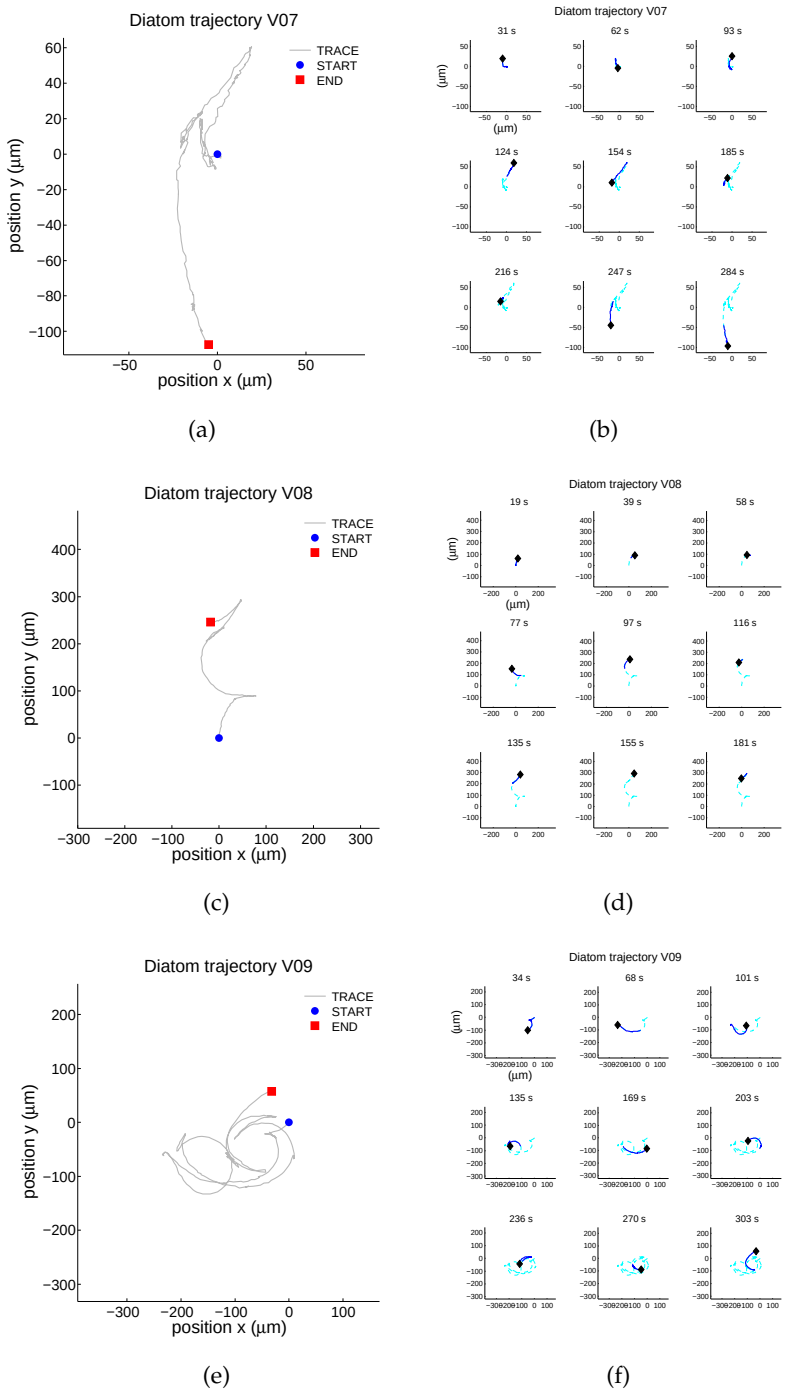

Figure 110: *Nitzschia* sp. diatom trajectories V 7-9

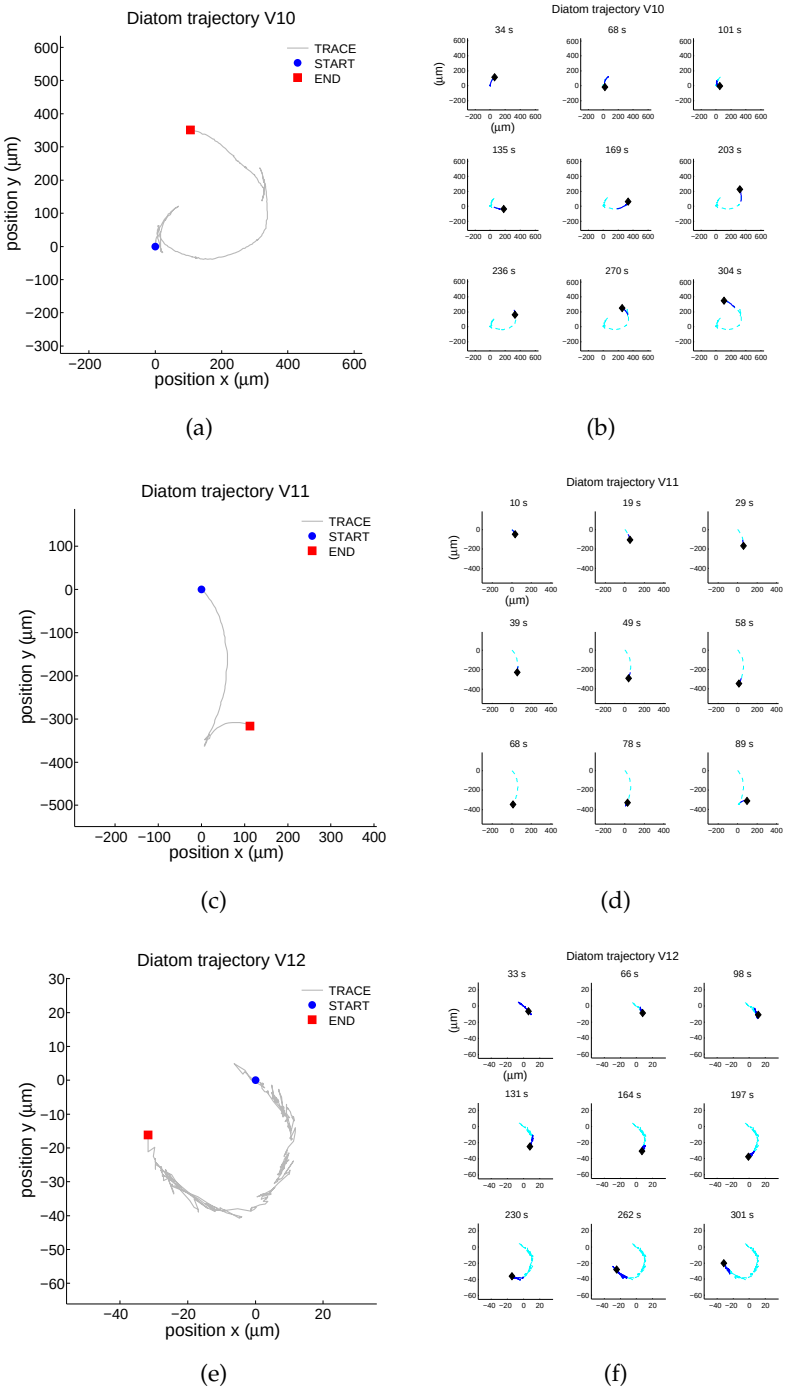

Figure 111: *Nitzschia* sp. diatom trajectories V 10-12. (a, c, e) Trajectory (b,c f) Time-lapsed trajectories.

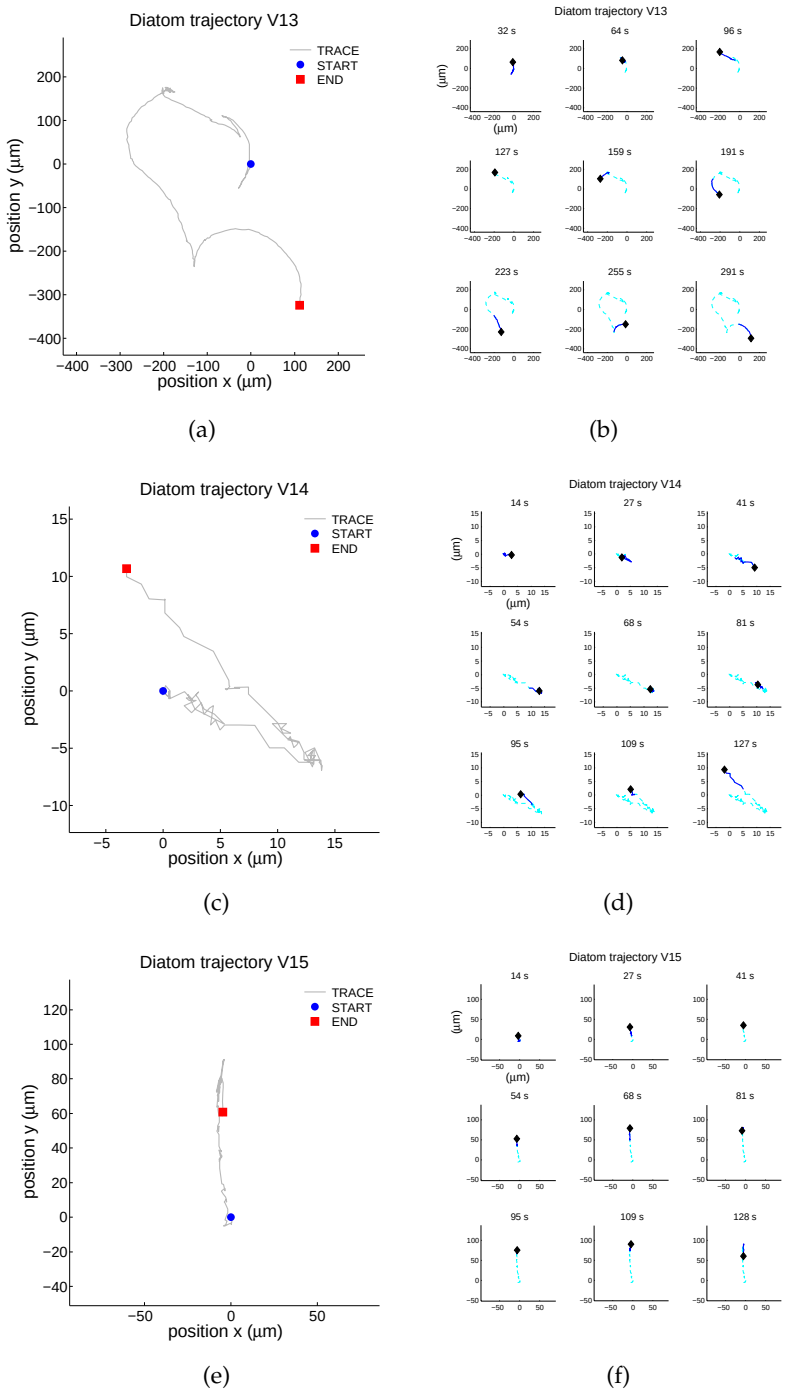

Figure 112: *Nitzschia* sp. diatom trajectories V 13-15

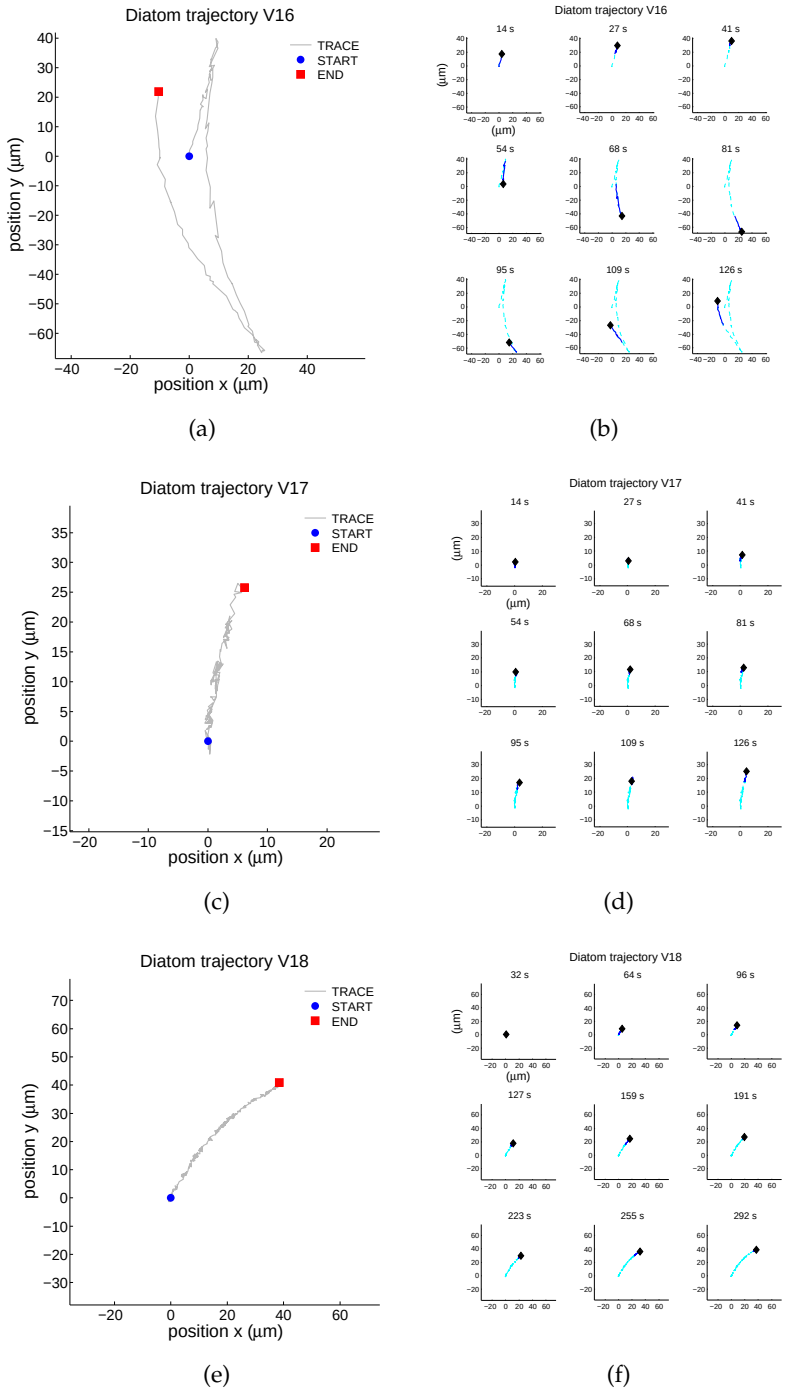

Figure 113: *Nitzschia* sp. diatom trajectories V 16-18. (a, c, e) Trajectory (b,c f) Time-lapsed trajectories.

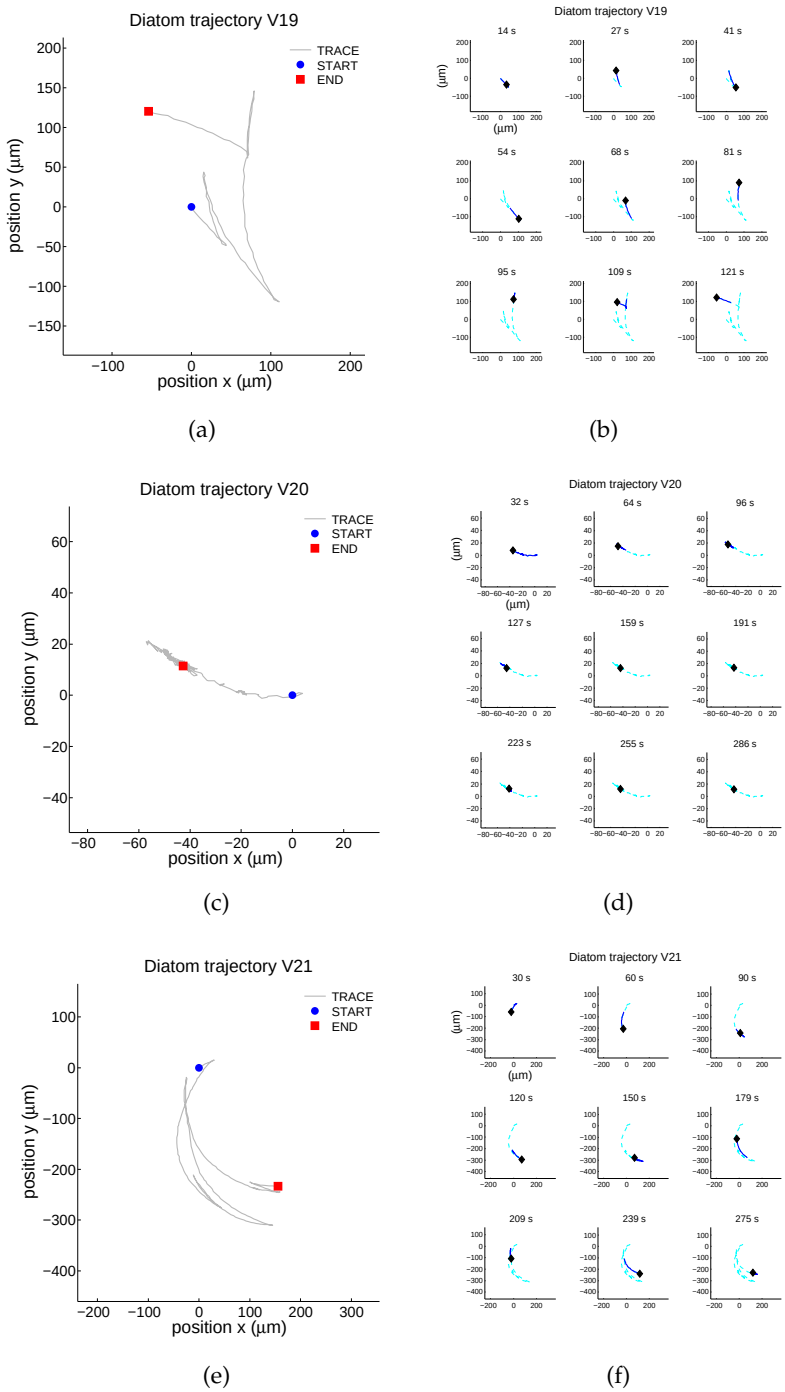

Figure 114: *Nitzschia* sp. diatom trajectories V 19-21

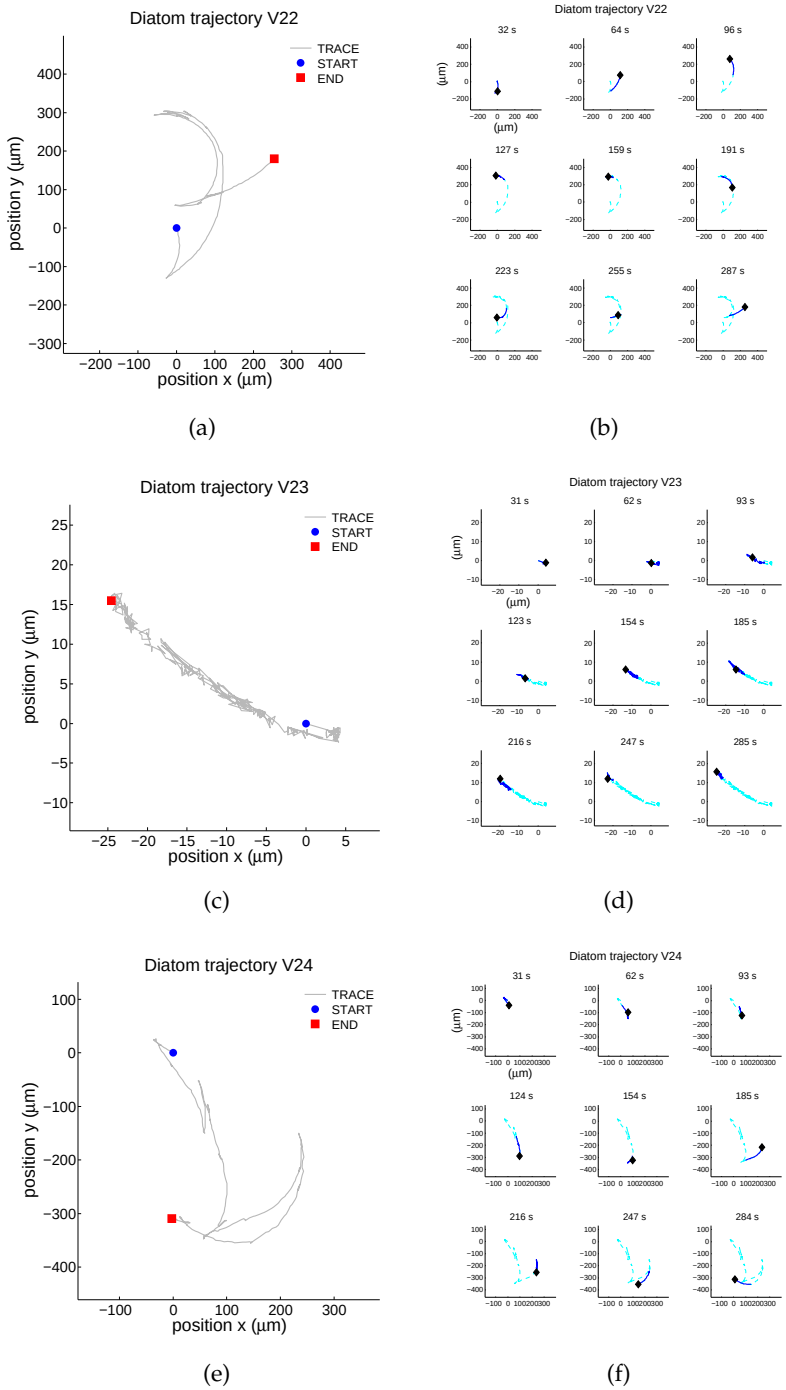

Figure 115: *Nitzschia* sp. diatom trajectories V 22-24. (a, c, e) Trajectory (b,c f) Time-lapsed trajectories.

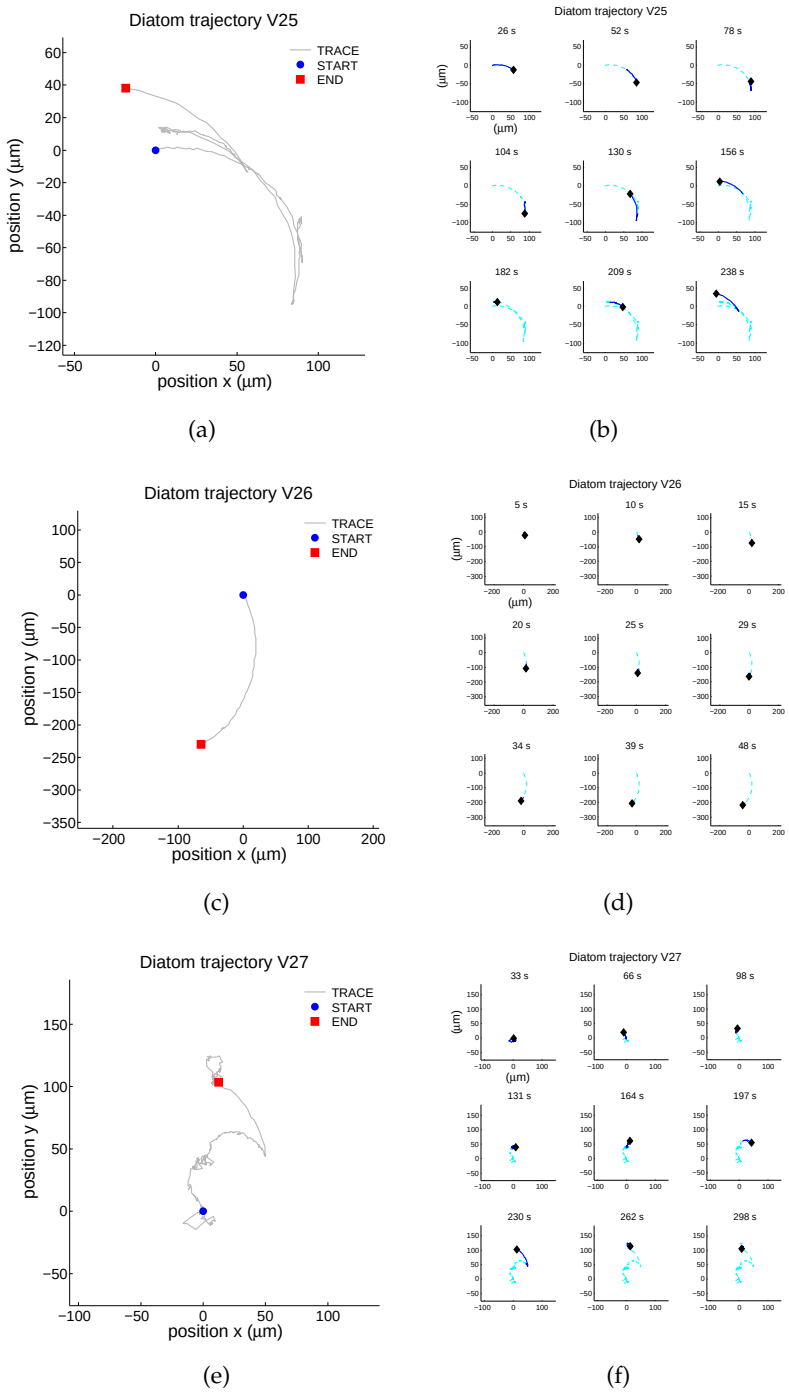

Figure 116: *Nitzschia* sp. diatom trajectories V 25-27

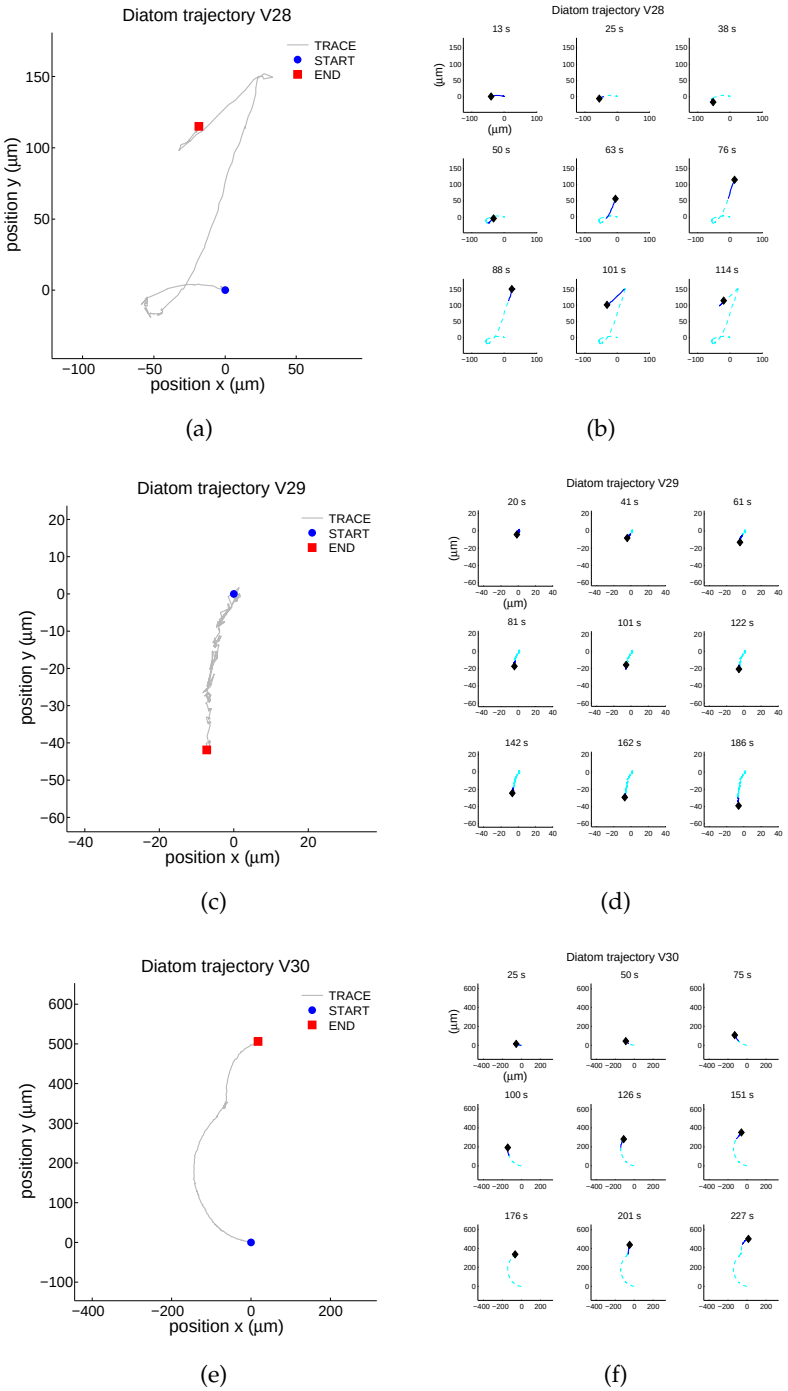

Figure 117: *Nitzschia* sp. diatom trajectories V 28-30. (a, c, e) Trajectory (b,c f) Time-lapsed trajectories.

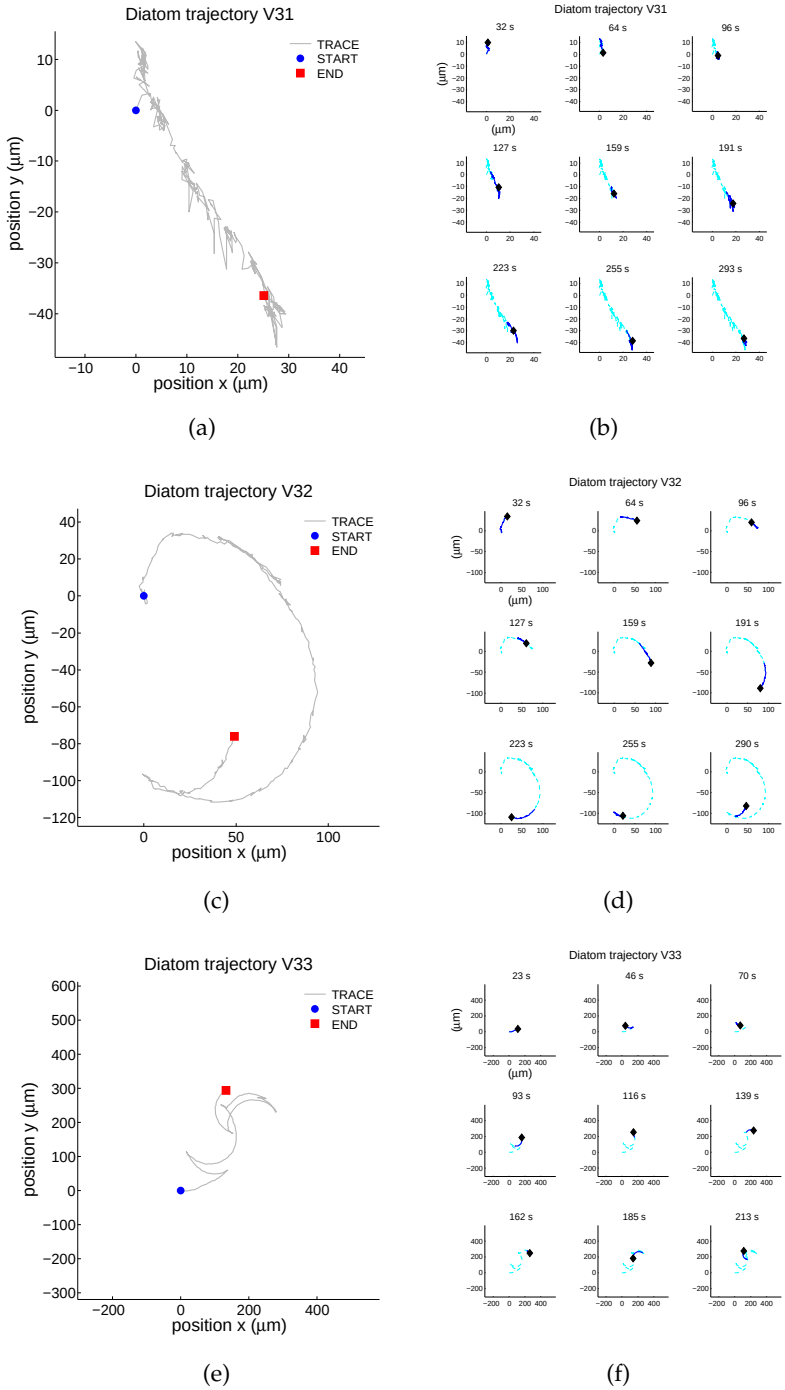

Figure 118: *Nitzschia* sp. diatom trajectories V 31-33

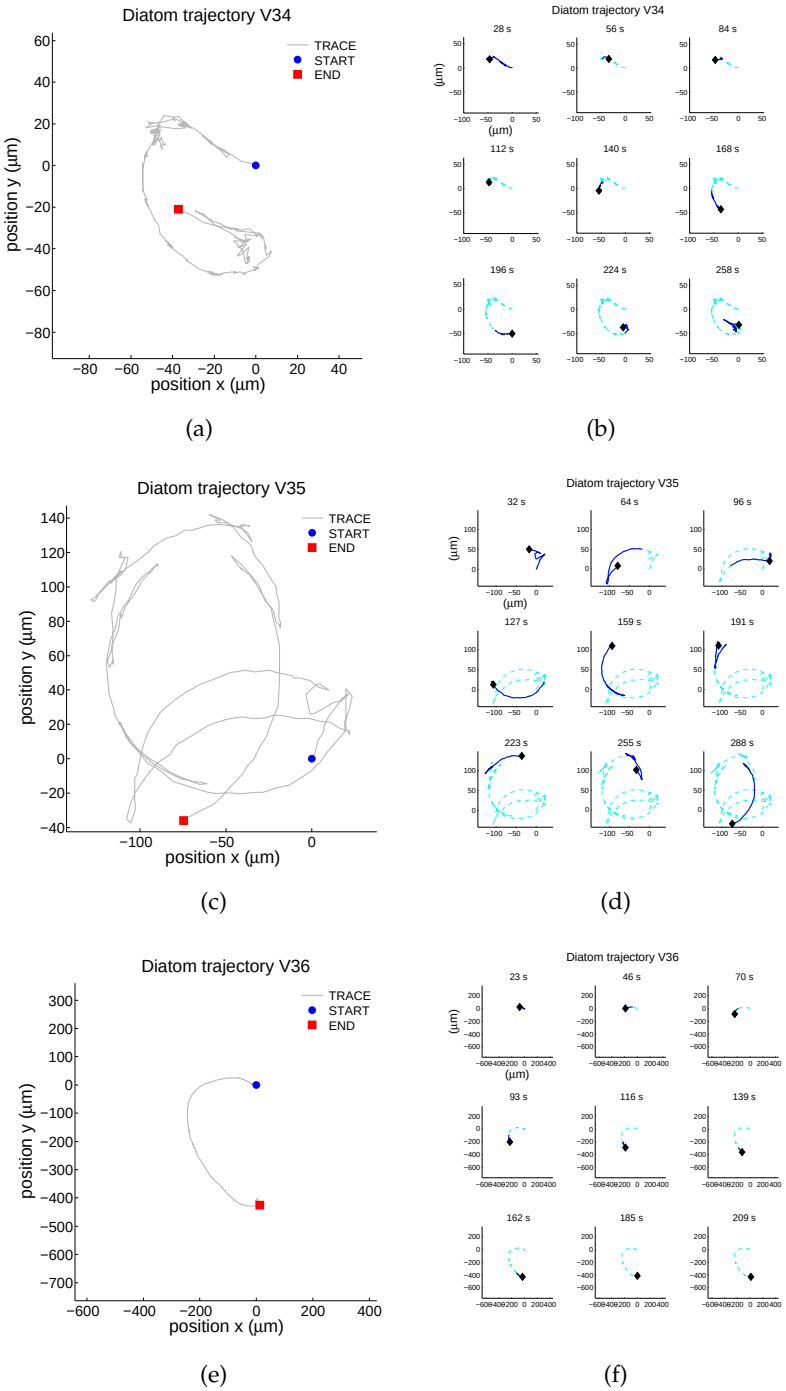

Figure 119: *Nitzschia* sp. diatom trajectories V 34-36. (a, c, e) Trajectory (b,c f) Time-lapsed trajectories.

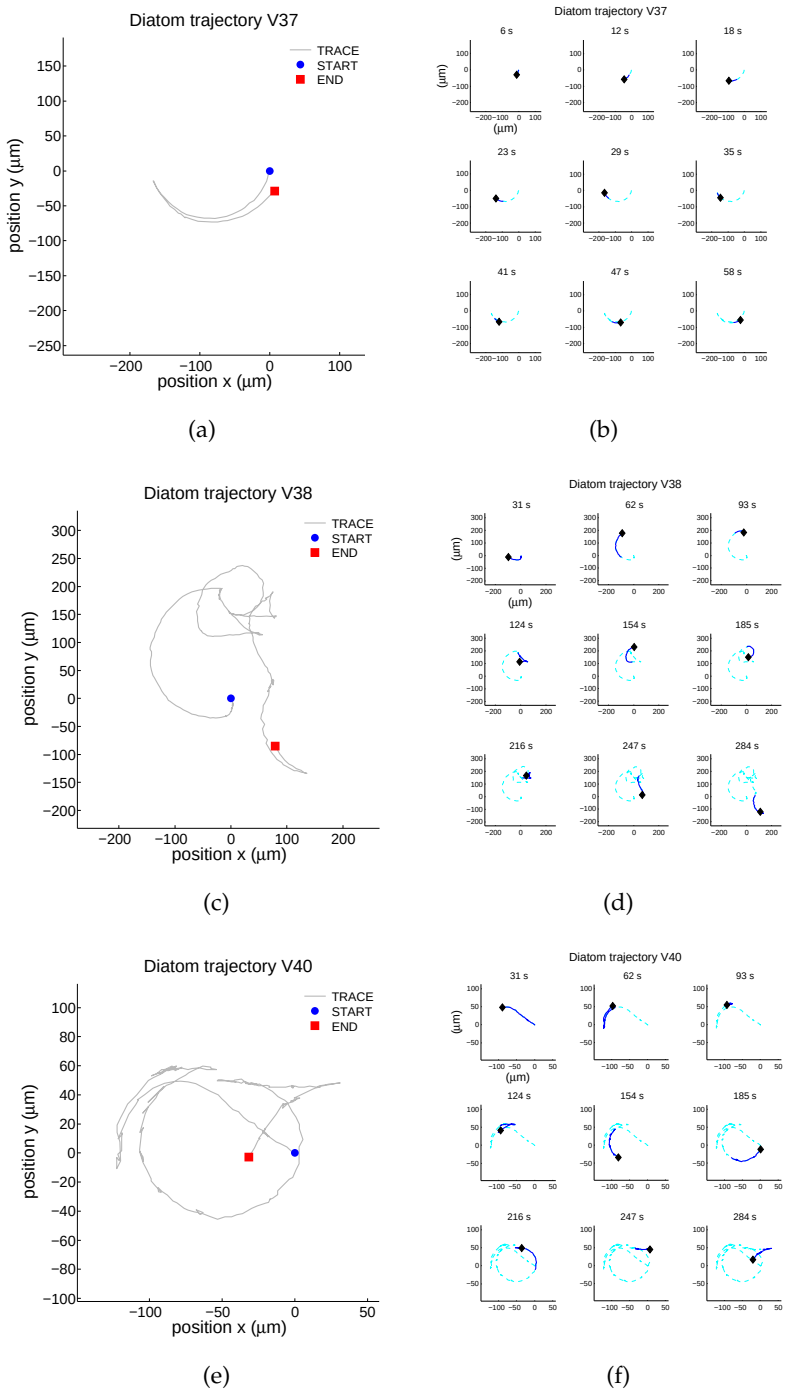

Figure 120: *Nitzschia* sp. diatom trajectories V 37-40

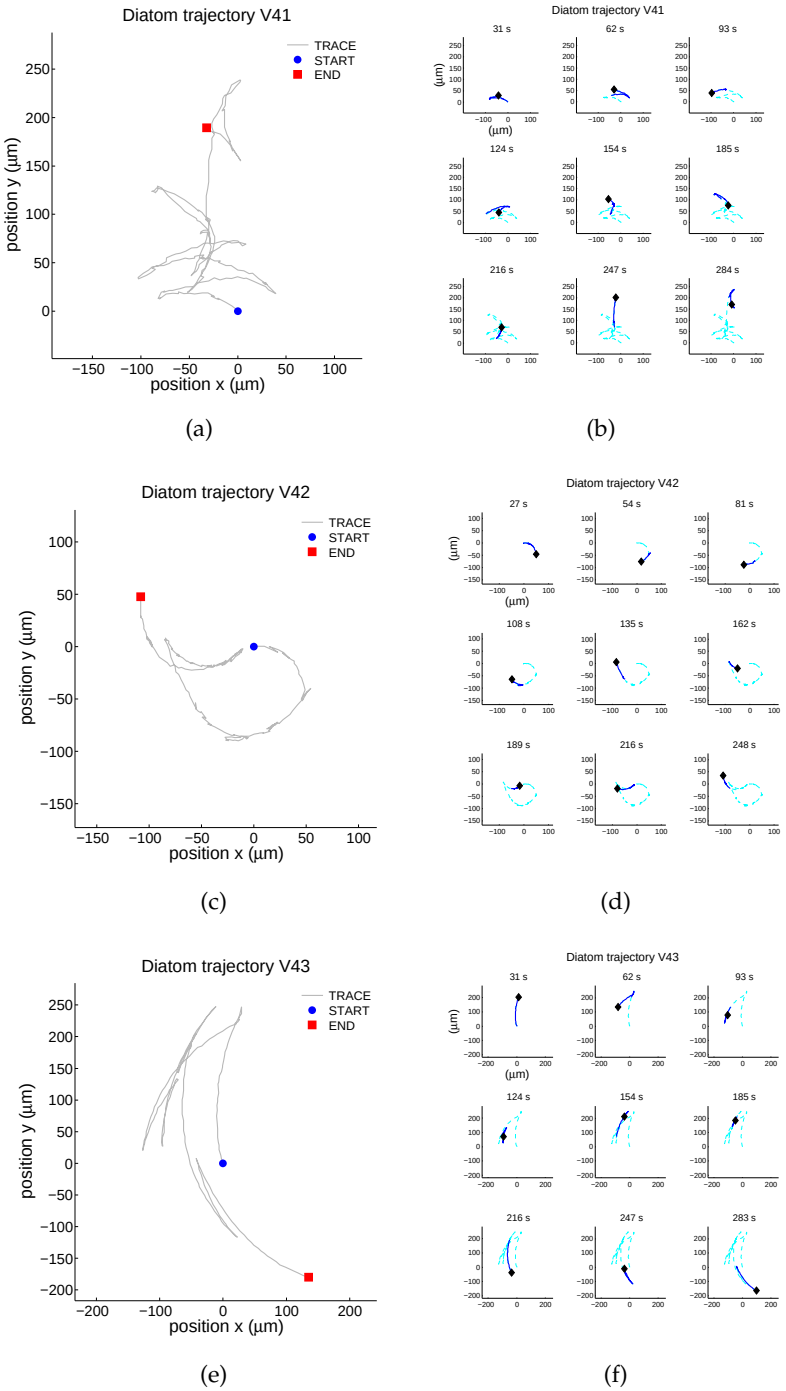

Figure 121: *Nitzschia* sp. diatom trajectories V 41-43. (a, c, e) Trajectory (b,c f) Time-lapsed trajectories.

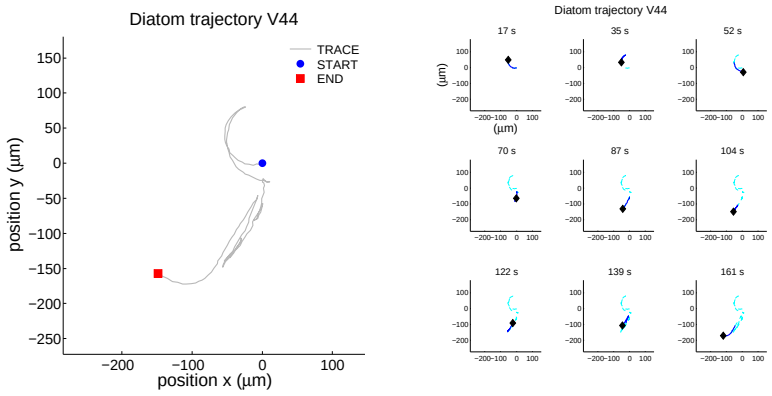

(a) (b)

Figure 122: *Nitzschia* sp. diatom trajectory V 44

BIBLIOGRAPHY

[1] Alessio, E., Carbone, A., Castelli, G., & Frappietro, V. (2002). Second-order moving average and scaling of stochastic time series. *European Physical Journal B*, *27*(197).

[2] Allemand, J. F. (1997). *Micromanipulation d'une molècule individuelle d' ADN*. Ph.D. thesis, Universitè Pierre et Marie Curie, Paris.

[3] Almeida, E., Diamantino, T. C., & de Sousa, O. (2007). Marine paints: the particular case of antifouling paints. *Progress in Organic Coatings*, *59*, 2–20.

[4] Appleyard, D. C., Vandermeulen, K. Y., Lee, H., & Lang, M. J. (2007). Optical trapping for undergraduates. *American Journal of Physics*, *75*(1), 5–14.

[5] Arima, Y., & Iwata, H. (2007). Effect of wettability and surface functional groups on protein adsorption and cell adhesion using well-defined mixed self-assembled monolayers. *Biomaterials*, *28*, 3074–3082.

[6] Armbrust, E. V., Berges, J. A., Bowler, C., Green, B. R., Martinez, D., Putnam, N. H., Zhou, S., Allen, A. E., Apt, K. E., Bechner, M., Brzezinski, M. A., Chaal, B. K., Chiovitti, A., Davis, A. K., Demarest, M. S., Detter, J. C., Glavina, T., Goodstein, D., Hadi, M. Z., Hellsten, U., Hildebrand, M., Jenkins, B. D., Jurka, J., Kapitonov, V. V., Kröger, N., Lau, W. W. Y., Lane, T. W., Larimer, F. W., Lippmeier, J. C., Lucas, S., Medina, M., Montsant, A., Obornik, M., Parker, M. S., Palenik, B., Pazour, G. J., Richardson, P. M., Rynearson, T. A., Saito, M. A., Schwartz, D. C., Thamatrakoln, K., Valentin, K., Vardi, A., Wilkerson, F. P., & Rokhsar, D. S. (2004). The genome of the diatom *Thalassiosira pseudonana*: Ecology, evolution, and metabolism. *Science*, *306*(5693), 79–86.

[7] Banerjee, I., Prangule, R. C., & Kane, R. S. (2011). Antifouling coatings: recent developments in the design of surfaces that prevent fouling by proteins, bacteria, and marine organisms. *Advanced Materials*, *23*, 690–718.

[8] Bao, Z., Weatherspoon, M. R., Shian, S., Cai, Y., Graham, P. D., Shawn M, A., Ahmad, G., Dickerson, M. B., Church, B. C., Kang, Z., Abernathy III, H. W., Summers, C. J., Liu, M., & Sandhage, K. H. (2008). Chemical reduction of three-dimensional silica micro-assemblies into microporous silicon replicas. *Nature*, (446), 172–175.

[9] Beausang, J. F., & Nelson, P. C. (2007). Diffusive hidden Markov model characterization of DNA looping dynamics in tethered particle experiments. *Physical Biology*, *4*(3), 205–219.

[10] Beausang, J. F., Zurla, C., Finzi, L., Sullivan, L., & Nelson, P. C. (2007). Elementary simulation of tethered Brownian motion. *American Journal of Physics*, *75*(6), 520–523.

[11] Bennett, S. M., Finlay, J. A., Gunari, N., Wells, D. D., Meyer, A. E., Walker, G. C., Callow, M. E., Callow, J. A., Bright, F. V., & Detty, M. R. (2010). The role of surface energy and water wettability in aminoalkyl/fluorocarbon/hydrocarbon-modified xerogel surfaces in the control of marine biofouling. *Biofouling*, *26*(2), 235–246.

[12] Blásquez, M. T., Anguiano, M., Arias de Saavedra, F., Lallena, A. M., & Carpena, P. (2009). Aplicación del método "Detrended Fluctuation Analysis" a la trayectoria del centro de presión del cuerpo humano. *Revista Física Médica*, *10*(1), 27–34.

[13] Blumberg, S., Gajraj, A., Pennington, M. W., & Meiners, J.-C. (2005). Three-dimensional characterization of tethered microspheres by total internal reflection flourescence microscopy. *Biophysical Journal*, *89*, 1272–1281.

[14] Botte, V., d'Alcalá, M. R., & Montresor, M. (2013). Hydrodynamic interactions at low reynolds number: an overlooked mechanism favouring diatom encounters. *Journal of Plankton Research*, (pp. 1–5).

[15] Bowler, C., Allen, A. E., Badger, J. H., Grimwood, J., Jabbari, K., Kuo, A., Maheswari, U., Martens, C., Maumus, F., Otillar, R. P., Rayko, E., Salamov, A., Vandepoele, K., Beszteri, B., Gruber, A., Heijde, M., Katinka, M., Mock, T., Valentin, K., Verret, F., Berges, J. A., Brownlee, C., Cadoret, J.-P., Chiovitti, A., Choi, C. J., Coesel, S., de Martino, A., Detter, J. C., Durkin, C., Falciatore, A., Fournet, J., Haruta, M., Huysman, M. J. J., Jenkins, B. D., Jiroutova, K., Jorgensen, R. E., Joubert, Y., Kaplan, A., Kröger, N., Kroth, P. G., La Roche, J., Lindquist, E., Lommer, M., Martin-Jézéquel, V., Lopez, P. J., Lucas, S., Mangogna, M., McGinnis, K., Medlin, L. K., Montsant, A., Secq, M.-P. O.-L., Napoli, C., Obornik, M., Parker, M. S., Petit, J.-L., Porcel, B. M., Poulsen, N., Robison, M., Rychlewski, L., Rynearson, T. A., Schmutz, J., Shapiro, H., Siaut, M., Stanley, M., Sussman, M. R., Taylor, A. R., Vardi, A., von Dassow, P., Vyverman, W., Willis, A., Wyrwicz, L. S., Rokhsar, D. S., Weissenbach, J., Armbrust, E. V., Green, B. R., van de Peer, Y., & Grigoriev, I. V. (2008). The *Phaeodactylum* genome reveals the evolutionary history of diatom genomes. *Nature*, *456*, 239–244.

[16] Brinkers, S., Dietrich, H. R. C., de Groote, F. H., Young, I. T., & Rieger, B. (2009). The persistence length of double stranded DNA determined using dark field tethered particle motion. *Journal of Chemical Physics*, *130*, 215105.

[17] Buldyrev, S. V., Goldberger, A. L., Havlin, S., Mantegna, R. N., Peng, C. K., & Stanley, H. E. (1995). Long-range correlation properties of coding and noncoding DNA sequences: GenBank analysis. *Physical Review E*, *51*(5), 5084–5091.

[18] Bustamante, C., Marko, J. F., Siggia, E. D., & Smith, S. (1994). Entropic elasticity of λ-phage DNA. *Science*, *265*(5178), 1599–1600.

[19] Capra, E. J., & Laub, M. T. (2012). Evolution of two-component signal transduction systems. *Annual Review of Microbiology*, *66*, 325–347.

[20] Cartaxana, P., Brotas, V., & Serôdio, J. (2008). Effects of two motility inhibitors on the photosynthetic activity of the diatoms *Cylindrotheca closterium* and *Pleurosigma angulatum*. *Diatoms Research*, *23*(1), 65–74.

[21] Chiovitti, A., Dugdale, T. M., & Wetherbee, R. (2006). Diatom Adhesives: Molecular and Mechanical Properties. In A. M. Smith, & J. A. Callow (Eds.) *Biological Adhesives*, (pp. 79–103). Springer-Verlag Berlin Heidelberg.

[22] Chiovitti, A., Heraud, P., Dugdale, T. M., Hodson, O. M., Curtain, R. C. A., Dagastine, R. R., Wood, B. R., & Wetherbee, R. (2008). Divalent cations stabilize the aggregation of sulfated glycoproteins in the adhesive nanofibers of the biofouling diatom *Toxarium undulatum*. *Soft Matter*, *4*(4), 811–820.

[23] Chiovitti, A., Higgins, M. J., Harper, R. E., & Wetherbee, R. (2003). The complex polysaccharides of the raphid diatom *Pinnularia viridis* (Bacillariophyceae). *Journal of Phycology*, *39*, 543–554.

[24] Cohn, S. A., & Weitzell Jr., R. E. (1996). Ecological considerations of diatom cell motility I. Characterization of motility and adhesion in four diatom species. *Journal of Phycology*, *32*, 928–939.

[25] Cooksey, K. E., & Wigglesworth-Cooksey, B. (1995). Adhesion of bacteria and diatoms to surfaces in the seas: a review. *Aquatic Microbial Ecology*, *9*, 87–96.

[26] Couillard, M., & Davison, M. (2005). A comment on measuring the Hurst exponent of financial time series. *Physica A: Statistical Mechanics and its Applications*, *348*(0), 404–418.

[27] Crawford, S. A., Higgins, M. J., Mulvaney, P., & Wetherbee, R. (2001). Nanostructure of the diatom frustule as revealed by atomic force and scanning electron microscopy. *Journal of Phycology*, *37*, 543–554.

[28] Daubechies, I. (1992). Ten Lectures on Wavelets. In *CBMS-NSF Lecture Notes nr. 61*. Philadelphia, PA: SIAM.

[29] de Brouwer, J. F. C., & Stal, L. J. (2002). Daily fluctuations of exopolymers in cultures of the benthic diatoms *Cylindrotheca closterium* and *Nitzschia* sp. (Bacillariophyceae). *Journal of Phycology*, *38*, 464–472.

[30] Delignières, D., Fortes, M., & Ninot, G. (2004). The fractal dynamics of self-esteem and physical self. *Nonlinear Dynamics in Psichology and Life Science*, *8*, 479–510.

[31] Delignières, D., & Marmelat, V. (2013). Theoretical and methodological issues in serial correlation analysis. *Advances in Experimental Medicine and Biology*, (782), 127–148.

[32] Delignières, D., Ramdani, S., Lemoine, L., Torre, K., Fortes, M., & Ninot, G. (2006). Fractal analyses for short time series: A re-assessment of classical methods. *Journal of Mathematical psichology*, *50*, 525–544.

[33] Dieker, T. (2004). *Simulation of Fractional Brownian Motion*. Master's thesis, University of Twente, The Nederlands.

[34] Diensthuber, R. P., Bommer, M., Gleichmann, T., & Möglich, A. (2013). Full-length structure of a sensor histidine kinase pinpoints coaxial coiled coils as signal transducers and modulators. *Structure*, *21*, 1127–1136.

[35] Dixit, S., Sing-Zocchi, M., Hanne, J., & Zocchi, G. (2005). Mechanics of binding of a single integration-host-factor protein to DNA. *Physical Review Letters*, *94*(11), 118101–1181014.

[36] Dobrowolski, J. M., Carruthers, V. B., & Sibley, L. D. (1997). Participation of myosin in gliding motility and host cell invasion by *Toxoplasma gondii*. *Molecular Microbiology*, *26*(1), 163–173.

[37] Domozych, D. S., Kort, S., Benton, S., & Yu, T. (2005). The extracellular polymeric substance of the green alga *Penium margaritaceum* and its role in biofilm formation. *Biofilms*, *2*, 129–144.

[38] Drum, R. W., & Hopkins, J. T. (1966). Diatom locomotion: an explanation. *Protoplasma*, *62*, 1–33.

[39] Dugdale, T., Dagastine, R., Chiovitti, A., Mulvaney, P., & Weatherbee, R. (2005). Single adhesive nanofibers from a live diatom

have the signature fingerprint of modular proteins. *Biophysical Journal*, *89*, 4252–4260.

[40] Dugdale, T., Dagastine, R., Chiovitti, A., & Wetherbee, R. (2006). Diatom adhesive mucilage contains distinct supramolecular assemblies of a single modular protein. *Biophysical Journal*, *90*, 2987–2993.

[41] Dugdale, T. M., Willis, A., & Wetherbee, R. (2006). Adhesive modular proteins occur in the extracellular mucilage of the motile, pennate diatom *Phaeodactylum tricornutum*. *Biophysical Journal*, *90*(L58-L60).

[42] Dunlap, D., Zurla, C., Manzo, C., & Finzi, L. (2011). Probing DNA topology using tethered particle motion. *Methods in Molecular Biology*, *783*, 295–313.

[43] Edgar, L. A. (1979). Diatom locomotion. Computer assisted analysis of cine film. *British Phycology Bulletin*, *14*, 83–101.

[44] Edgar, L. A. (1983). Mucilage secretions of moving diatoms. *Protoplasma*, *118*, 44–48.

[45] Edgar, L. A., & Pickett-Heaps, J. D. (1983). The mechanism of diatom locomotion I. An ultrastructural study of the motility apparatus. *Proceedings of the Royal Society of London. Series B. Biological Sciences*, *218*(1212), 331–343.

[46] Edgar, L. A., & Pickett-Heaps, J. D. (1984). Diatom locomotion. In X. X. Chapman, & F. E. Round (Eds.) *Progress in Phycology Research*, (pp. 48–88). Bristol: Biopress.

[47] Ehrlich, H., Demadis, K. D., Pokrovsky, O. S., & Koutsoukos, P. G. (2010). Modern views on desilicification: biosilica and abiotic silica dissolution in natural and artificial environments. *Chemical Review*, *110*, 4556–4689.

[48] Fan, H.-F. (2012). Real-time single-molecule tethered particle motion experiments reveal the kinetics and mechanisms of Cre-mediated site-specific recombination. *Nucleic Acids Research*, *40*(13), 6208–6222.

[49] Farlow, S. J. (1993). *Partial Differential Equations for Scientists and Engineers*. New York, NY, USA: Dover Publications.

[50] Finlay, J. A., Bennett, S. M., Brewer, L. H., Sokolova, A., Clay, G., Gunari, N., Meyer, A. E., Walker, G. C., Wendt, D. E., Callow, M. E., Callow, J. A., & Detty, M. R. (2010). Barnacle settlement and the adhesion of protein and diatom microfouling to xerogel films with varying surface energy and water wettability. *Biofouling*, *26*(6), 657–666.

[51] Finlay, J. A., Callow, M. E., Ista, L. K., & Callow, J. A. (2002). The influence of surface wettability on the adhesion strength of settled spores of the green alga *Enteromorpha* and the diatom *Amphora*. *Integrative and Comparative Biology*, *42*, 1116–1122.

[52] Finzi, L., & Gelles, J. (1995). Measurements of lactose repressor-mediated loop formation and breakdown in single DNA molecules. *Science*, *267*(5196), 378–380.

[53] Foreman, R., Fiebig, A., & Crosson, S. (2012). The LovK-LovR two-component system is a regulator of the general stress pathway in *Caulobacter crescentus*. *Journal of Bacteriology*, *194*(12), 3038–3049.

[54] Frigeri, L. G., Radabaugh, T. R., Haynes, P. A., & Hildebrand, M. (2006). Identification of proteins from a cell wall fraction of the diatom *Thalassiosira pseudonana*. *Molecular Cellular Proteomics*, *5*, 182–93.

[55] Gao, J., Hu, J., Mao, X., & Perc, M. (2012). Culturomics meets random fractal theory: Insights into long-range correlations of social and natural phenomena over the past two centuries.

[56] Gao, J., Hu, J., Tung, W.-W., Cao, Y., Sarshar, N., & Roychowdhury, V. P. (2006). Assessment of long-range correlation in time series: how to avoid pitfalls. *Physical Review E*, *73*, 016117.

[57] Gebeshuber, I. C., Drack, M., & Scherge, M. (2008). Tribology in biology. *Tribology*, *2*(4), 200–212.

[58] Gebeshuber, I. C., Kindt, J. H., Thompson, J. B., Amo, Y. D., Stachelberger, H., Brzezinski, M. A., Stucky, G. D., Morse, D. E., & Hansma, P. K. (2003). Atomic force microscopy study of living diatoms in ambient conditions. *Journal of Microscopy*, *212*, 292–299.

[59] Gebeshuber, I. C., Stachelberger, H., & Drack, M. (2005). Diatom bionanotribology: Biological surfaces in relative motion: Their design, friction, adhesion, lubrication and wear. *Journal of Nanoscience and Nanotechnology*, *5*, 1–9.

[60] Gebeshuber, I. C., Stachelberger, H., Drack, M., & Franek, F. (2005). Biotribology at the micro- and nanoscale as exemplified by diatoms. In *Proceedings 1st Vienna International Conference Micro- and Nano-Technology*, (pp. 135–140). Vienna, Austria.

[61] Gegner, J. (Ed.) (2013). *Tribology - Fundamentals and Advancements*. Janeza Trdine, Croatia: InTech.

[62] Geim, A. K., Dubonos, S. V., Grigorieva, I. V., Novoselov, K. S., Zhukov, A. A., & Shapoval, S. Y. (2003). Microfabricated adhesive mimicking gecko foot-hair. *Nature Materials*, *2*, 461–463.

[63] Gelles, J., Schnapp, B. J., & Sheetz, M. P. (1988). Tracking kinesin-driven movements with nanometre-scale precision. *Letters to Nature*, *331*(4), 450–453.

[64] Gohar, R., & Rahnejat, H. (2008). *Fundamentals of Tribology*. London, UK: Imperial College Press.

[65] Goldberger, A., Amaral, L. A. N., Hausdorff, J. M., Ivanov, P. C., & Peng, C. K. (2002). Fractal dynamics in physiology, alterations with desease and aging. *Proceedings of the National Academy of Sciences*, *19*(99), 2466–2472.

[66] Gunari, N., Brewer, L. H., Bennett, S. M., Sokolova, A., Kraut, N. D., Finlay, J. A., Meyer, A. E., Walker, G. C., Wendt, D. E., Callow, M. E., & Callow, J. A. (2011). The control of marine biofouling on xerogel surfaces with nanometer-scale topography. *Biofouling*, *27*(2), 137–149.

[67] Gupta, S. (2008). Lecture Series on Digital Voice and Picture Communication. Department of Electronics and Electrical Communication Engg, IIT Kharagpur. http://nptel.iitm.ac.in/video.php?subjectId=117105081 [accessed 2013].

[68] Gupta, S., & Agrawal, S. C. (52). Survival and motility of diatoms *Navicula grimmei* and *Nitzschia palea* affected by some physical and chemical factors. *Folia Microbiology*, *2*(127-134).

[69] Han, L., Lui, B. H., Blumberg, S., Beausang, J. F., Nelson, P. C., & Phillips, R. (2008). Calibration of tethered particle motion experiments. In C. Benham (Ed.) *Mathematics of DNA Structure, Function and Interactions*. New York, NY, USA: Springer.

[70] Harper, M. A., & Harper, J. T. (1967). Measurements of diatom adhesion and their relationship with movement. *British Phycology Bulletin*, *3*, 195–207.

[71] Harper, M. L., Dooris, A., & Paré, P. E. (2009). The fundamentals of biotribology and its application to spine arthroplasty. *SAS Journal*, *3*, 125–132.

[72] Hernández, M. (2010). *Transformada ondeleta continua y discreta y sus aplicaciones*. Instituto Tecnológico de San Luis Potosí.

[73] Higgins, M. J., Crawford, S. A., Mulvaney, P., & Wetherbee, R. (2002). Characterization of the adhesive mucilages secreted by live diatom cells using atomic force microscopy. *Protist*, *153*, 25–38.

[74] Higgins, M. J., Molino, P. J., Mulvaney, P., & Wetherbee, R. (2003). The structure and nanomechanical properties of the adhesive mucilage that mediates diatom-substratum adhesion and motility. *Journal of Phycology*, *39*, 1181–1193.

[75] Higgins, M. J., Sader, J. E., Mulvaney, P., & Wetherbee, R. (2003). Probing the surface of living diatoms with atomic force microscopy: the nanostructure and nanomechanical properties of the mucilage layer. *Journal of Phycology*, *39*, 722–734.

[76] Hodson, O. M., Monty, J. P., Molino, P. J., & Wetherbee, R. (2012). Novel whole cell adhesion assays of three isolates of the fouling diatom *Amphora coffeaeformis* revel diverse responses to sufaces of different wettability. *Biofouling*, *28*(4), 381–393.

[77] Holland, R., Dugdale, T. M., Wetherbee, R., Brennan, A. B., Finlay, J. A., Callow, J. A., & Callow, M. E. (2004). Adhesion and motility of fouling diatoms on a silicone elastomer. *Biofouling*, *20*(6), 323–329.

[78] Hurst, H. (1951). Long term storage capacity of reservoirs. In *Transactions of the American Society of Engineers*, 116, (pp. 770–808).

[79] Ibarra-Junquera, V., Escalante-Minakata, P., Murguía, J. S., & Rosu, H. C. (2006). Inferring mixed-culture growth from total biomass data in a wavelet approach. *Physica A*, *370*, 777–792.

[80] Ihlen, E. A. F. (2012). Introduction to multifractal detrended fluctuation analysis in Matlab. *Frontiers in Physiology*, *3*(141), 1–18.

[81] Jin, R.-H., & Yuan, J.-J. (2011). Learning from biosilica: Nanostructured silicas and their coatings on substrates by programmable approaches. In M. Cavrak (Ed.) *Advances in Biomimetics*, chap. 8, (pp. 159–184). InTech.

[82] Kantelhardt, J., Zschiegner, S., Koscielny-Bunde, E., Bunde, A., Havlin, S., & Stanley, E. (2002). Multifractal detrended fluctuation analysis of nonstationary time series. *Physica A*, *316*(14).

[83] Kellermayer, M. S. Z., Bustamante, C., & Granzier, H. L. (2003). Mechanics and structure of titin oligomers explored with atomic force microscopy. *Biochimica et Biophysica Acta*, *1604*, 105–114.

[84] Kim, D.-H., Chambliss, A. B., & Wirtz, D. (2013). The multi-faceted role of the actin cap in cellular mechanosensation and mechanotransduction. *Soft Matter*, *9*, 5516–5523.

[85] Kofoed, D. (2012). *DNA-Protein Interaction Studied at the Single Molecule Level using Tethered Particle Motion*. Master's thesis, University of Copenhagen. Niels Bohr Institute.

[86] Kröger, N., & Poulsen, N. C. (2008). Diatoms–From cell wall biogenesis to nanotechnology. *Annual Review of Genetics*, *42*, 81–107.

[87] Lebeau, T., Gaudin, P., Moan, R., & Robert, J. M. (2002). A new photobioreactor for continuos marennin production with a marine diatom: influence of the light intensity and the immobilised-cell matrix (alginate beads or agar layer). *Applied Microbiology and Biotechnology*, *59*, 153–159.

[88] Li, Y., Gao, Y. H., Li, X. S., Yang, J. Y., & Que, G. H. (2010). Influence of surface free energy on the adhesion of marine benthic diatom *Nitzchia closterium* MMDL533. *Colloids and Surfaces B: Biointerfaces*, *75*(2), 550–556.

[89] Lind, J. L., Heimann, K., Miller, E. A., van Vliet, C., Hoogenraad, N. J., & Wetherbee, R. (1997). Substratum adhesion and gliding in a diatom are mediated by extracellular proteoglycans. *Planta*, *203*, 213–221.

[90] Linder, A., Colchero, J., Apell, H. J., Marti, O., & Mlynek, J. (1992). Scanning force microscopy of diatom shells. *Ultramicroscopy*, *42*(44), 329–332.

[91] Lokenath, D. (2002). *Wavelet Transforms and Their Applications*. Birkhäuser.

[92] Mallat, S. G. (1998). *A Wavelet Tour of Signal Processing*. San Diego: Academic Press.

[93] Manghli, M., Tardin, C., Baglio, J., Rousseau, P., Salomé, L., & Destainville, N. (2010). Probing DNA conformational changes with high temporal resolution by tethered particle motion. *Physical Biology*, *7*, 046003.

[94] Mitbavkar, S., & Anil, A. C. (2007). Species interactions within a fouling diatom community: roles of nutrients, initial inoculum and competitive strategies. *Biofouling*, *23*, 99–112.

[95] Mizrahi, B., Khoo, X., Chiang, H. H., Sher, K. J., Feldman, R. G., Lee, J.-J., Irusta, S., & Kohane, D. S. (2013). Long-lasting antifouling coating from multi-armed polymer. *Langmuir*, *29*(32), 10087–10094.

[96] Molino, P. J., Hodson, O. M., Quinn, J. F., & Wetherbee, R. (2006). Utilizing QCM-D to characterize the adhesive mucilage secreted by two marine diatom species *in-situ* and in real-time. *Biomacromolecules*, *7*, 3276–3282.

[97] Molino, P. J., Hodson, O. M., Quinn, J. F., & Wetherbee, R. (2008). The quartz crystal microbalance, a new tool for the investigation of the bioadhesion of diatoms to surfaces of differing surface energies. *Langmuir*, *24*, 6730–6737.

[98] Molino, P. J., & Wetherbee, R. (2008). The biology of biofouling diatoms and their role in the development of microbial slimes. *Biofouling*, *24*(5), 365–379.

[99] Moroz, A. L., Ehrman, J. M., Clair, T. A., Gordon, R. J., & Kaczmarska, I. (1999). The impact of ultraviolet-B radiation on the motility of the freshwater epipelic diatom *Nitzschia linearis*. *Global Change Biology*, *5*, 191–199.

[100] Mr. C (1702). Two Letters from a Gentleman in the Country, Relating to Mr Leuwenhoeck's Letter in Transaction, No. 283. Communicated by Mr C. *Philosophical Transactions (1683-1775)*, *23*, 1494–1501.

[101] Murase, A., Kubota, Y., Hirayama, S., Kumashiro, Y., Okano, T., Mayama, S., & Umemura, K. (2011). Two-dimensional analysis of the diatom *Navicula* sp. using a micro chamber. *Journal of Microbiological Methods*, *87*(3), 316–319.

[102] Murguía, J. S., & Rosu, H. C. (2011). Discrete wavelet analyses for time series. In J. T. Olkkonen (Ed.) *Discrete Wavelet Transforms: Theory and Applications*.

[103] Murguía, J. S., & Rosu, H. C. (2012). Multifractal analyses of row sum signals of elementary cellular automata. *Physica A*, (391), 3638–3649.

[104] Murguía, J. S., Rosu, H. C., Pérez-Terrazas, J. E., & Mejía-Carlos, M. (2012). Multifractal analysis of time series from CA by means of the wavelet transform. *Revista Mexicana de Física S*, *58*, 84–90.

[105] Nelson, P. C., Zurla, C., Brogiolo, D., Beausang, J. F., Finzi, L., & Dunlap, D. (2006). Tethered particle motion as a diagnostic of DNA tether length. *Journal of Physical Chemistry B*, *110*(34), 17260–17267.

[106] Nichols, H. W. (1973). Growth media–Freshwater. In J. R. Stein (Ed.) *Handbook of Phycological Methods: Culture Methods and Growth Measurements*, (pp. 7–24). New York, NY, USA: Cambridge University Press.

[107] Peng, C. K., Buldyrev, S., Havlin, S., Simons, M., Stanley, H., & Goldberger, A. (1994). Mosaic organization of DNA nucleotides. *Physical Review E*, *49*(2).

[108] Perazzo, C. A., Fernández, E. A., & Willshaw, P. (2004). Determinación de correlaciones a largo plazo utilizando dfa. In E. Vera de Prayer, C. D'Atellis, R. Armentano, & M. Risk (Eds.)

Procesamiento de Señales e Imágenes: Teoría y Aplicaciones, (pp. 297–312). Facultad Regional Buenos Aires, Universidad Tecnológica Nacional.

[109] Perkins, R. G., Kromkamp, J. C., Serôdio, J., Lavaud, J., Jesus, B. M., Mouget, J. L., Lefebvre, S., & m. Forster, R. (2010). The Application of Variable Cholorophyll Fluorescence to Microphytobenthic Biofilms. In D. Suggett (Ed.) *Chlorophyll a Fluorescence in Aquatic Sciences: Methods and Applications, Developments in Applied Phycology 4*, (pp. 237–275). Springer Science+Business Media B.V.

[110] Perkins, R. G., Lavaud, J., Serôdio, J., Mouget, J. L., Cartaxana, P., Rosa, P., Barille, L., Brotas, V., & Jesus, B. M. (2010). Vertical cell movement is a primary response of intertidal benthic biofilms to increase light dose. *Marine Ecology Progress Series*, *416*, 93–103.

[111] Pickup, J. C., Hussain, F., Evans, N. D., Rolinski, O. J., & Birch, D. J. S. (2005). Fluorescence-based glucose sensors. *Biosensors and Bioelectronics*, *20*, 2555–2565.

[112] Pinder, J. C., Fowler, R. E., Dluzewski, A. R., Bannister, L. H., Lavin, F. M., Mitchell, G. H., Wilson, R. J. M., & Gratzer, W. B. (1998). Actomyosin motor in the merozoite of the malaria parasite *Plasmodium falciparum*: implications for red cell invasion. *Journal of Cell Science*, *111*, 1831–1839.

[113] Potapova, M. (2010). *Platessa stewartii*. In Diatoms of the United States. http://westerndiatoms.colorado.edu/taxa/species/planothidium_stewartii [accessed 2013].

[114] Pouget, N., Dennis, C., Turlan, C., Grigoriev, M., Chandler, M., & Salomé, L. (2004). Single-particle tracking for DNA tether length monitoring. *Nucleic Acids Research*, *32*(9), e73.

[115] Poulsen, N. C., Spector, I., Spurck, T. P., Schultz, T. F., & Wetherbee, R. (1999). Diatom gliding is the result of an actin-myosin motility system. *Cell Motility and the Cytoskeleton*, *44*, 23–33.

[116] Poulsen, N. C., Sumper, M., & Kröger, N. (2003). Biosilica formation in diatoms: Characterization of native silaffin-2 and its role in silica morphogenesis. *Proceedings of the National Academy of Sciences*, *100*(21), 12075–12080.

[117] Qamar, A., McPherson, C., Babb, J., Bernstein, L., Werdmann, M., Yasick, D., & Zarich, S. (1999). The Goldman algorithm revisited. Prospective evaluation of a computer-derived algorithm versus unaided physician judgment in suspected acute myocardial infarction. *American Heart Journal*, *138*(4), 705–709.

[118] Quian, H. (2003). Fractional Brownian motion and fractional Gaussian noise. In G. Rangarajan, & M. Ding (Eds.) *Processes with Long-Range Correlations: Theory and Applications*. Germany: Springer-Verlag Berlin Heidelberg.

[119] Rief, M., Gautel, M., Oesterhelt, F., Fernandez, J. M., & Gaub, H. E. (1997). Reversible unfolding of individual titin immunoglobin domains by AFM. *Science*, *276*, 1109–1112.

[120] Rosu, H. C., Murguía, J. S., & Ludu, A. (2013). Scaling analyses based on wavelet transforms for the Talbot effect. *Physica A*, *392*, 3780–3788.

[121] Schafer, D. A., Gelles, J., Sheetz, M. P., & Landick, R. (1991). Transcription by single molecules of RNA polymerase observed by light microscopy. *Nature*, *352*, 444–448.

[122] Segall, D. E., Nelson, P. C., & Phillips, R. (2006). Volume-exclusion effects in tethered-particle experiments: Bead size matters. *Physical Review Letters*, *96*, 088306.

[123] Sifuzzaman, M., Islam, M. R., & Ali, M. Z. (2009). Application of wavelet transform and its advantages compared to Fourier transform. *Journal of Physical Sciences*, *13*, 121–134.

[124] Smayda, T. J., & Boleyn, B. J. (1965). Experimental observations on the flotation of matine diatoms. I. *Thalassiosira cf. nana*, *Thalassiosira rotula* and *Nitzschia seriata*. *Limnology and Oceanography*, *x*(4), 499–509.

[125] Stal, L. J., & Brouwer, J. F. C. (2003). Biofilm formation by benthic diatoms and their influence on the stabilization of intertidal mudflats. *Berichte – Forschungszentrum Terramare*, (12), 109–111.

[126] Strang, G. (1993). Wavelet transforms versus Fourier transforms. *Bulletin of the American Mathematical Society*, *28*(2), 288–305.

[127] Sutherland, I. W. (1999). Biofilm exopolysaccharides. In J. Wingender, T. R. Neu, & H. C. Flemming (Eds.) *Microbial extracellular polymeric substances. Characterization, structure and function*, (pp. 73–92). Springer, Berlin.

[128] Taylor, W. H., & Hagerman, P. H. (1990). Application of the method of phage T4 DNA ligase-catalyzed ring-closure to the study of DNA structure. *Journal of Molecular Biology*, *212*, 363–376.

[129] Umemura, K., Haneda, T., Tanabe, M., Suzuki, A., Kumashiro, Y., Itoga, K., Okano, T., & Mayama, S. (2013). Semi-circular microgrooves to observe active movements of individual *Navicula pavillardii* cells. *Journal of Microbiological Methods*, *92*, 349–354.

[130] Umemura, K., Yamada, T., Maeda, Y., Kobayashi, K., Kuroda, R., & Mayama, S. (2007). Regulated growth of diatom cells on self-assembled monolayers. *Journal of Nanobiotechnology*, *5*(2).

[131] Underwood, G. J. C., & Patterson, D. M. (2003). *The importance of extracellular carbohydrate production by marine epipelic diatoms*, vol. 40 of *Advances in Botanical Research*. Elsevier Academic Press.

[132] Ward, L., & Greenwood, P. (2007). *Scholarpedia*, *2*(12), 1537.

[133] Wetherbee, R., Lind, J. L., Burke, J., & Quantrano, R. S. (1998). The first kiss: establishment and control of initial adhesion by raphid diatoms. *Journal of Phycology*, *34*, 9–15.

[134] Wiggins, P. A., & Nelson, P. C. (2006). Generalized theory of semiflexible polymers. *Physical Review E, Statistical, Nonlinear, and Soft Matter Physics*, *73*, 031906.

[135] Wigglesworth-Cooksey, B., & Cooksey, K. E. (2005). Use of fluorophore-conjugated lectins to study cell-cell interactions in model marine biofilms. *Applied and Environmental Microbiology*, *71*(1), 428–435.

[136] Wigglesworth-Cooksey, B., van der Mei, H., Busscher, H. J., & Cooksey, K. E. (1999). The influence of surface chemistry on the control of cellular behavior: studies with a marine diatom and a wettability gradient. *Colloids and Surfaces B: Biointerfaces*, *15*, 71–79.

[137] Wong, W. P., & Halvorsen, K. (2006). The effect of integration time on fluctuation measurements: calibrating an optical trap in the presence of motion blur. *Optics Express*, *14*(25), 12517.

[138] Zurla, C., Franzini, A., Galli, G., Dunlap, D. D., Lewis, D., Adhya, S., & Finzi, L. (2006). Novel tethered particle motion analysis of CI protein-mediated DNA looping in the regulation of bacteriophage lambda. *Journal of Physics: Condensed Matter*, *18*(14), S225–S234.